Verena Amritzer, Graz University of Technology, BSc

Optical Properties of Phosphors for White Light Emitting Diodes prepared by the Solution Combustion Method

MASTER'S THESIS

to achieve the university degree of

Diplom-Ingenieurin

Master's degree programme: Technical Chemistry

submitted to

Graz University of Technology

Supervisor

Ao.Univ.-Prof. Dipl.-Ing. Dr.techn. Karl Gatterer

Institute of Physical and Theoretical Chemistry

Graz, January 2019

AFFIDAVIT

I declare that I have authored this thesis independently, that I have not used other than the declared sources/resources, and that I have explicitly indicated all material which has been quoted either literally or by content from the sources used. The text document uploaded to TUGRAZonline is identical to the present master‘s thesis.

Date

Signature

Danksagung

An dieser Stelle möchte ich mich recht herzlich bei meinem Betreuer Ao.Univ.-Prof. Dipl.-Ing. Dr.techn. Karl Gatterer für die Bereitstellung des Themas und die vielseitige und stets freundliche Unterstützung bei meiner praktischen Tätigkeit im Labor, sowie beim Verfassen meiner Arbeit während der gesamten Zeit bedanken.

Ebenso möchte ich meinen Dank an Ao.Univ.-Prof. Dipl.-Ing. Dr.techn. Franz-Andreas Mautner und Oberrätin Dipl.-Ing. Dr.techn. Brigitte Bitschnau richten, die mich mithilfe ihrer Durchführung der Röntgenbeugungsmessungen und bei der Auswertung der Spektren beim Vervollständigen dieser Abschlussarbeit unterstützt haben.

Weiters bedanke ich mich bei Hilde Freißmuth für die Chemikalienbereitstellung.

Ebenso gilt mein besonderer Dank an meinen Freund Manuel, der mich über die gesamte Studienzeit unterstützt hat und mir immer zur Seite stand.

Vielen lieben Dank auch meiner Freundin Katharina, die mich immer tatkräftig unterstützt hat.

Zu guter Letzt möchte ich meiner lieben Familie danken, die mir auch mit Rat und Tat beigestanden ist und mich während meines Studium durch Höhen und Tiefen begleitet hat.

Abstract

Rare earth doped inorganic materials are of high interest for the fabrication of white light emitting diodes. Therefore, in the frame of this master thesis three series of different phosphor materials, like Sm^{3+} doped $Ba_2YV_3O_{11}$, Dy^{3+} and Tm^{3+} co-doped $GdAl_3(BO_3)_4$ and Ce^{3+} doped $Y_3Al_5O_{12}$, were prepared by the solution combustion method. Each sample series consists of different concentrations of the rare earth metal ions to determine the optimal dopant concentration for the generation of white light with the highest possible efficiency. The solution combustion route is a fast process, which can produce phosphor materials with particle sizes in the nanoscale. For comparison purposes the Ce^{3+} doped $Y_3Al_5O_{12}$ was also prepared by the classic solid-state reaction procedure. The optical properties of the obtained products of each sample series and of both methods were characterized by reflectance and fluorescence spectroscopy. Then, the chromaticity values were calculated from the results of the fluorescence measurements and plotted in the 1931 CIE color chart. Additionally, the luminescence of the phosphor materials was investigated under the UV-lamp. Furthermore, XRD measurements of some chosen products of each sample series were carried out to examine the phase purity and determine the particle size.

Kurzfassung

Für die Herstellung von weißlicht-emittierenden Dioden sind Seltenerd-dotierte Materialien von großem Interesse. Deshalb wurden im Rahmen dieser Masterarbeit drei Serien von verschiedenen Leuchtstoffmaterialien, wie Sm^{3+} dotiertes $Ba_2YV_3O_{11}$, Dy^{3+} und Tm^{3+} co-dotiertes $GdAl_3(BO_3)_4$ und Ce^{3+} dotiertes $Y_3Al_5O_{12}$ mittels der Solution Combustion Methode hergestellt. Jede Probenreihe besteht aus verschiedenen Konzentrationen von Seltenerdmetall-Ionen, um die optimale Dotierungskonzentration für die Herstellung von weißem Licht mit der höchstmöglichen Effizienz zu bestimmen. Die Solution Combustion Methode ist ein schneller Prozess, durch welchen Phosphormaterialien mit Partikelgrößen im Nanobereich erzeugt werden können. Daher wurde eine Doppelbestimmung des Ce^{3+} dotierten $Y_3Al_5O_{12}$ für Vergleichszwecke mittels Festkörperreaktion hergestellt. Die optischen Eigenschaften der erhaltenen Produkte von jeder Probenreihe und von beiden Methoden wurden mittels Reflexions- und Fluoreszenzspektroskopie charakterisiert. Danach wurden die Chromatizitätswerte von den erhaltenen Werten der Fluoreszenzmessungen berechnet und im 1931 CIE Farbdiagramm eingezeichnet. Zusätzlich wurde die Lumineszenz der Leuchtstoffe mittels einer UV-Lampe untersucht. Weiters wurden XRD-Messungen an einigen ausgewählten Produkten jeder Probenreihe durchgeführt, um die Phasenreinheit zu untersuchen und die Partikelgröße zu bestimmen.

Table of content

1 Introduction

Today, in a world in which environmental aspects and power saving are priority matters, white light emitting diodes (WLEDs) become more and more attractive to replace conventional incandescent lamps. Due to their numerous further benefits such as a long life, high luminous efficiency, a broad spectral range and good safety properties, LEDs are considered as new generation of lighting sources. [1]

The improvement of the brightness and the energy efficiency of a LED was constantly in focus. Later, the color rendering index attracted high attention due to the necessity of white light in different applications. For example, the lighting in a museum is different compared to the lighting in a store, which also strongly depends on the color rendering index of the LED. Thus, WLEDs are manufactured with different optical features to cover a wide scope of applications. [2]

The crucial point for the development of WLEDs was in the 1990s due to the invention of a LED, that emits blue light. By the combination of the blue LED with a phosphor material, the production of white light was possible. This type of light emitting diodes are called phosphor converted light emitting diodes (pc-LEDs). In general, pc-LEDs are one of the two approaches to generate white light. A further possibility is the application of combined red, blue and green LEDs. However, this type of WLEDs is cost-intensive. Therefore pc-LEDs are favored, which consist either of a blue LED or of a near ultraviolet LED combined with an inorganic phosphor material. The phosphor, in turn, consists of a host matrix in which a small concentration of rare earth metal ions or transition metal ions are incorporated as activators. The incoming short-wavelength radiation from the blue or near ultraviolet LED is then converted by the phosphor to light with a longer wavelength in the visible spectrum. The incoming radiation and the produced emission generates then white light. [3]

There are several preparation methods for phosphor materials. The scope ranges from the solid-state reaction with included grinding steps, over the hydrothermal synthesis to the precipitation from a solution or a sol-gel. The solid-state reaction is the conventional method for the fabrication of phosphors. However, this approach is a time-consuming process and undesired contaminants can be introduced. The precipitation method requires a long preparation time too and the hydrothermal synthesis needs expensive equipment for the high temperature and pressure treatment. The solution combustion method is a very attractive preparation method, because it is very fast. Additionally, the solution combustion method is efficient in energy consumption and produces a uniform product. [4]

The Ce^{3+} doped $Y_3Al_5O_{12}$ (YAG) was the first phosphor material that was combined with a GaInN/GaN LED to generate white emission. The GaInN/GaN LED produces blue light and acts as an excitation source for the phosphor. The Ce^{3+} doped $Y_3Al_5O_{12}$ absorbs a portion of the blue light and converts it into yellow emission. Consequently, the blue and the yellow emission can be tuned to create white light emission with a high luminous efficiency and a good color rendering index. [5]

The advantage of the Ce^{3+} doped $Y_3Al_5O_{12}$ is, that this LED type is cheaper than the trichromatic combined LEDs. Furthermore, the luminous efficiency of the YAG pc-LED is also higher than the luminous efficiency of the green, red and blue LED device. [6]

However, the spectral range of the Ce^{3+} doped $Y_3Al_5O_{12}$ is not fully covered due to the missing emissions in the red part of the visible spectrum. The color rendering index could be improved by co-doping with other transition metal or rare earth metal ions. [7]

The generation of white light can be also achieved by the application of phosphors with a boro-aluminate group. One representative of this kind of phosphor hosts is the $GdAl_3(BO_3)_4$, which offers many important advantages, like the excellent nonlinear optical properties and luminescence efficiency. Additionally, the host is very chemical and temperature resistant. [8]

The $GdAl_3(BO_3)_4$ can be doped with a small amount of Dy^{3+} ions to result in a white emission. The Dy^{3+} ions show a significant yellow and blue emission band in the visible spectrum. Depending on the host material, the yellow emission can be more dominant due to its hypersensitivity. Therefore, the addition of Tm^{3+} ions can supply a portion of blue to shift the chromaticity values of the phosphor closer to the achromatic point. [9]

The $Ba_2YV_3O_{11}$ host material doped with Sm^{3+} ions is relatively innovative in the field of phosphor materials for WLEDs. The orange emission from the Sm^{3+} and the intrinsic emission from the $Ba_2YV_3O_{11}$ host can be adjusted to get directly white emission. The preparation of this phosphor by the solution combustion method leads to a product with particles in the nanoscale. This offers many advantages such as a high lumen output, a reduced internal scattering and the phosphor is very stable against high temperatures. [10]

The aim of this master thesis is the investigation of the optical properties of three different rare earth doped phosphor materials prepared by the unconventional solution combustion method. The luminescence and color coordinates of the inorganic phosphors are examined and how they differ from each other. Furthermore, the influence of the doping concentration of the rare earth metal ions in the host matrix is investigated to find the optimal activator concentration for the phosphors, with a high luminescence efficiency and color coordinates near to them of pure white light.

2 Theoretical Part

2.1 White Light Generation

Sunlight has always been an urgent necessity for human beings. Nowadays, there are also many artificial light sources, which bring brightness into our lives. Early on, in the first half of the seventeenth century a relation between light and color was noticed. It was discovered that light is not colorless and it is not only responsible for visual perception, which was the general belief until this time. The general thought of people was that the color of an object comes only from the object itself, but this assumption was changed shortly afterwards. The color of an object was explained by the fact, that the illuminating light experienced a transformation when it came in contact with the object and the modified light was then reflected back into the observer's eyes. The today's perspective of color is based on this consideration, which was made at that time. The definition of a color is not that simple because in addition to the physical part the observers own perception plays an important role. [11]

Humans can sense sunlight and all light which is related to it. Due to that fact, it is obvious that the interest is aimed at light sources, which produce light that imitates the spectrum of the sun. The spectral power distribution is an important factor for the perception of light. The blackbody radiation is a good example that shows similarities to the spectrum of sunlight. [12]

A blackbody is a lump of matter with thermal energy that emits light. It was known since the 19th century that intensity and spectral distribution of the emitted light depends on the temperature of the matter. [13]

The mathematical description is the famous Plank law. [14] Blackbody radiation emitted at 5777 K is compared with the emission of the sun in Figure 2.1.

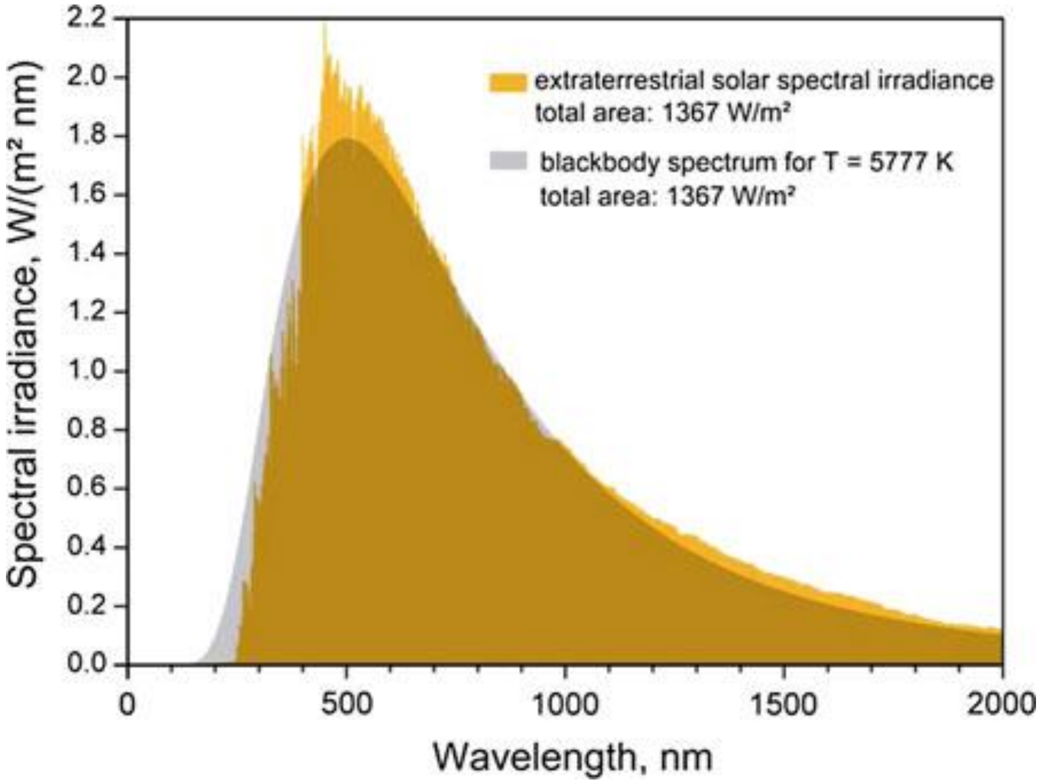

Figure 2.1: Spectrum of the sun compared to blackbody spectrum [15]

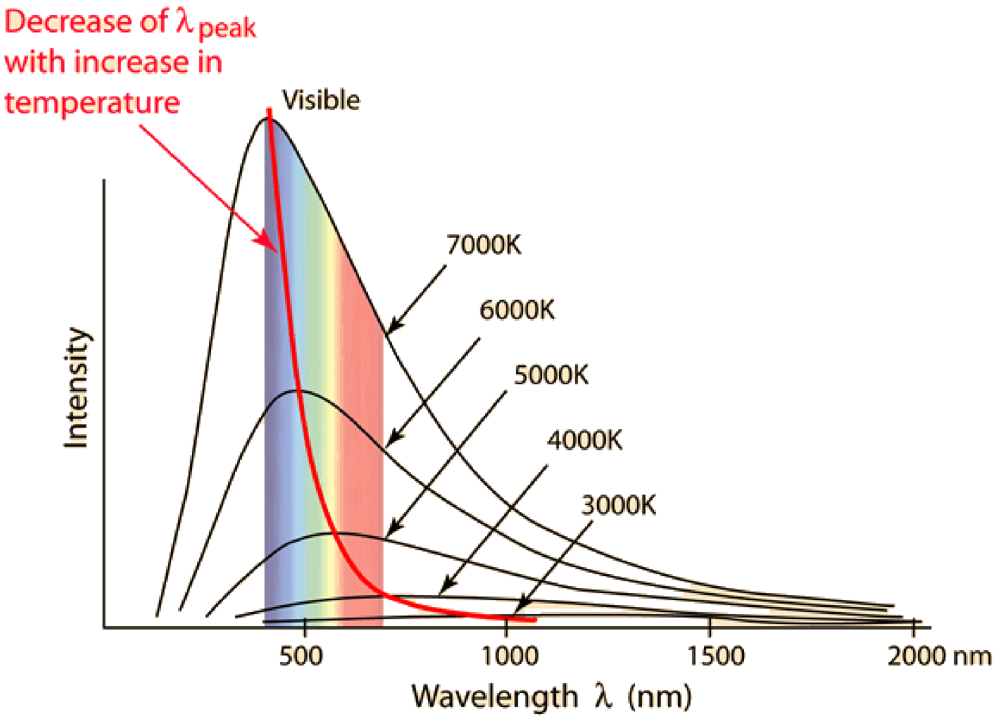

Figure 2.2: Blackbody spectrum at different temperatures, adapted from [16]

As can be seen in Figure 2.2, the spectral distribution strongly depends on the temperature of the blackbody. If the temperature is too low, the spectrum distinguishes significantly from the solar spectrum. The blackbody spectrum has the highest agreement with the spectrum of sunlight when the temperature is about 5800 K. This is also considered as the surface temperature (i.e., the temperature of the photosphere) of the sun. Carbon and tungsten are materials with high melting points and are hence utilized in incandescent light sources. Although, the melting point of carbon is higher, tungsten has a lower vapor pressure. This feature leads to a better stability of the light source. An additional property of tungsten is the increased emission of radiation in the visible range and a lower radiation in the infrared range. [12]

Figure 2.3 exhibits the spectrum of a tungsten halogen lamp compared to the spectrum of a blackbody and the spectrum of the sun.

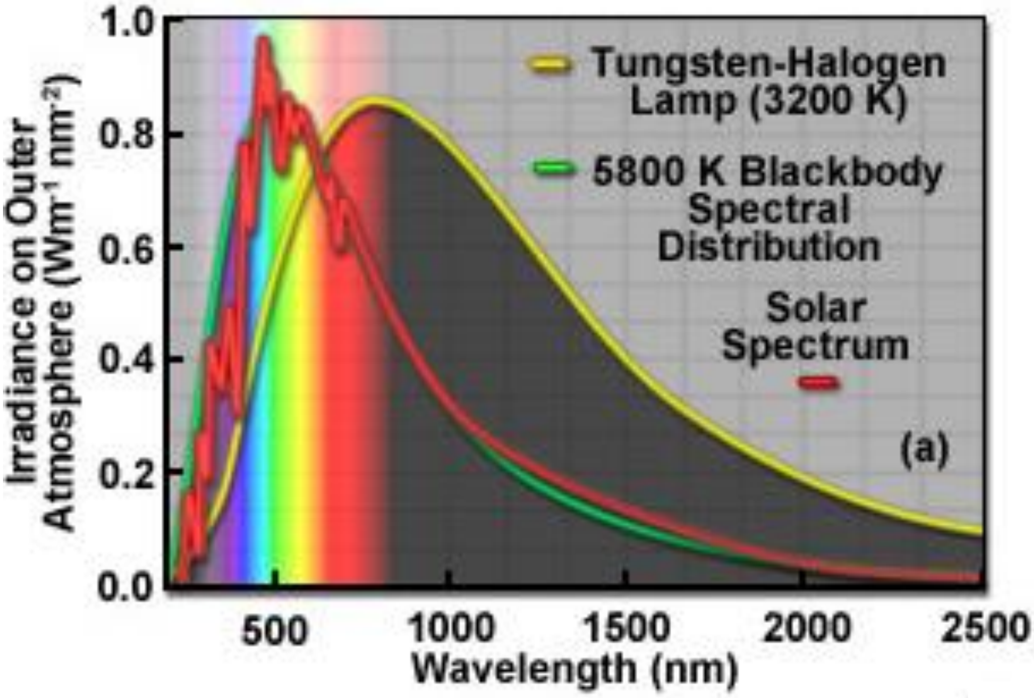

Figure 2.3: Spectrum of tungsten-halogen lamp compared to blackbody spectrum and spectrum of the sun [17]

A light source can be described by some important parameters. One of these is the luminous efficacy, which is the percentage of the visible radiation transformed from the power of the light source. Its unit is lumen per watt. Lumen is the unit of the luminous flux, which is defined as the quantity of light emitted per unit time. [18]

Another important parameter is the illuminance, which has the unit lux. It describes how bright an area is illuminated by a light source. It also considers the distance to the area. [19]

Light sources can be further characterized by the irradiance. It is defined as the radiant power hitting the surface of an object proportional to its area. Consequently, the unit is Watt per square meters. [20]

The quantum efficiency is another important term in the field of light generation. It is defined as the ratio of the photons absorbed by the material and the converted photons. It should converge to unity as far as possible. Furthermore, the color rendering index (CRI) is necessary to compare generated light from a light source with a reference light. In the test procedure, the reference source illuminates different test objects, which results in certain colors. The light source should be able to reproduce this color of the test object. [21]

2.1.1 Historical Developments

The request for everlasting brightness goes way back thousands of years in history since humans always had the desire to enlighten their places after the sunset or to shed light in dark spaces. The first mentioned lamp was a stone lamp invented approximately 40 000 years ago. It was made of a perforated limestone filled with pieces of animal fat in it. Due to a small flame, a very weak luminosity was created, but did not heat up the stone too much, which allowed people to carry the lamp in their hands without any additional grip. [22]

However, before this lamp was fabricated the only light sources were fire bowls or fire baskets with a rod or torch-like construction. They were often made of vegetables furnished with combustible materials. Later in the ancient Rome candles made of beeswax or animal fat were the first available candles and a common artificial light source. Subsequently, in the eighteenth century it was established that the combustion process took place due to the presence of oxygen. Based on this revolutionary scientific perception a specific oil lamp with a relatively high oxygen supply was developed. It provided an increased illuminance of the artificial light source. Almost at the same time, major advances in lighting generation occurred due to the invention of gas lighting which then became the commonly applied source of light for people. In the nineteenth century an apparatus made of calcium oxide (named limelight) was manufactured that imitated daylight due to the phenomena of candoluminescence. Nearly at the same time, the interest in electric lighting increased very fast. Experiments of discharge processes between two rods made of carbon and a copper-zinc battery used as a power source were a first impulse for electric lighting generation. Nevertheless, the breakthrough came with inventions like the continuous-current generator and the practical electric lighting device in the 1870s. Even though the practical electric lighting device showed only a short lifetime, it was applied as new street-lighting technique. With further improvements of lifetime and performance these devices were applicable for different purposes up to the beginning of the twentieth century. [23]

In 1878 Thomas Alva Edison had started his experiments for creating an efficient electric lighting source. His invention consisted of an electric candle or a burner. Due to experiments with a platinum incandescent element, he determined a dependence of the lifetime on the vacuum in the lamp. He found that the lifetime increases with a higher vacuum, which led him to the fabrication of a specific incandescent lamp. Edison had to deal with the high vacuum that had to be sustained during the use of the lamp. Furthermore, a suitable material for the incandescent element had to be found, because platinum melted at these conditions. Hence, he changed the platinum element against a carbon glow wire that resulted in much higher stability and lifetime. [24]

At the beginning of the 20th century the mercury vapor lamp was invented. The light emission of the lamp was in the blue-green range of the visible spectrum. Subsequently, sodium instead of mercury was used and thus the low-pressure sodium vapor lamp was developed. It was found, that a raise of the gas pressure leads to a broadening of the emission spectrum. Due to this insight the high-pressure sodium lamp was invented. [25]

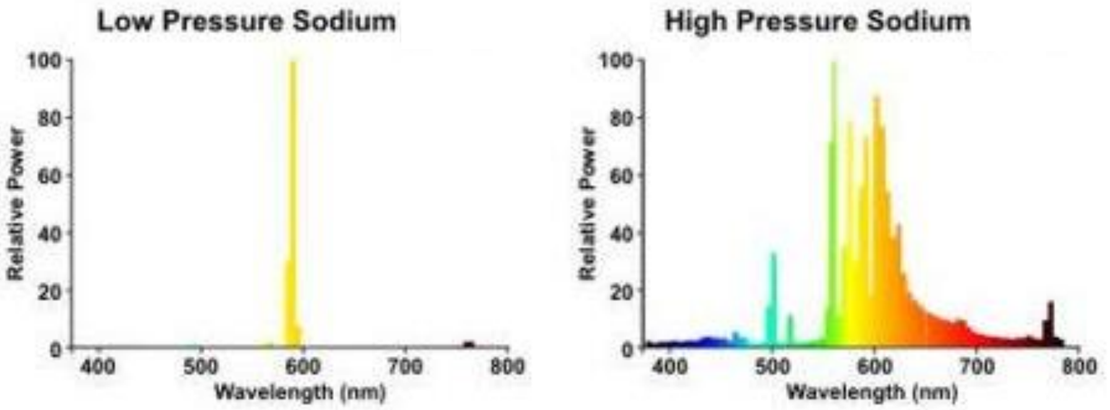

Figure 2.4: Visible spectra of low- and high-pressure sodium lamp, adapted from [26]

In 1938 a new type of light source, the fluorescent lamp was introduced, which became a big seller at that time. The lamp consisted of a small tube, in which a phosphor substance was deposited. Due to the illumination of the phosphor with ultraviolet light produced by a mercury discharge, white light was generated. Blue and green components coming from the mercury and the red component was from the phosphor. Shortly after the applications of the fluorescent lamps, the incandescent filament lamps and the sodium vapor lamps had become a solid part of human lives, light emitting diodes became very popular. The invention of the LED is based on a surprising discovery due to an electric experiment at the beginning of the 20th century. The flow of a current due to a potential difference of approximately 10 V through a SiC crystallite caused an emission of pale-yellow light. This voltage difference was sufficient for merely a few crystallites, but for the light emission of many crystallites it had to be increased to approximately 110 V. These studies laid the cornerstone for the LED technique.

However, the first applicable LED producing visible light was only fabricated in 1962. The LED was made of gallium arsenide phosphide and produced red light. Starting from this point, researchers focused on the development of further LEDs generating light of other colors from the visible spectrum. Hence, green and yellow LEDs were developed about 10 years later. Furthermore, the brightness of red LEDs was improved too. In the next decades, several different materials were found to be useable for light emitting diodes. In the 1990s the research on red and blue laser diodes was in major focus. Materials such as InGaP/GaAs and GaInAlN/GaN were applied for the construction of these lasers. The first one offered optical brightness properties in the yellow to red range of the visible spectrum. The other one produced red to amber light. However, there were a lot of problems to deal with in the following years, among other things the design of the LEDs. The general problem was, that the production of light took place inside the device, but it would be better if the light generation could be achieved on the surface. Thus, a technology was discovered were a transparent wafer made of GaP was used instead of the GaAs substrate. Due to this change, red LEDs delivered significantly higher efficiencies, which made them suitable for the usage as brake lights in cars or as red signals in traffic lights. Afterwards, AlInGaN had to stand the test if it was an appropriate material for light emitting diodes. In combination with a sapphire substrate it produces an energy-richer green, blue and ultraviolet radiation. The light generation with AlInGaN on a sapphire substrate, however, let several questions unanswered and a complete understanding of the process' background was not available. However, due to the high green sensitivity of the human's eye, green LEDs could be used in many applications. [25]

In the 1980s LEDs with monochromatic yellow, orange and red light with a good efficiency were invented. They were built with an AlGaInP chip. Later at the beginning of the 1990s GaInN chips were used to produce green, blue and violet LEDs, which supplied a high efficiency again. The invention of these monochromatic emitting light LEDs, which comprise the whole visible spectrum, lead to a breakthrough in the production of LEDs, that emit white light. [27]

Subsequently, research was directed towards the fabrication of white light emitting diodes (WLEDs). Consequently, the first LED that produces white light was invented in 1996. The white light emitting system consisted of a blue LED and a down-converting phosphor material. The phosphor material partly transformed the illuminating blue light into yellow radiation. The mixture of blue and yellow radiation resulted in white light emission. [25]

2.1.2 White Light Emitting Diodes

In the past only monochromatic emitting diodes that emit red, blue or green light were developed for different applications. However, the need for white light emitting diodes is increasing for their possible application as an alternative lighting source to conventional lamps. The many advantages of WLEDs such as their small-sized set-up, the long lifetime and the high flux efficiency make them very attractive for many different applications. Additionally, the environmental aspect and the energy-friendly operation are other reasons for further progress. In general, there are two main principal ways how white light can be produced in WLEDs. Either two wavelengths of complementary colors such as blue and yellow are mixed or, alternatively, a composition of red, blue and green light is created. Based on these two concepts many types of WLEDs were evolved until today. Consequently, methods were invented to generate white light by combining LEDs of different colors. (That was carried out in the same way as humans experienced white light by using red, blue and green LEDs together or by the combination of two LEDs with complementary colors.) [28]

The method of the combination of two or three monochromatic LEDs is very successful in its dynamic color control. The color can be changed by individually justifying the current at the single LEDs. A further benefit is the large quantum efficiency. After all, the expenses limit the usage of combined LEDs since there exist approaches which are much cheaper in their production and adaption. Another option for generating white light sources is the production of phosphor-converted LEDs (pc-LEDs) that also avoids the cost problem. The small assembly of these diodes is a significant advantage and the quantum efficiency is acceptable, even though it is less compared to the efficiency of the combined LEDs. Phosphor-converted LEDs consist of an excitation source either in the visible or in the ultraviolet range. The usage of both ranges is possible too. The phosphor acts as a modifier and changes the short-waved illumination from the excitation source into light with a longer wavelength. The incoming and the converted radiation together form observable white light. A very popular example for such a pc-LED is the combination of a cerium doped yttrium aluminum garnet (YAG) and a blue LED. [29]

The YAG phosphor in combination with the blue light source is one option of the two main sorts of phosphor converted LEDs that produces white light. It includes a yellow light emitting phosphor, that is deposited on a blue LED chip. However, instead of the yellow phosphor a combination of a red and green phosphor can be used too, because the emission spectra of both possibilities are quite related. The other opportunity is the application of a red-green-blue phosphor mixture combined with a LED chip, which delivers near ultraviolet radiation. [3]

The following figure demonstrates the different types for the generation of white emission.

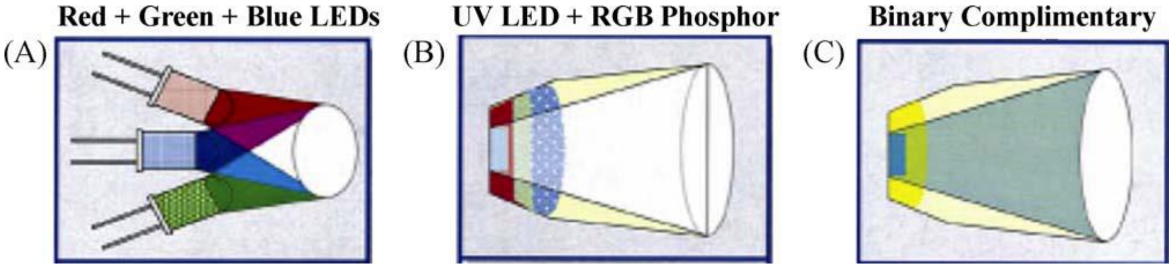

Figure 2.5: Different types of WLEDs, adapted from [30]

2.2 Samples and Preparation

2.2.1 Suitable Materials for White Light Emitting Diodes

In general, applicable materials for the generation of visible light must be able to emit light after the absorption of energy. Such materials are called phosphor materials and consist of a crystalline host material in which at least one kind of doping element is incorporated. Either the host lattice or one sort of doping atoms acts as a sensitizer and absorbs radiation, which is further transmitted to the activator. The activator or emitter is another kind of foreign atom in the host lattice, that produces a luminescence (sensitized luminescence) through this process. [31]

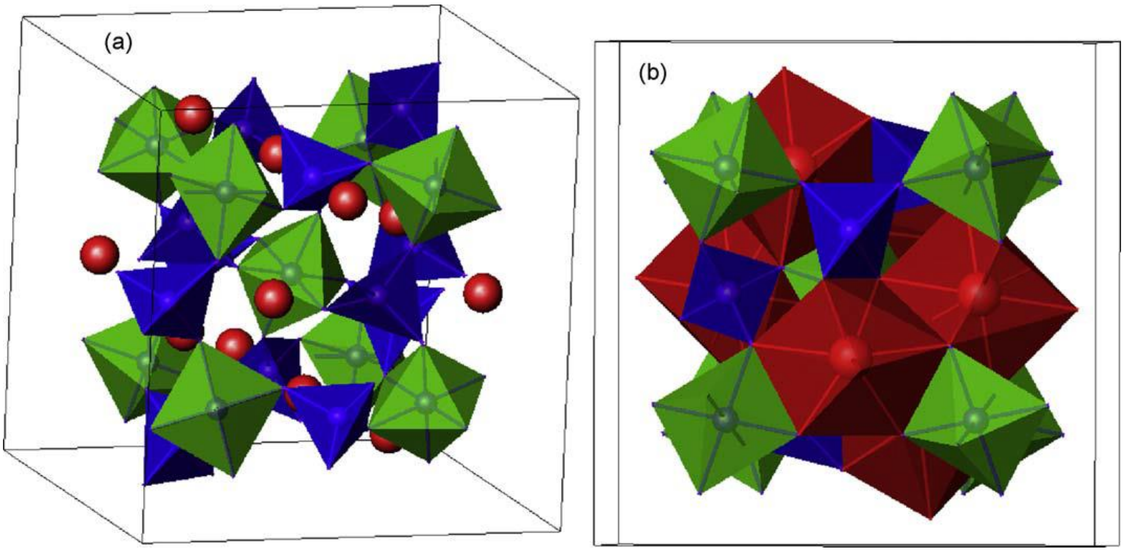

Figure 2.6: a) Crystal structure of $Y_3Al_5O_{12}$ consisting of AlO_6 octahedrons (green) and AlO_4 tetrahedrons (blue). Y^{3+} spheres (red) are in the spaces between the octahedrons and tetrahedrons. b) This picture of the $Y_3Al_5O_{12}$ structure illustrates the corner and the edge- sharing among the AlO_6 octahedrons (green), AlO_4 tetrahedrons (blue) and the YO_8 dodecahedrons (red). [32]

As mentioned in 2.1.2 phosphor materials generating yellow light are used for white light emitting diodes. The used host materials are often silicates, oxynitrides, aluminates and different garnets.

Garnets got a lot of attention for the application in LEDs and they are the most relevant category of these materials. One of the most readily used garnet is the yttrium aluminum garnet. Its structure is shown in Figure 2.6. [33]

The crystal lattice of the $Y_3Al_5O_{12}$ garnet has a cubic structure with a general formula of $(A)_3(B)_2(C)_3O_{12}$. The letters in the formula do not represent one element. They represent the Y^{3+} dodecahedral coordination to O^{2-}, and the Al^{3+} octahedral and tetrahedral coordination to O^{2-}, respectively. [32]

The doping with Ce^{3+} ions effects that the YAG emits yellow light after excitation. The cerium ions replace some yttrium ions in the crystal lattice and are the activators of the light emitting system. The incoming blue/green radiation is transformed into yellow radiation. This is caused by 5d-4f transitions due to very strong interactions of the Ce^{3+} ions and the host lattice. The 5d-state is displaced to lower levels of energy resulting in a yellow emission. The YAG has almost perfect optical properties to generate white light. [33]

The Ce^{3+} doped YAG offers an emission in a wide spectral range, that is beneficial for the emission of white light. Many further advantages like a more than acceptable quantum efficiency speak for its application. Additionally, the chemical stability plays an important role, which is also quite good for YAG. [34]

However, YAG as host material is not only of interest because of its application as phosphor material for LEDs. It is applied for many further purposes such as laser host material or as detector. Therefore, many other doping and co-doping elements can be added to vary its optical properties. They are mostly rare earth metal ions like Nd^{3+}, Eu^{3+}, Yb^{3+}, Dy^{3+} and the before mentioned Ce^{3+} and transition metal ions like Cr^{3+} are readily used too. [35]

Other interesting phosphor materials can be a combination of two phosphors, that offers new perspectives in the luminescence technique. A mix of a phosphor that contain borates and a phosphor that contains aluminates provides the positive features from both parts. Thus, the $GdAl_3(BO_3)_4$ (GAB), that belongs to this new type of phosphors, exhibits excellent optical and stability properties, when rare earth metals as activators are involved. The non-linear optical features and the chemical and thermal stability is caused by the rare earth ion doped borate host. [8]

Materials with non-linear optical features have the ability to change the frequency of a laser beam. The frequency of radiation that passes the material is doubled or even multiplied. Usually, this behavior occurs only at high light intensities. A famous example, is the Nd^{3+} doped YAG laser, which produces laser light at 1062 nm in the near infrared range. If this laser emission passes a suitable non-linear material, frequency doubling and tripling occurs, which transforms the laser emission into the visible range. [36]

Furthermore, $GdAl_3(BO_3)_4$ absorbs high quantities in the VUV/UV/NIR range. The aluminate-based part with rare earth metal activators is responsible for the excellent luminescence efficiency. It also delivers a good thermal stability. [8]

Additional, the $GdAl_3(BO_3)_4$ exhibits a sufficient degree of hardness and contains no moisture. Therefore, it is a very interesting material for the usage in lasers. [37]

The Gd^{3+} ions in the host matrix convey light in the ultraviolet range with a wavelength of approximately 200 nm to the activator. This feature is necessary for different purposes such as photolithography or the development of prototypes for lasers and many others. [38]

The GAB can be doped with many different rare earth ions as emitters. They displace some Gd^{3+} ions from their position in the host crystal and occupy them. For example, appropriate rare earth metal ions like Ce^{3+}, Dy^{3+}, Tb^{3+}, Tm^{3+} and Eu^{3+} are often used for light generation. Furthermore, co-doped GAB phosphors, that consist of a combination of two or more lanthanides, offer promising opportunities. For instance, the co-doping with Ce^{3+} and Dy^{3+} ions leads to a radiation of white light after excitation with UV-light. [39]

Another relatively innovative host material for phosphors is $Ba_2YV_3O_{11}$. In the past, the application of this material was not common and therefore experiments with only a few types of rare earth metals were known. Due to the doping of $Ba_2YV_3O_{11}$ with Sm^{3+} ions, a white luminescence after illumination is produced. Therefore, the material can be deployed in phosphor converted white LEDs. It shows excellent optical features and it is extreme resistant against heat. The $V_3O_{11}^{7-}$ group represents an orthovanadate and a pyrovanadate anion. The orthovanadate of the host matrix absorbs energy from the incident radiation and carries it to the activator ions. [10]

In materials with a YVO_4 part and with rare earth ions as dopant, the excitation energy is absorbed by the vanadate group. The energy is not directly transmitted to the activator ions. Instead, it passes through many other vanadate groups until finally a transfer to the rare earth ions takes place. However, the vanadate group offers an emission in the visible range, too. Consequently, the emission of the vanadate and the emission of the rare earth ions compete with each other. Lower temperatures decrease the luminescence of the rare earth metals and increase the intensity of the released vanadate radiation. The reason for this is, that the transfer between the vanadate groups is strongly influenced by the temperature. The energy transfer from the vanadate to the activator is only hardly affected by the temperature. [40]

As previously stated, the application of Sm^{3+} as activator is possible, which is a very important rare earth metal dopant used in various inorganic materials. It exhibits four transitions from the excited state of $^4G_{5/2}$ to four different lower energy levels $^6H_{5/2}$, $^6H_{7/2}$, $^6H_{9/2}$ and $^6H_{11/2}$ resulting in an orange-reddish luminescence. [41]

Further opportunities for applicable lanthanides in $Ba_2YV_3O_{11}$ for light production are for instance Eu and Dy. [42]

2.2.2 Conventional Oxide Method

The solid-state reaction method is the traditional way to synthesize phosphor materials. The reaction is performed in the solid-state and takes place between powdered reactants. The obtained products are mainly inorganic materials, which are used among other things as phosphor materials. The solid-state reaction method is very simple and an appropriate way to synthesize materials in a large scale. However, the sintering process needs very high temperatures because of the large grain size of the particles. To decrease the temperature, the grain sizes must be kept small. The driving force for the reaction is the migration of atoms between the reactants. Therefore, several grinding and heating steps are necessary. [43]

The high-temperature treatment of the material for a certain time leads to higher crystallinity of the product. However, the structural and morphological features decrease due to the high temperature. For a better diffusion behavior during the reaction a molten salt or a flux can be added. Consequently, the method is called then molten salt method. It delivers improved phosphor features such as a better growth of the particles and better emission properties. [44]

The solid-state reaction route has also some drawbacks like an undesired agglomeration or the insertion of contaminants because of the flux. The required high temperature is a challenge too. The treatment of the samples with a mill is necessary to receive fine particles leading to a new method, which includes the usage of high-energy ball mills. [45]

2.2.3 Solution Combustion Method

The solution combustion method that is also called solution combustion synthesis (SCS) is a relatively novel way to synthesize nanomaterials. Therefore, it can be another option for the fabrication of light emitting materials compared to the conventional oxide route. The materials show better properties due to the smaller particle size. The point of origin of the solution combustion method goes back to the 1980s with the discovery of the thermal degradation of metal hydrazinecarboxylate hydrates. The compound dissociates at low temperatures and results in a fine-grained metal oxide and releasing gases. The metal hydrazinecarboxylate hydrate itself acts as a fuel and as an oxidizer. It includes hydrogen and carbon atoms operating as fuel, while the oxygen atoms act as oxidizer. Characteristic for such type of reaction is that gases are released in large quantities. Experiments with aluminum nitrate hydrate (oxidizer) and urea (fuel) play an important role for further developments of this synthesis method. Both compounds were mixed and dissolved in distilled water. Then the reaction mixture was put into an oven where the reaction took place at 500°C. After only a few minutes the process was finished. Due to observations during the reaction it was figured out that the water began to boil and astonishingly the mixture started to burn with a bright flame. The result of the combustion was a very voluminous α-aluminum oxide with flaked shape. Additionally, large quantities of gases were produced. [46]

In principal, Solution Combustion Synthesis are self-sustained processes. A solution consisting of a metal, an oxidizer and a fuel are heated up and a combustion process takes place. The oxidizer is often a metal nitrite and the fuel can be categorized generally according to its chemical composition. Fuels are typical organic substances with a reactive part, for example an amino-, carboxyl- or hydroxyl-group. This type of synthesis is a fast high-temperature process because of the degradation of the oxidizer during the reaction. The SCS has many advantages which are reflected in the properties of the obtained powder. Since the starting materials are dissolved in distilled water under continuous stirring, a homogenous solution is generated. This step provides the intended composition of the product. Another great benefit is the increased crystallinity and the high purity of the synthesized powder due to the high temperature conditions of the combustion process. Additionally, the calcination step which is necessary in the conventional sol-gel method to reach the desired composition, is not required anymore. Furthermore, the reaction takes only a short time and yields a product with a particle size at the nanoscale. The reason for this is that the particles have not enough time to grow. In addition, the resulting gases prevent the increase of the particle size too. The solution combustion synthesis can be operated in two different approaches. The volume combustion synthesis was the first invented method which requires an external heating unit that can be an oven for example. It is performed in a homogenous solution containing a fuel and an oxidizer again. Due to the applied heat the reaction occurs with a thermal energy release. Hence, the regulation of the reaction is a major challenge. The second approach is the high-temperature synthesis, where the reaction propagates on its own. This method does not need a constant heating oven because the reaction is started only by one inflammation step. The incineration goes forward on the specimen and shows a continued self-propagating behavior. The self-propagating high-temperature method is easier to control and that results in the usage for incineration studies of different solutions. Another advantage is the rapid cooling of the sample. This results in a powder with a smaller particle size and a larger specific surface area of preventing further sintering. [47]

2.3 Rare Earth dopants and their Spectroscopy

Ce^{3+} belongs to the category of 5d-4f transition activators. Their energy levels are greatly influenced by their immediate environment. Therefore, cerium ions which replace some ions in the crystal lattice of the host material, exhibit other emission features than free ions. The luminescence of the activator ions depends strongly on the type of host material and its specific features. The reason for the light emission in the visible range of the Ce^{3+} ions is the decrease of the d-energy levels, when the ions are included into the host matrix. Due to the smaller gap between the 5d- and 4f-states the emission energy corresponds with the energy of visible light. In case yttrium aluminium garnet is used as host material and the Ce^{3+} ions are the dopant, it correlates with yellow radiation. In general, a smaller gap causes a red-shift of the color spectrum. The decrease of energy of the d-orbitals is caused by two phenomena, which are demonstrated in Figure 2.7. [48]

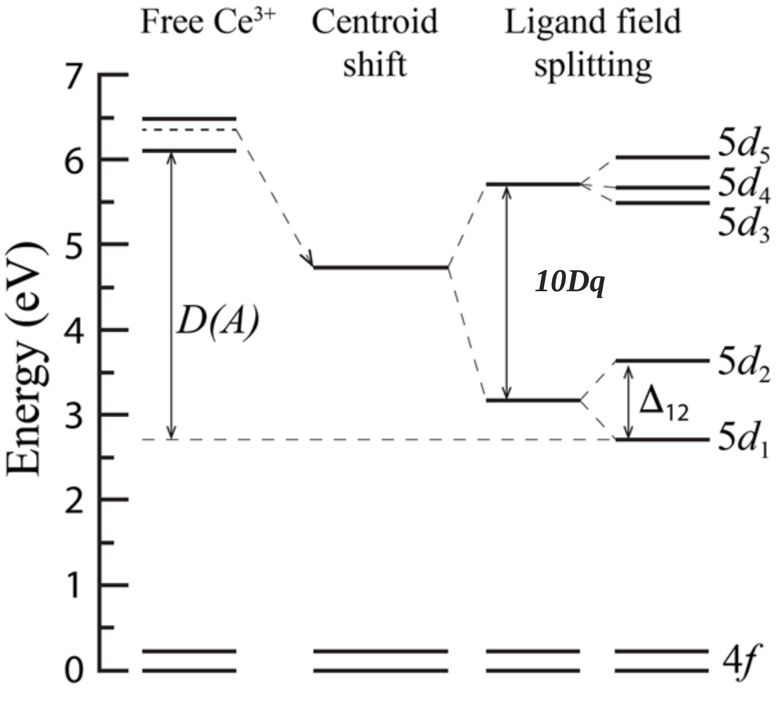

Figure 2.7: Energy levels of a free Ce^{3+} ion and how they are influenced due to the incorporation into a host matrix, adapted from [49]

One of them is the centroid shift, that effects a general lowering of the d-energy levels due to reduced repulsion of the electrons in the d-orbitals. The higher the polarizability of the anion ligand and the lower the electronegativity of the cations of the host material, the stronger the centroid shift. Due to a high covalence between the Ce^{3+} ions and the host anions, the electrons of the activator are partly displaced in the direction of the ligands. This reduces the repulsion of the electrons resulting in an energy level decrease, known also as the nephelauxetic effect. The second impact on the d-energy levels is the ligand field splitting. Due to the ligand field a separation of the 5d-levels into states with different energies occurs. The distance between the highest energy level and the lowest one is described by 10Dq (the crystal field strength). [48]

The 5d-orbitals of the Ce^{3+} ions in the YAG host experience a cubic crystal field splitting, which is indicated in Figure 2.7 by 10Dq. As can be seen, the d-orbitals are further separated due to a noncubic crystal field splitting. [32]

The crystal field splitting is influenced by many factors, especially by the interaction of emitter ions (activator) and ligand. The bond length and the covalency of the emitter ion with the host anion belong to these interactions. The emitter ion sites symmetry and the coordination number affect 10Dq as well. The ligand field splitting is different in various coordination polyhedra, for instance, an octahedral coordination has the largest value of Dq. In contrast to the d-orbitals, the f-orbitals are not situated in the outer electron shell. This leads to a high shielding from the external impacts. Hence, the f-levels experience the influence of the centroid shift and the ligand field splitting to a much lesser extent. [48]

A further applied rare earth metal as activator is Dy^{3+}. In general, the doping of a material with Dy^{3+} shows two significant emission bands in the yellow and the blue range of the visible spectrum. The peak at approximately 480 nm is due to the transition of $^4F_{9/2}$ to $^6H_{15/2}$ and results in an emission of blue light. The second significant peak occurs at approximately 575 nm because of the $^4F_{9/2}$ to $^6H_{13/2}$ transition. This relaxation generates an emission in the yellow range. In addition to the two significant peaks, a further very small peak at approximately 665 nm can be observed. This means, that the transition of $^4F_{9/2}$ to $^6H_{11/2}$ is noticed in the emission spectrum too. However, this transfer produces only a very weak red light. [50]

The energy levels of Dy^{3+} in a host matrix and the transitions from the excited state to the ground state and two further lower energy levels are illustrated in Figure 2.8.

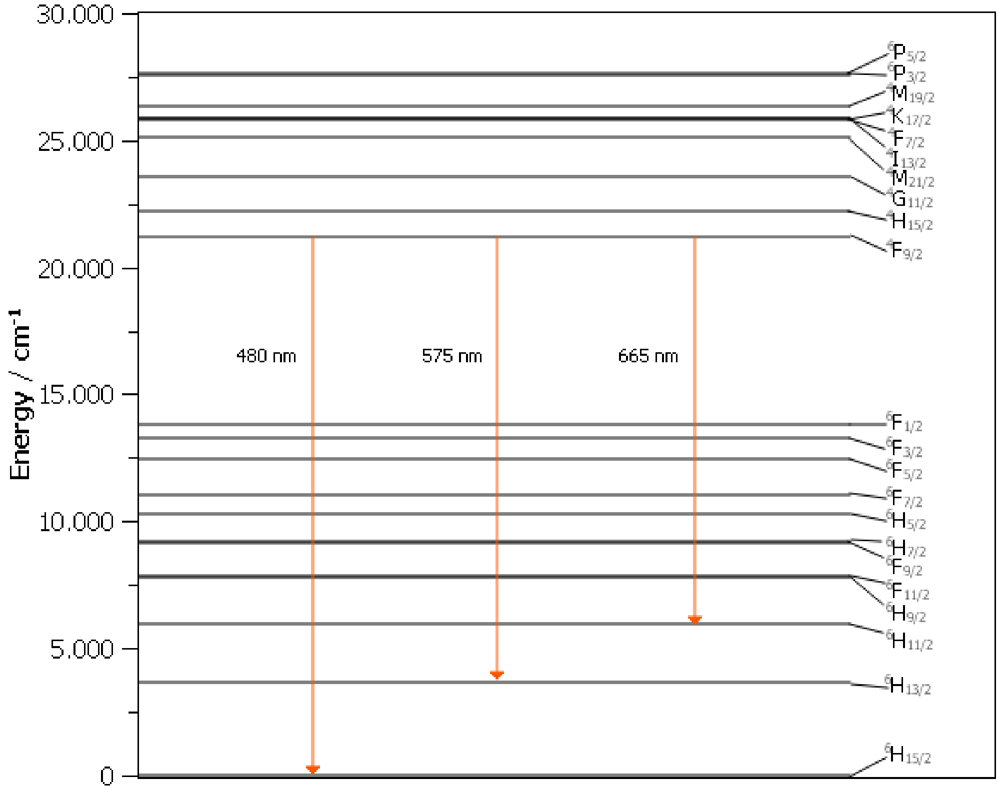

Figure 2.8: Energy levels of Dy^{3+} ion in a host and the transitions from the excited energy level to three different lower energy states

The ratio of the intensities of the blue and the yellow wavelengths play an important role. A certain ratio of the intensities of both colors can produce white light. Hence, Dy^{3+} is an appropriate dopant for hosts, which are used as phosphor materials for W-LEDs. The host surrounding has a heavy impact on the yellow emission due to the hypersensitivity of the $^4F_{9/2}$ to $^6H_{13/2}$ transition. In contrast, the transition of $^4F_{9/2}$ to $^6H_{15/2}$, corresponding to the blue emission is hardly affected by the surrounding. [51]

Therefore, the intensity of yellow radiation can be stronger than the intensity of blue radiation of Dy^{3+} in many hosts. Consequently, the emission of Dy^{3+} doped materials often results in a yellow light. [9]

The color of the emission can be partly influenced by the activator concentration or by the constituents of the crystal. However, there are sometimes circumstances in which the yellow part of the Dy^{3+} in a host is still more present because of the hypersensitivity. Then, another method is required to create white emission. Due to the increase of the blue part, the blue/yellow ratio can be varied and white light is generated. [52]

In many cases, the blue emission is increased by the introduction of Tm^{3+} due to $^1D_2$ to $^3F_4$ and $^1G_4$ to $^3H_6$ transitions. The transitions lead to emission bands in the blue range at wavelengths of approximately 450 nm and 470 nm. [53]

These transitions of Tm^{3+} after excitation can be seen in Figure 2.9, which also illustrates the energy levels of Tm^{3+} in a host material.

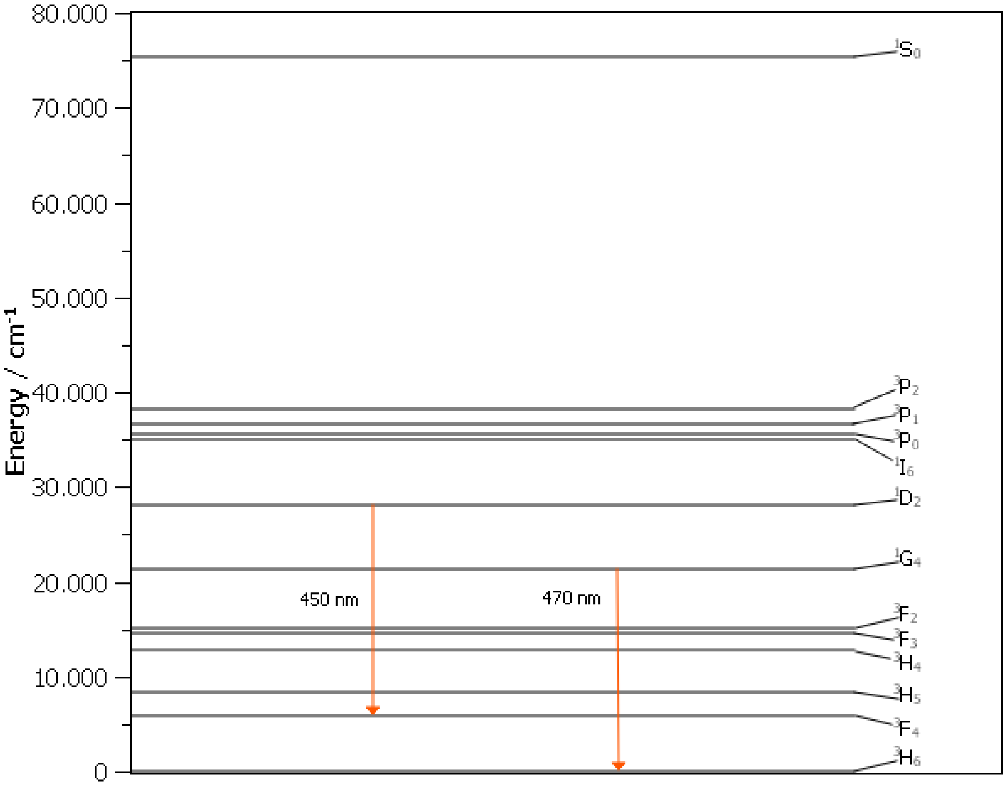

Figure 2.9: Energy levels of Tm^{3+} ion in a host and the transitions from two excited energy levels to two different lower energy states

Sm^{3+} ions are a common used dopant for phosphor materials too. The free Sm^{3+} ions produce a red emission after excitation. If the Sm^{3+} ions are incorporated into a crystal lattice of a host, they show an orange-red luminescence. This is traced back to intra f-f transitions in the 4f subshell due to charge transfer band between the lanthanide ions and the host ions. [54]

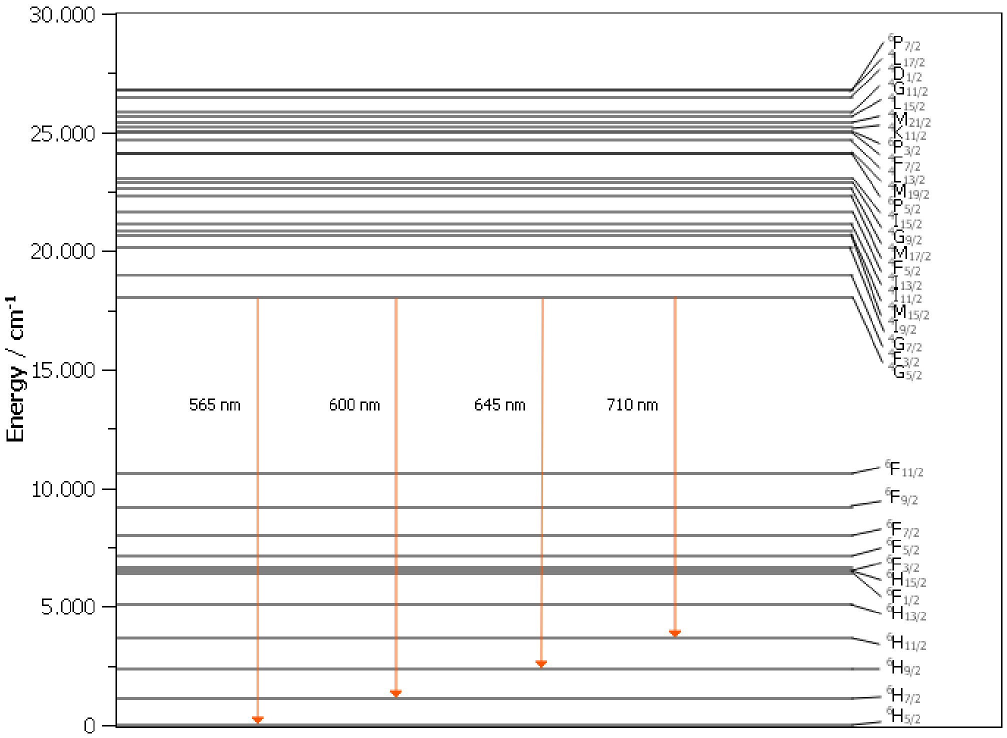

Figure 2.10: Energy levels of Sm^{3+} ion in a host and the transitions from the excited energy level to four different lower energy states

Figure 2.10 illustrates the relaxation of Sm^{3+} from the excited state to four lower energy levels, which produces the characteristic orange-reddish light in many host matters. The relaxation occurs from the excited $^4G_{5/2}$ level to the $^6H_{5/2}$, $^6H_{7/2}$, $^6H_{9/2}$ and $^6H_{11/2}$ energy levels. [55]

Each of these transitions results in an emission of light with a certain wavelength in the visible range. Therefore, the emission spectrum reveals four peaks with wavelengths of approximately 565, 600, 645 and 710 nm. In many cases, the two strongest emission bands are at 600 and 645 nm. The emission bands at 565 and 710 are often much weaker in their intensities. This intensity distribution leads to a generation of an overall orange emission. However, the distribution and hence the resulting color strongly depends on the host matrix. [56]

2.4 Measuring Color

2.4.1 The CIE systems and the Color Coordinates

There was a long road in the past since a standardized CIE (Commission internationale de l’éclairage) system was introduced. However, due to Wright´s and Guild´s efforts the CIE 1931 standard colorimetric observer could be established. Only a few participants carried out the tests for the two scientists. [57]

Their research was based on Maxwell´s earlier experiments. [58] The mixing of three specific monochromatic lights (stimuli) created an additive mixture of colors, which is experienced as one stimulus. For the sake of simplicity usually red, blue and green stimuli were applied. For the standardization specific parameters were defined leading to the progression of the CIE 1931 standard system. The selected terms for the performance were a dark environment and a 2° foveal range, which is located in the macula region of the retina (Maxwell´s spot), for watching the colors. A scheme of the experimental procedure is shown in Figure 2.11. [59]

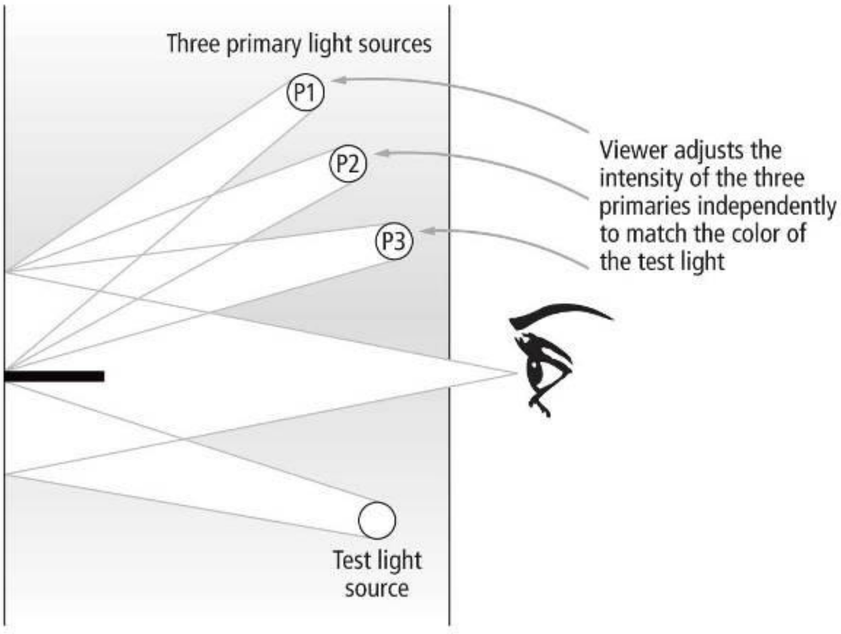

Figure 2.11: Color comparison experiment due to additive color mixing [60]

The participant observed a circular area, which was divided into two halves. In one half the reference color was presented. The participant had to match the reference color with the three monochromatic lights on the other half of the area. The light flow of the three stimuli with monochromatic wavelengths was set by regulators until a color agreement between both sides was obtained. Then the information for the light intensities of the combined stimuli was used to describe the reference color due to these R, G and B values (primaries). In Figure 2.12 the color matching functions of these values are illustrated.

As you can see, one of the curves has a negative part. In this case a color match can be only reached, when one of the monochromatic lights would be supplied on the side of the reference color. [59]

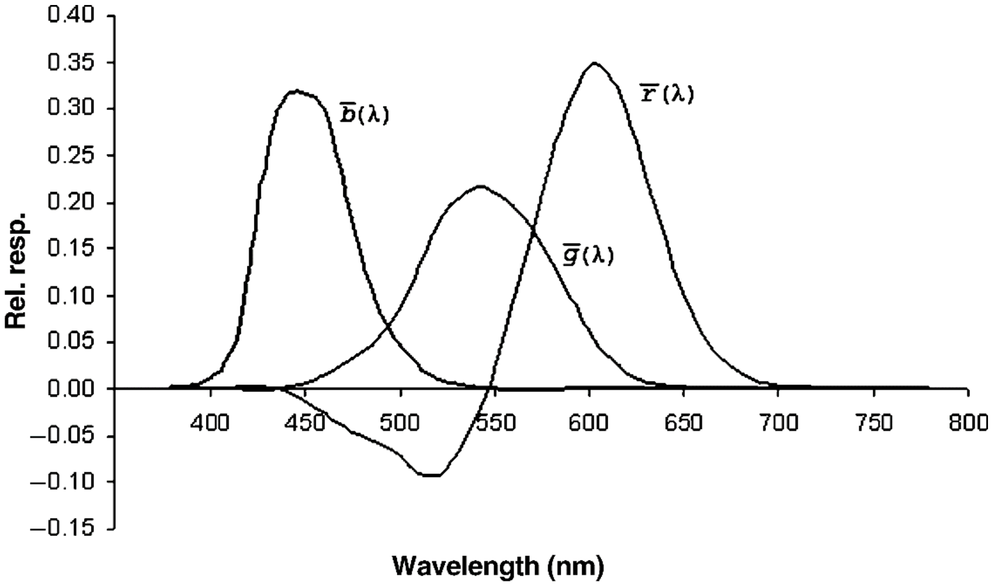

Figure 2.12: Color matching functions of the RGB trichromatic system [61]

In order to avoid negative values a coordinate transformation from the RGB into the virtual X,Y,Z space was made. These non-real but virtual primaries X, Y and Z and their color matching functions are shown in Figure 2.13. [61]

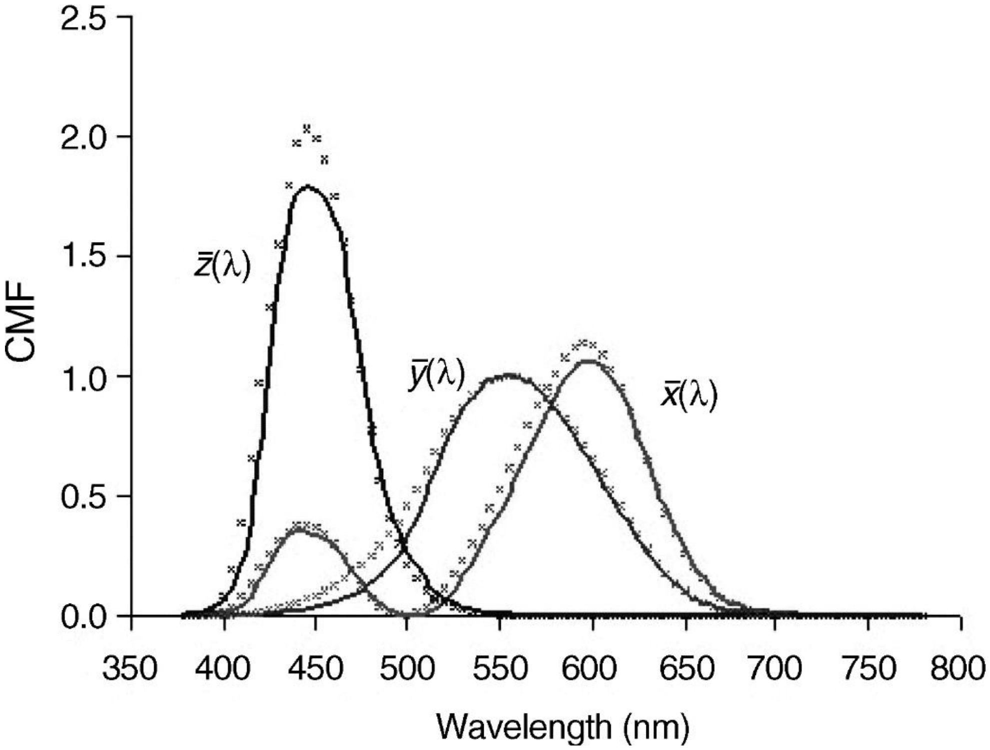

Figure 2.13: Color matching functions of the XYZ trichromatic system of the CIE 1931 color system shown as continuous lines. The crosses represent the color matching functions of the XYZ trichromatic system of the CIE 1964 color system. [62]

The X, Y and Z primaries are also called tristimulus values. Via the determination of the areas under the curves the tristimulus values can be calculated. This can be performed by an integration operation but for the sake of simplicity, multiplications at each wavelength serve also the purpose. Therefore, the spectral reflectance factor can be multiplied with the spectral power of the illumination lamp. The gained result is further multiplied with the three color-matching functions, which leads to three different values at each wavelength. Consequently, three rows with a lot of values are obtained. Afterwards, the values of each row are summed resulting in the X, Y and Z primaries. [63]

The characterization of an observed color is basically possible with the tristimulus values. However, the depiction with these values is slightly difficult because three-dimensional space would be needed. Therefore, the chromaticity values x, y and z were introduced. The x value is calculated by dividing the X primary through the sum of all three primaries. Accordingly, the y and z values are determined in the same way by dividing the Y or Z value through the sum of all primaries. The addition of the three chromaticity values amounts to 1. Hence, for the illustration of two of a colors properties, hue and chroma it would be sufficient to give the x and y values and the problem becomes two-dimensional. If, however, also the third property of a color, its brightness (or value) needs to be quantified Y must additionally be considered. [64]

Although the CIE 1931 standard colorimetric observer was a great system for characterizing colors, it worked only with a 2° foveal field. Therefore, research kept on running for a system in which a larger field of the retina could be stimulated. Finally, the CIE 1964 standard colorimetric observer was introduced due to the experiments of Stiles, Burch and Speranskaya. The main difference was the increased foveal range of 10°. Additionally, more participants were involved in the experiments, which makes the CIE 1964 color system more accurate than the CIE 1931 one. The measured data were converted again into the tristimulus values and consequently into the x_{10}, y_{10} and z_{10} chromaticity values similar to the CIE 1931 standard colorimetric observer. [65]

2.4.2 The CIE color chart

The chromaticity diagram of the CIE 1931 standard colorimetric observer is illustrated in Figure 2.14. Due to the information that the sum of all chromaticity values yielded 1, a two-dimensional diagram with coordinate axes of the x and y value can be created. It results in a horseshoe like shape of all perceptible visible colors. [66]

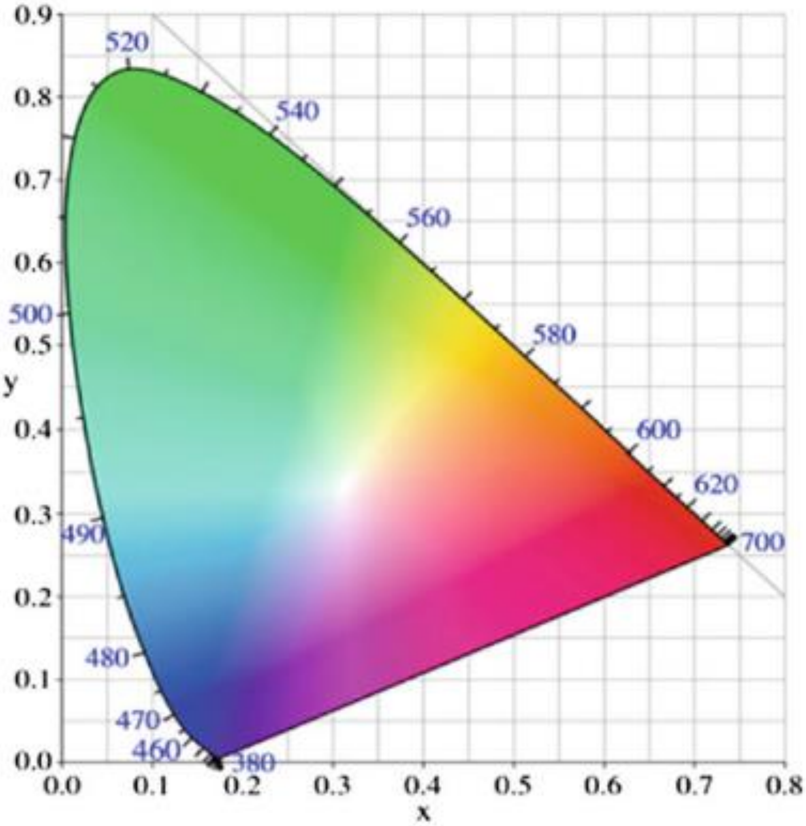

Figure 2.14: Color chart of the 1931 CIE standard colorimetric observer [67]

The 1931 CIE color chart consists of the x and y chromaticity values, which form a hoof-shaped area with different colors. Each point within this area represents a specific color with a fixed brightness. Only the points in the color triangle are visibly observable. If we look at one point in this diagram, it can be described by the x, y and z values. However, the determination of the tristimulus values X, Y and Z is not possible when merely the chromaticity values are given. A certain point with x, y and z description can stand for many various points with different X, Y and Z values, which differ in the brightness. Therefore, an additional information is required to identify a specific color. The Y value is gladly used for further specifications in combination with the y and z parameters. Hence, an entire description of a color point of the chart is feasible through x, y and Y and the X and Z tristimulus values can be calculated. All points on the boundary line are the x and y values of the monochromatic colors with different wavelengths from 380 to 780 nm. These spectral pure colors own the highest saturation level. Each color point within the color area can be determined as a mixture of three primary colors. In contrast, the boundary line between the blue and red region (purple line) consists of mixtures of deep red and blue. The Saturation level decreases from the outside to the inside of the diagram. In the center of the hoof-shaped area is the achromatic point with x=y= 0.33 and a saturation of zero. The pure white color and all grey colors with different shades are represented by the achromatic point. All possible mixed colors are located within hoof-shaped section and their belonging complementary colors are on a line, which goes through the achromatic point. [68]

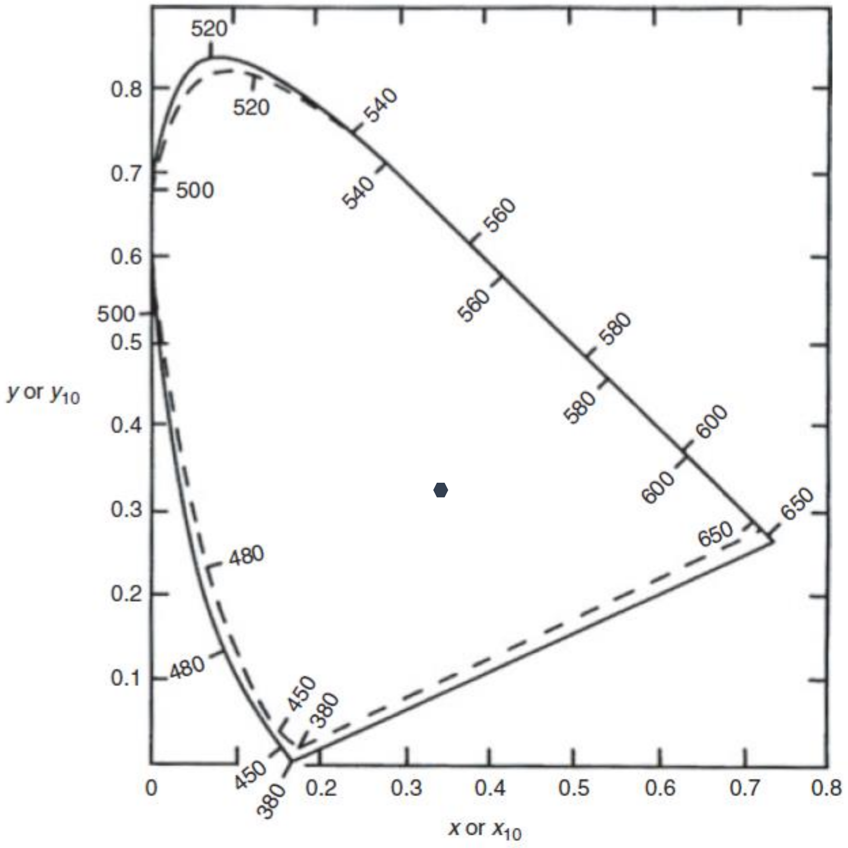

Figure 2.15: The difference of the color triangles of the 1964 CIE standard colorimetric observer (dashed line) and the 1931 CIE standard colorimetric observer (continuous line), adapted from [69]

Figure 2.15 illustrates the chromaticity diagram of the 1964 CIE color system (dashed lines). It is quite related to the 1931 CIE diagram (continuous line) as you can see in the figure above. Both have the typical hoof-shaped area of colors of the different wavelengths. Their areas in the plot have also nearly the same size. However, the difference between the two chromaticity diagrams is that the x and y values of some specific wavelengths of the 1964 CIE system are located further inside compared to the CIE 1931 diagram. The achromatic point, in turn, is in both chromaticity diagrams at the same position. [70]

3 Experimental Part

3.1 Chemicals and Equipment used

The chemicals used for the three experimental series of the solution combustion method and the experiments of the conventional oxide method can be seen in Table 3.1. To synthesize the Dy^{3+} and Tm^{3+} doped $GdAl_3(BO_3)_4$, Gadolinium nitrate was required which was produced from the available Gd_2O_3 and nitric acid. The obtained $Gd(NO_3)_3$ was assumed to contain six water molecules per formula unit.

The crystal water content for the used $Ce(NO_3)_3$ was not specified at the chemical container and thus also six water molecules per formula unit were assumed.

Table 3.1: Chemicals used

Substance	Manufacturer
$Ba(NO_3)_2$	Merck, 99%
NH_4VO_3	Sigma-Aldrich, 99.99%
$Y(NO_3)_3 \cdot 6H_2O$	Sigma-Aldrich, 99.9%
$Sm(NO_3)_3 \cdot 6H_2O$	Sigma-Aldrich, 99.9%
Gd_2O_3	Alfa, 99.99%
Gd_2O_3	RE Acton, 99.999%
$Dy(NO_3)_3 \cdot 5H_2O$	Sigma-Aldrich, 99.9%
$Tm(NO_3)_3 \cdot 6H_2O$	Sigma-Aldrich, 99.9%
$Ce(NO_3)_3 \cdot xH_2O$	ARGE Organische Synthese, ≥98.5%
$Al(NO_3)_3 \cdot 9H_2O$	Carl Roth, ≥98%
$Y_3Al_5O_{12}$	Alfa Aesar, 99.9% (REO)
H_3BO_4	Carl Roth, ≥99.8%
NH_2CONH_2	LOBA Chemie
HNO_3 65%	Fluka Chemie AG

The required instruments and the equipment used for all experiments are shown in Table 3.2.

Table 3.2: Equipment used

Equipment	Manufacturer
balance	Mettler BB240
Magnetic Stirrer	IKA ® RH basic 2
Muffle Furnace	Nabertherm ®, Program Controller S27
Hydraulic press	PerkinElmer
UV-lamp	Vilber Lourmat
Fluorescence Spectrometer	PerkinElmer LS 55
UV/VIS/NIR Spectrometer	Lambda 950
XRD	Bruker D8-Advance

3.2 Conventional Oxide Route

3.2.1 Preparation of Ce^{3+} doped $Y_3Al_5O_{12}$

The amounts of the starting materials were calculated such that 3 g of Ce^{3+} doped $Y_3Al_5O_{12}$ (YAG) resulted. Two samples were prepared with a Ce^{3+}-concentration of 0.7 wt% which corresponds to approximately 1 mol% Ce^{3+} ions. For the preparation $Y_3Al_5O_{12}$ and $Ce(NO_3)_3 \cdot 6H_2O$ were weighted in the appropriate quantities. The two reactants were mixed in a mortar and transferred into a platinum crucible. Then 3 mL Acetone were added, and the slurry was stirred for a short time with a spatula to ensure a homogenous mixture. Afterwards, the sample was covered with a platinum lid and placed in a preheated furnace. The sample was sintered at 1000°C for 6 hours. After cooling down the product was pulverized in a mortar again and further optical characterizations as well a XRD-measurement were carried out.

3.3 Solution Combustion Method

In general, the procedure for the three sample series were the same. The rare earth metal nitrates reacted with a fuel under an exothermic reaction to form the light emitting substance. They differed only in their combustion temperature and in their sintering temperature and time. Additionally, the dissolution or mixture procedure was slightly different.

3.3.1 Preparation of Sm^{3+} doped $Ba_2YV_3O_{11}$

For the fabrication of the Sm^{3+} doped $Ba_2YV_3O_{11}$ the masses of the starting materials were calculated to reach a product mass of 3 g or 1.5 g. The required amount of urea was determined by the oxidizing and reducing valencies of all oxidizers (nitrates) and the fuel (urea).

These valence values are based on the following assumptions. Metals, carbon, and hydrogen are taken as reducing elements with their corresponding valences metal (+n), carbon (+4), hydrogen (+1), respectively. Oxygen, as an oxidizer, has valence (−2), and nitrogen is assumed to have zero valence. So the reducing valence of urea as an example is calculated as: CH_4N_2O +6 (4+4x1+2x0-2 = +6)

An overview of the valencies of the different reactants are illustrated in Table 3.3. M is the general symbol for all possible metals.

Table 3.3: Valencies of oxidizers and fuel

Reactant	Valency
MNO_3	-5
$M(NO_3)_2$	-10
$M(NO_3)_3$	-15
Urea	+6

To produce 1 mol $Ba_2YV_3O_{11}$, 2 mol $Ba(NO_3)_2$ and 1 mol $Y(NO_3)_3{\cdot}6H_2O$ are necessary. Accordingly, the oxidizer/fuel equation was used for the calculation of the amount of moles of urea.

$$2 \cdot (-10) + 1 \cdot (-15) + x \cdot 6 = 0 \tag{1}$$

The x represents the required amount of urea for the solution combustion process and yields 5.83 mol. The quantity of urea remained the same for all samples in this experimental series. The additional $Sm(NO_3)_3{\cdot}6H_2O$ effects no change in the calculation, because the amount of $Y(NO_3)_3{\cdot}6H_2O$ was then reduced such that the sum of both compounds resulted in 1 mol.

The reactants were weighted in a 400 mL Duran beaker and approximately 20 mL distilled water were added. The beaker was covered with a cover glass. Then the mixture was stirred for 2-3 hours until a homogenous mixture remained. Afterwards, the beaker without the cover glass was placed into the preheated muffle furnace at 600°C for about 10 minutes where an exothermic reaction took place. After cooling down the product was pulverized in a mortar and then formed to a tablet with the help of a mechanical tablet press to get better sintering conditions. Subsequently, the pill was put into a platinum crucible and sintered in a muffle furnace at 900°C for 3 hours. During this time the Sm^{3+} ions were incorporated into the crystal lattice and the conversion to the Sm^{3+} doped $Ba_2YV_3O_{11}$ occurred.

Finally, the sintered beige-colored substance was pulverized again and used for further optical characterizations and XRD measurements.

A series of samples with various Sm^{3+}-concentrations was synthesized to investigate the optical features depending on the doping concentration.

Table 3.4: Concentrations of Sm^{3+} ions in each $Ba_2YV_3O_{11}$ sample of the experimental series

Experiments	$c_{Sm^{3+}}$ [mol%]
1	0
2	0.5
3	1.0
4	1.5
5	2.0
6	2.5
7	3.0

3.3.2 Preparation of Dy^{3+} and Tm^{3+} doped $GdAl_3(BO_3)_4$

The preparation of Dy^{3+} and Tm^{3+} doped $GdAl_3(BO_3)_4$ was similar to the fabrication of Sm^{3+} doped $Ba_2YV_3O_{11}$. However, the available gadolinium oxide had to be converted into gadolinium nitrate by evaporating the oxide with concentrated nitric acid and a small amount of water. This was carried out in a glass beaker under the hood by heating up until a white material was formed and no nitrous gases were generated anymore. It was assumed that the produced $Gd(NO_3)_3$ contained six crystal water molecules per formula unit. The necessary mass of urea was calculated by the oxidizer/fuel equation again. All nitrates and the fuel were considered for the determination and their valencies were used from Table 3.3.

The fabrication of 1 mol $GdAl_3(BO_3)_4$ required 1 mol $Gd(NO_3)_3 \cdot 6H_2O$, 3 mol $Al(NO_3)_3 \cdot 9H_2O$ and x mol urea.

$$1 \cdot (-15) + 3 \cdot (-15) + x \cdot 6 = 0 \qquad (2)$$

Equation 2 resulted 10 mol urea that were used for the preparation of all phosphors in this samples series. The doping elements (Dy^{3+} and Tm^{3+}) do not influence the required weight of the fuel again.

Then $Al(NO_3)_3 \cdot 9H_2O$, $Dy(NO_3)_3 \cdot 5H_2O$, $Tm(NO_3)_3 \cdot 6H_2O$, the self-produced $Gd(NO_3)_3 \cdot 6H_2O$, boric acid and urea were weighted in a 400 mL Duran beaker. Approximately 10 mL distilled water were added and the substances were dissolved rapidly under heating. Subsequently the solution was placed into the preheated muffle furnace at 500°C, where the combustion process took place within 15 minutes. Then, the cooled product was pulverized in the mortar and then sintered in a platinum crucible at 1100°C for 18 hours. For the sintering process the pulverized material could be sintered without any tablet pressing step due to the high sintering temperature and the long sintering time. After cooling down, the material was pulverized again. The obtained material had a white color and was characterized by the same methods as the Sm^{3+} doped $Ba_2YV_3O_{11}$.

A series of samples with different concentrations of the doping elements was prepared to compare the optical properties of each composition. Two experiments were carried out with only one of the two rare earth metals. For the residual series the concentration of Dy^{3+} ions remained the same and the Tm^{3+}-concentration was varied.

Table 3.5: Concentrations of Dy^{3+} ions and Tm^{3+} ions in each $GdAl_3(BO_5)_4$ sample of the experimental series

Experiments	$c_{Dy^{3+}}$ [mol%]	$c_{Tm^{3+}}$ [mol%]
1	3	0
2	0	3
3	3	1
4	3	2
5	3	3
6	3	4

3.3.3 Preparation of Ce^{3+} doped $Y_3Al_5O_{12}$

$Y(NO_3)_3 \cdot 6H_2O$, $Al(NO_3)_3 \cdot 9H_2O$, $Ce(NO_3)_3 \cdot 6H_2O$ and urea were weighted in a 400 mL Duran glass beaker. The required urea mass was determined by the oxidizing and reducing valencies equation again. As like the two sample series before, the valencies of the nitrates and the fuel were used from Table 3.3.

1 mol $Y_3Al_5O_{12}$ needed 3 mol $Y(NO_3)_3 \cdot 6H_2O$, 5 mol $Al(NO_3)_3 \cdot 9H_2O$ and x mol urea.

$$3 \cdot (-15) + 5 \cdot (-15) + x \cdot 6 = 0 \tag{3}$$

The preparation of the undoped and the Ce^{3+} doped YAG phosphors required 20 mol of urea. The amount of dopant did not matter in the determination of the fuel amount.

Then approximately 30 mL distilled water were added and the reactants were dissolved by stirring without any additional heat. The furnace was preheated to the reaction temperature of 500°C. The Duran beaker with the solution was placed into the furnace for 20 minutes until the reaction was finished. After cooling, the material was pulverized with a mortar and sintered in a platinum crucible at 900°C for 2 hours. The tablet pressing step for the sintering process was not required again. Then the cooled substrate was pulverized in the mortar and the yellow powder was characterized by different optical methods and XRD measurements.

To investigate the influence of the doping element amount on the optical features, an experimental series with different concentrations of Ce^{3+} ions were synthesized.

Table 3.6: Concentrations of Ce^{3+} ions in each $Y_3Al_5O_{12}$ sample of the experimental series

Experiments	$c_{Ce^{3+}}$ [mol%]
1	0
2	1
3	2
4	3
5	4
6	5

3.4 Reflectance Spectroscopy

The optical features were investigated with a *Lambda 950 UV/VIS/NIR Spectrometer*. The spectrometer used is a double-beam spectrometer. A tungsten halogen lamp for the visible and near-infrared range and a deuterium lamp for the ultraviolet range serve as light sources. The spectrometer uses a double-monochromator optical system and employs two different detectors, an InGaAs detector for the NIR range and a photomultiplier tube detector for the UV/VIS range. The spectrometer contains in addition an integrating sphere made of Spectralon® with a diameter of 150 mm for reflectance measurements. The related software is the *UV WinLab Software*.

The sample holder was filled with a small amount of the pulverized sample and then mounted at the spectrometer fixture. The Reflectivity of single wavelengths directed on the sample was determined and a reflectance spectrum was recorded in the range of 200 to 2500 nm with a data interval of 2 nm and a spectral slit width of 2 nm. Furthermore, an additional spectrum was recorded in the near-infrared radiation region (820-2500 nm) with a data interval of 1 nm and a slit width of 0.5 nm, because of a closer examination on all obtained peaks. These settings produced spectra in which the peaks were easier to identify and could be assigned to the different energy levels of the rare earth metals. The smaller values for the data interval and the slit width led to sharper peaks. Therefore, more peak maxima could be observed. However, it led to an increase of undesired underground noise too. Nevertheless, with the chosen parameter values, that were mentioned before, the peaks were sharp enough and the underground noise was kept relatively low.

3.5 Fluorescence Spectroscopy

Further optical characterizations were carried out with a *PerkinElmer LS 55 Luminescence Spectrometer*. The device is able to measure fluorescence, phosphorescence, chemiluminescence and bioluminescence. However, only the fluorescence mode was used for measurements of the phosphors. The light source is a xenon discharge lamp and the monochromator is a Monk-Gillieson type monochromator. The spectrometer consists of two sample detectors, a gated photomultiplier and a R928 photomultiplier, which cover a spectrum of 200 to 900 nm. Additional, a photodiode as reference detector is integrated. The related software is the *FL WinLab Software*.

For the fluorescence measurements the same filled sample holder (that was used before for the reflectance measurements) was prepared with an additional wire around the holder. This was necessary to keep a small distance between the holder and the fluorescence spectrometer fixture, where it was mounted – for some unexplained ereason this small distance provided much more fluorescence intensity. The measurements were performed in the excitation and the emission mode leading to the recording of an excitation and a fluorescence spectrum. At first, the suitable excitation wavelength was determined by an excitation spectrum by knowing the wavelength of one emission peak. Afterwards, the obtained excitation wavelength was used for recording the fluorescence spectrum. The adjusted parameters for the fluorescence measurements of the different experimental series of the solution combustion method and the conventional oxide method varied because of their different substance properties. Hence, the parameters for each experimental series after sintering process are listed in the following tables.

Table 3.7: Settings of emission mode of the fluorescence spectrometer for Sm^{3+} *doped* $Ba_2YV_3O_{11}$ *synthesized by solution combustion method*

Scan type	Emission
Start [nm]	300
End [nm]	900
Excitation wavelength [nm]	254
Excitation Slit [nm]	7
Speed [nm/min]	1200
Emission Slit [nm]	5
Gain	High
Auto Lamp	On

Table 3.8: Settings of emission mode of the fluorescence spectrometer for Dy^{3+} and Tm^{3+} doped $GdAl_3(BO_3)_4$ synthesized by solution combustion method

Scan type	Emission
Start [nm]	400
End [nm]	900
Excitation wavelength [nm]	358
Excitation Slit [nm]	15
Speed [nm/min]	1200
Emission Slit [nm]	3
Gain	High
Auto Lamp	On

Table 3.9: Settings of emission mode of the fluorescence spectrometer for Ce^{3+} doped $Y_3Al_5O_{12}$ synthesized by solution combustion method and conventional oxide route

Scan type	Emission
Start [nm]	400
End [nm]	900
Excitation wavelength [nm]	343
Excitation Slit [nm]	9
Speed [nm/min]	1200
Emission Slit [nm]	9
Gain	Low
Auto Lamp	On

3.6 XRD measurements and Rietveld Analysis

Crystallographic characterizations of some samples of each experimental series were carried out with a *Bruker D8-Advance Diffractometer* with a Lynxeye detector. The used data bases were the PDF4 + 2016 from ICDD (Powder Diffraction File, International Centre for Diffraction Data) and the structure data base ICSD (Inorganic Crystal Structure Data Base) of FIZ Karlsruhe. The Rietveld refinement was performed with *X'Pert Highscore Plus* from Panalytical.

The samples did not require any further treatment. The powder was deposited directly on the sample holder with a spatula and then smoothed with a glass plate. At first a rapid measurement with one of the samples was carried out to estimate the scattering power. After that, all selected samples from each experimental series were measured with the same adjusted parameters that can be found in Table 3.10.

Table 3.10: Settings of the diffractometer for the selected samples of the three experimental series synthesized by solution combustion method and the two Ce^{3+} doped $Y_3Al_5O_{12}$ substrates synthesized by conventional oxide method

Start [2θ]	10
End [2θ]	100
Step size [2θ]	0.02
Step time [s/step]	2
Cu-K_α radiation [Å]	1.5406
Voltage [V]	40 000
Current [mA]	40
Performance [W]	1600

4 Results and Discussion

4.1 Sm^{3+} doped $Ba_2YV_3O_{11}$ prepared with Solution Combustion Method

The different characterizations of the Sm^{3+} doped $BaYV_3O_{11}$ samples with various methods were carried out before and after the sintering process. This allowed to observe the incorporation of the doping element into the crystal structure.

4.1.1 Characterization with UV-lamp

The intermediate products (after combustion process and before sintering) were illuminated with UV-light of two different wavelengths. The illumination with a wavelength of 254 nm exhibited already an orange glow whereby the brightness varied with the Sm^{3+}-concentration. The highest lightning intensity was achieved by the sample containing 2 mol% Sm^{3+}. In both cases with increasing and decreasing doping concentration the intensity faded. The undoped sample showed a yellow glow. Further, the intermediate products were exposed to light with a wavelength of 365 nm. The whole concentration series offered no characteristic luminescence at this excitation wavelength.

After sintering the fluorescence behavior of the products was different compared to before the sintering, which can be seen in Figure 4.1.

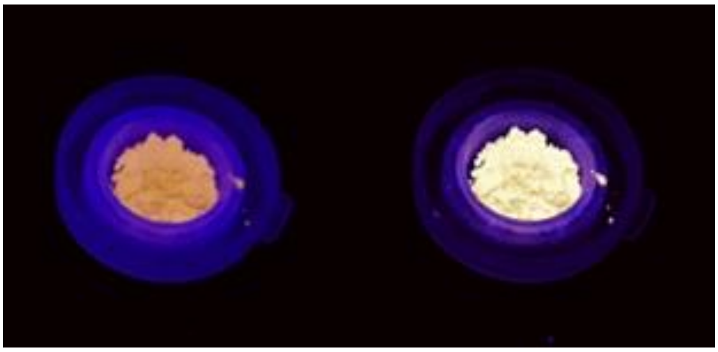

Figure 4.1: Luminosity of the sintered 2 mol% Sm^{3+} doped $Ba_2YV_3O_{11}$ sample. On the left side the phosphor was illuminated with a wavelength of 254 nm and on the right side it was illuminated with a wavelength of 365 nm.

Although the illumination with 254 nm exhibited an orange glow as with the intermediates before, the brightness of the sintered substrates was more intensive, and the orange color was even lighter. In general, the products after sintering showed a stronger luminosity but no apparent trend in the concentration series was visible for the naked eye.

Compared to the intermediate substrates the irradiation with 365 nm of the sintered samples produced a pale-yellow luminosity. The exception here was the 2 mol% doped Sm^{3+} sample, that did not glow at all this wavelength. No significant difference between the luminosity behavior of the different composition of the residual products can be observed with the human eye. The color and the brightness of the glow of the sintered Sm^{3+} doped $Ba_2YV_3O_{11}$ phosphor in Figure 4.1 is slightly altered by the camera used.

4.1.2 Characterization with Reflectance Spectroscopy

The reflectance spectra in the near-infrared range of the undoped and the 2 mol% Sm^{3+} doped $Ba_2YV_3O_{11}$ are illustrated in Figure 4.2. The reflectance spectra of both samples in the visible range were neglected, because no significant peak could be observed.

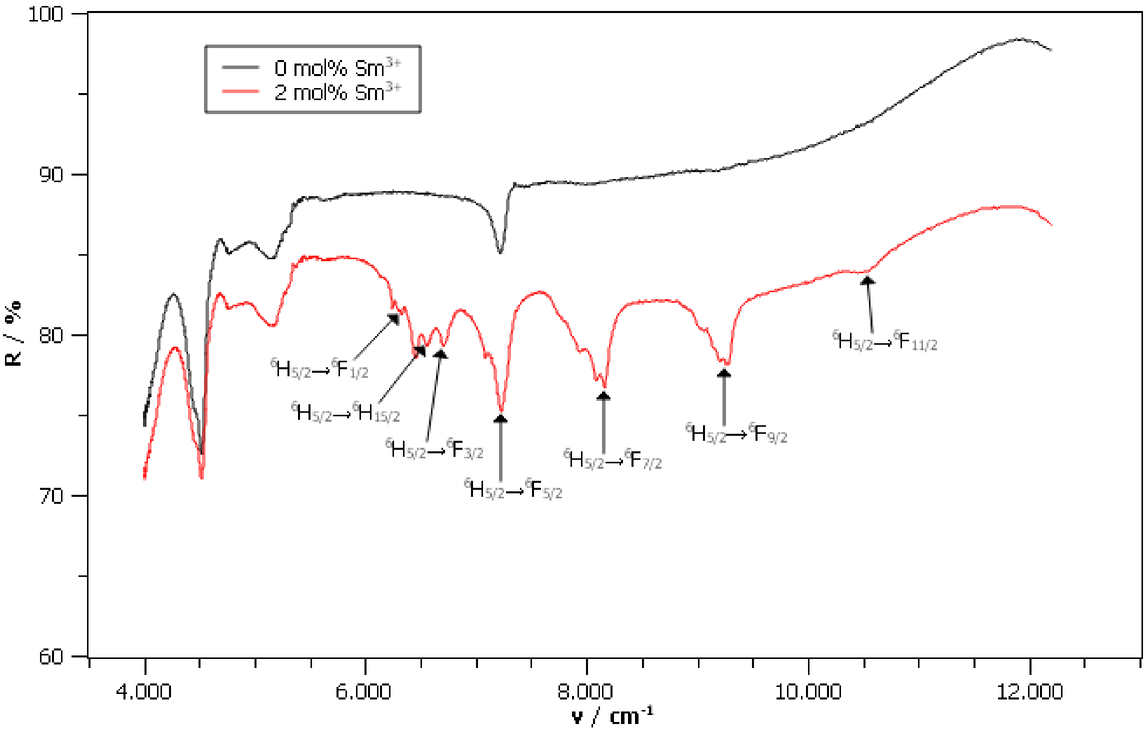

Figure 4.2: Reflectance spectra of undoped $Ba_2YV_3O_{11}$ and 2 mol% Sm^{3+} doped $Ba_2YV_3O_{11}$ powders in NIR range

The black curve in Figure 4.2 represents the undoped $Ba_2YV_3O_{11}$ after sintering, whereas the red curve demonstrates the 2 mol% Sm^{3+} doped $Ba_2YV_3O_{11}$ phosphor. From the comparison of the reflectance spectra of these two samples, the f-f transitions of Sm^{3+} can be identified. Transitions occur from approximately 11.000 to 6.000 cm^{-1} and correspond to transitions from the ground state ($^6H_{5/2}$) to the low-lying multiplets of Sm^{3+}.

There are also some unidentified peaks in the range of 6.000 to 4.000 cm^{-1}, which are present in the both samples. These partly broad peaks are not generated by transitions between the different energy levels of Sm^{3+}. Overtones and vibrational combinations of crystal lattice units can be responsible for the peaks.

4.1.3 Characterization with Fluorescence Spectroscopy

The emission spectra of the undoped $Ba_2YV_3O_{11}$ and the $Ba_2YV_3O_{11}$ samples with different Sm^{3+}-concentrations after the sintering process are shown in Figure 4.3.

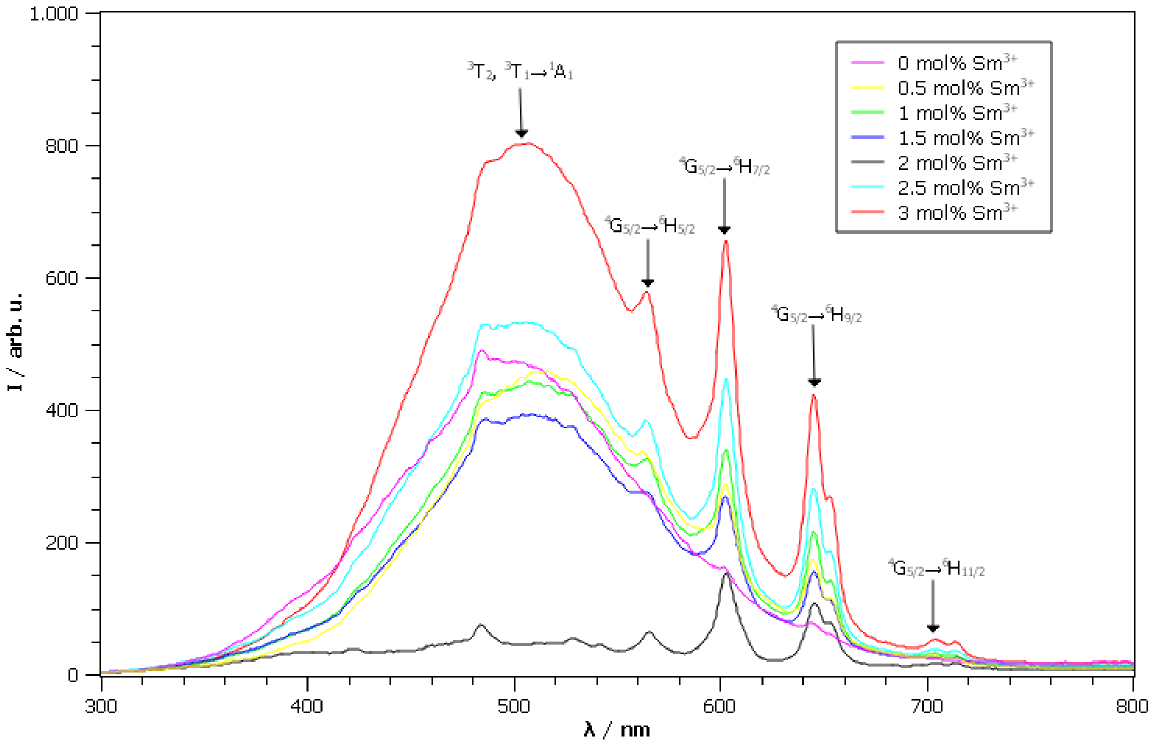

Figure 4.3: Emission spectra of sintered Sm^{3+} doped $Ba_2YV_3O_{11}$ powders with different Sm^{3+}-concentrations as activator ions

The purple curve in Figure 4.3 illustrates the emission spectrum of the undoped $Ba_2YV_3O_{11}$. It reveals only one broad peak ranging from approximately 380 to 680 nm. Due to the absence of Sm^{3+} ions, the peak belongs to the vanadate group.

The broad emission band is caused by spin-forbidden transitions, more precisely by $^3T_1$ to $^1A_1$ and $^3T_2$ to $^1A_1$ transitions. [71]

This emission band from the vanadate group occurs also in all emission spectra, belonging to the phosphors with different Sm^{3+}-concentrations. The samples with a Sm^{3+}-concentration from 0 to 2 mol% exhibit a decrease of the intensity of the vanadate peak. The 2 mol% Sm^{3+} doped $Ba_2YV_3O_{11}$ has a significant lower luminescence intensity of this peak compared to the others. However, a broad peak in the range of 380 to 680 nm is identifiable. The phosphors with a Sm^{3+}-concentrations of 2.5 and 3.0 mol% have, in turn, higher intensities of this emission band.

All other visible peaks in Figure 4.3 are due to the Sm^{3+} ions activator. It is well recognizable, that these peaks do not occur in the undoped sample. There are four transitions from the excited state $^4G_{5/2}$ to four different energy levels with lower energies. The peak of the relaxation from $^4G_{5/2}$ to $^6H_{5/2}$ is around 560 nm, which corresponds to green/yellow radiation. The transition from $^4G_{5/2}$ to $^6H_{7/2}$ occurring at approximately 605 nm produces a yellow light emission. A further significant peak appears at around 650 nm, which corresponds to the $^4G_{5/2}$ to $^6H_{9/2}$ transition. This relaxation generates emission in the orange range. Additionally, a very small peak is noticeable at 705 nm, which means that a transition from the excited state $^4G_{5/2}$ to $^6H_{11/2}$ also takes place. The energy release at this relaxation produces a red emission. However, the intensity of the peak is very weak, therefore the contribution to the overall emission intensity is very small.

As you can see, emission spectrum of Sm^{3+} doped $Ba_2YV_3O_{11}$ reveals an emission nearly over the entire visible range, which are good conditions to generate white light. However, the high intensities in the yellow range and the significant peaks in the orange and red region are responsible for the yellow and orange perception.

The emission spectra of the Sm^{3+} doped phosphors exhibit no particular trend of an increase or decrease of the intensities depending on the activator concentration. The $Ba_2YV_3O_{11}$ with 3 mol% Sm^{3+} ions shows the highest intensities of all peaks. Consequently, it has the general strongest luminosity of the sample series.

According to the literature, the sample series should show a decrease of the vanadate emission band with increasing the Sm^{3+}-concentration and the peaks caused by the transitions of the Sm^{3+} should first increase and then a concentrations quenching should occur at a doping concentration of 2.5 mol% Sm^{3+} ions. [10] This behavior, cannot be observed in this sample series, which can be seen in Figure 4.3. As already mentioned, the phosphor with the highest Sm^{3+} ions amount shows the strongest peaks over the visible range, but according to the literature it should not have these distinct emission band. But the phosphors with 1.5 or 2.0 mol% Sm^{3+} ions should show the strongest peaks due to the transitions of Sm^{3+}. Although no trend according to the activator concentration is obtained, all samples of the series exhibit the characteristic transitions of the vanadate and the samarium part resulting in a yellow/orange luminescence.

4.1.4 CIE Color Coordinates and Color Chart

The 1931 CIE color chart with received chromaticity values obtained for the sintered Sm^{3+} doped $Ba_2YV_3O_{11}$ samples serves as visual demonstration of the obtained colors. The chart is illustrated in the following figure.

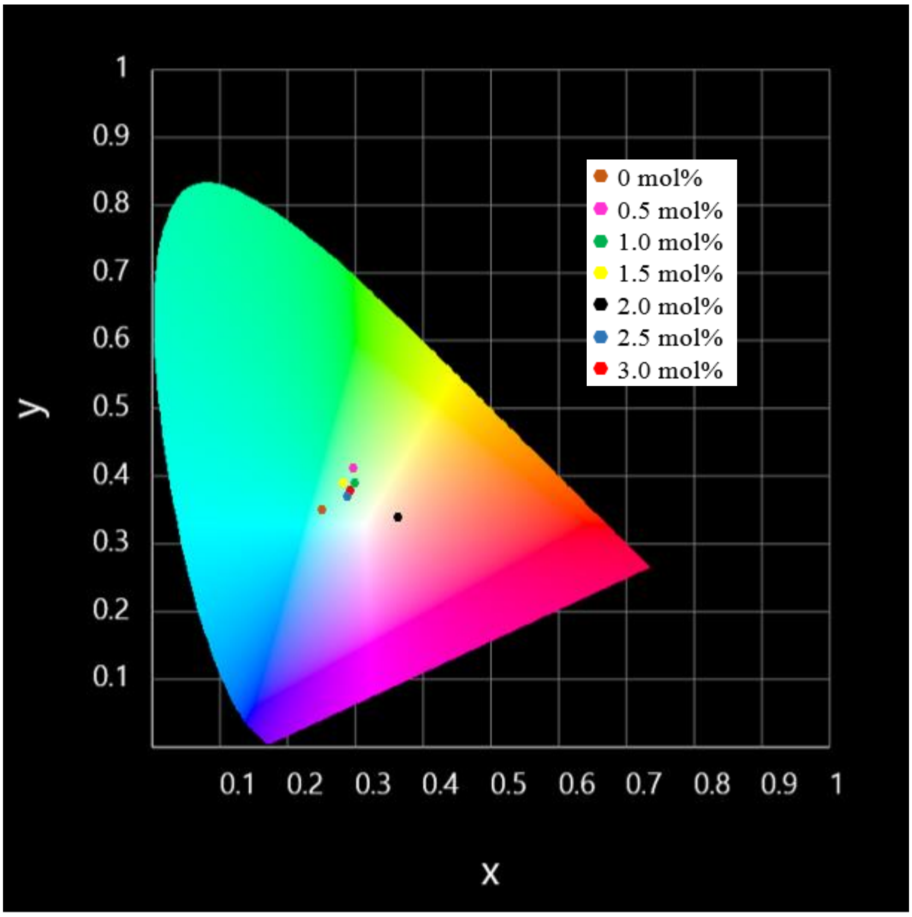

Figure 4.4: 1931 CIE color chart with marked chromaticity values of the sintered Sm^{3+} doped $Ba_2YV_3O_{12}$ phosphors

The colored points in Figure 4.4 represent the color coordinates of the Sm^{3+} doped $Ba_2YV_3O_{11}$ sample series. The sintered Sm^{3+} doped materials should have their chromaticity values around the achromatic point (with x = y = z = 0.33). As can be seen in the illustration most of the samples have lower x and higher y values than expected. However, they are very near to the achromatic point. The points are slightly shifted to the light green area. As was first mentioned in 4.1.1, the samples emit a light orange glow upon an excitation with 254 nm and a yellow emission with 364 nm excitation. The only exception was the 2 mol% Sm^{3+} doped sample, which shows only an orange glow under the UV lamp. This orange lightning of the 2 mol% doped material is confirmed with the color results from the fluorescence measurement and the calculations, which is marked with a black point in Figure 4.4. All other dots in the color chart are relative near to each other meaning that the Sm^{3+} doped $Ba_2YV_3O_{11}$ powders have similar chromaticity values. No trend because of the different concentrations of the doping element is recognizable. Due to that a concentration quenching cannot be observed as well.

4.1.5 Crystallographic Characterization

Four samples of the experimental series, prior to the sintering step, were characterized by XRD measurements. The following figure shows the spectrum of the Sm^{3+} doped $Ba_2YV_3O_{11}$ substrate with a Sm^{3+}-concentration of 1 mol%.

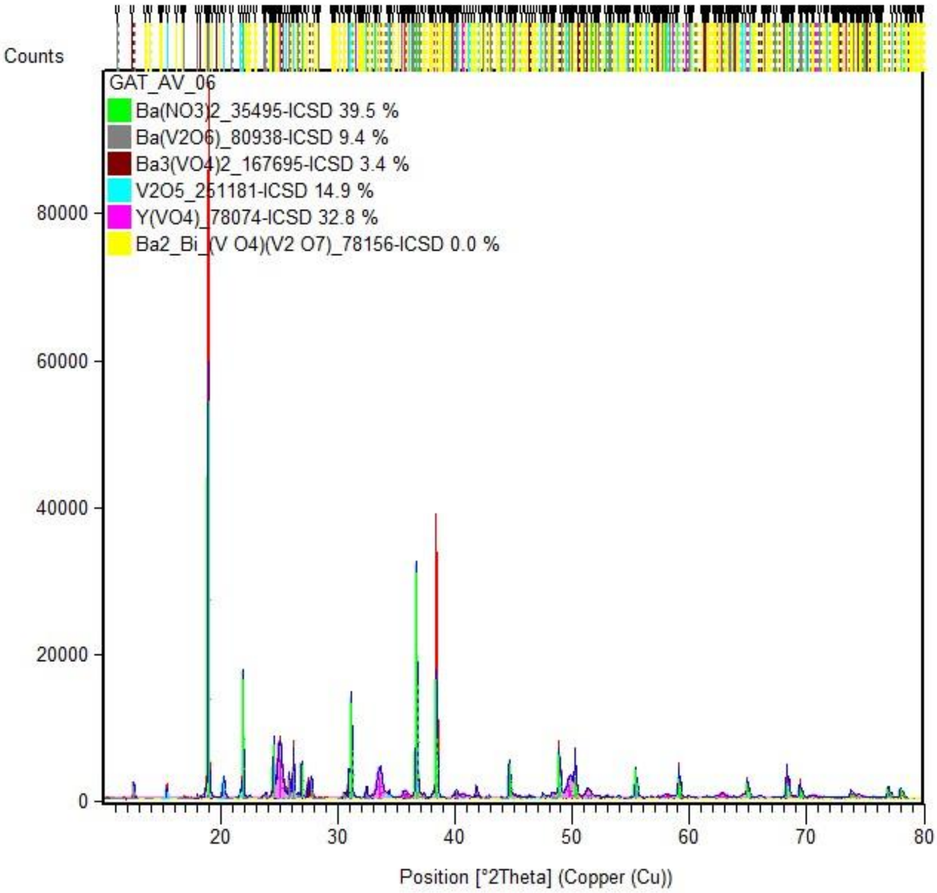

Figure 4.5: XRD spectrum with Rietveld refinement of $Ba_2YV_3O_{11}$ with 1 mol% Sm^{3+} ions before sintering

Figure 4.5 illustrates the composition of the sample after the combustion process. The $Ba_2Bi(VO_4)(V_2O_7)$ phase in the image corresponds to the $Ba_2Y(VO_4)(V_2O_7)$ phase, which means that the Rietveld refinement results in the same crystal structure for $Ba_2Y(VO_4)(V_2O_7)$ as for the bismuth compound. However, no bismuth is present in the product. It is also important to mention that the samarium is not considered for the crystal structure determination. As can be seen there is no desired $Ba_2YV_3O_{11}$ in the sample before the sintering was performed. A high percentage of the $Ba(NO_3)_2$ starting material still occurs after the combustion. Additionally, some vanadates of barium and yttrium are formed. The other un-sintered samples of this series show similar results and are not shown here.

The same four samples were also characterized by XRD measurements after the sintering process. The results are shown in the following figures.

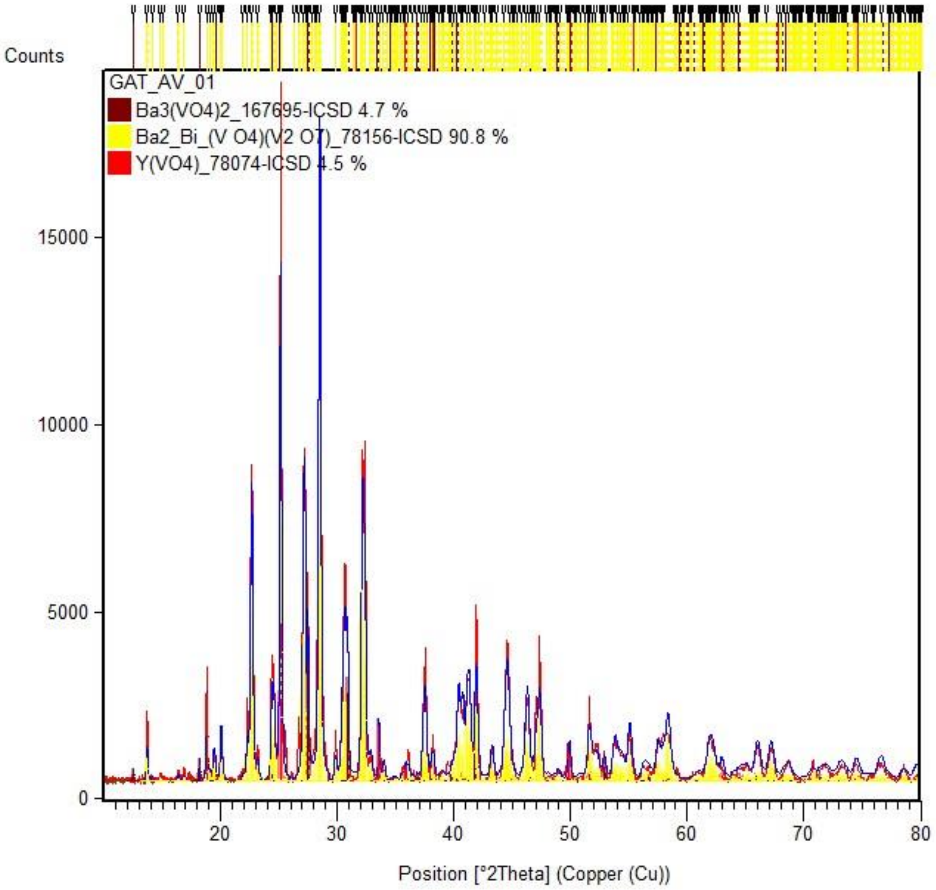

Figure 4.6: XRD spectrum with Rietveld refinement of $Ba_2YV_3O_{11}$ with 0 mol% Sm^{3+} ions after sintering

The crystallographic characterization of the sintered sample without any samarium ions reveals a totally different composite now. Figure 4.6 demonstrates three different phases, in which the bismuth complies with Yttrium again. As expected after the sintering process the part of the desired $Ba_2YV_3O_{11}$ phase has been increased. This proves that the actual product formation will not take place until the substrate is heated at a required temperature for a certain time. As you can see it yielded about 90 % of the intended $Ba_2YV_3O_{11}$ phase. Furthermore, no starting materials are present in the product anymore. They are completely converted into $Ba_2YV_3O_{11}$, $Ba_3(VO_4)_2$ and $Y(VO_4)$.

However, it is worth mentioning that the percentage shares of the single phases in the XRD spectrum can deviate from the real composition. Figure 4.6 exhibits a lot of peaks and the overlap of several small and some larger peaks. Due to these overlaps many peaks could not be identified and consequently they can have an impact on the outcome. This statement is valid in all the XRD spectra presented.

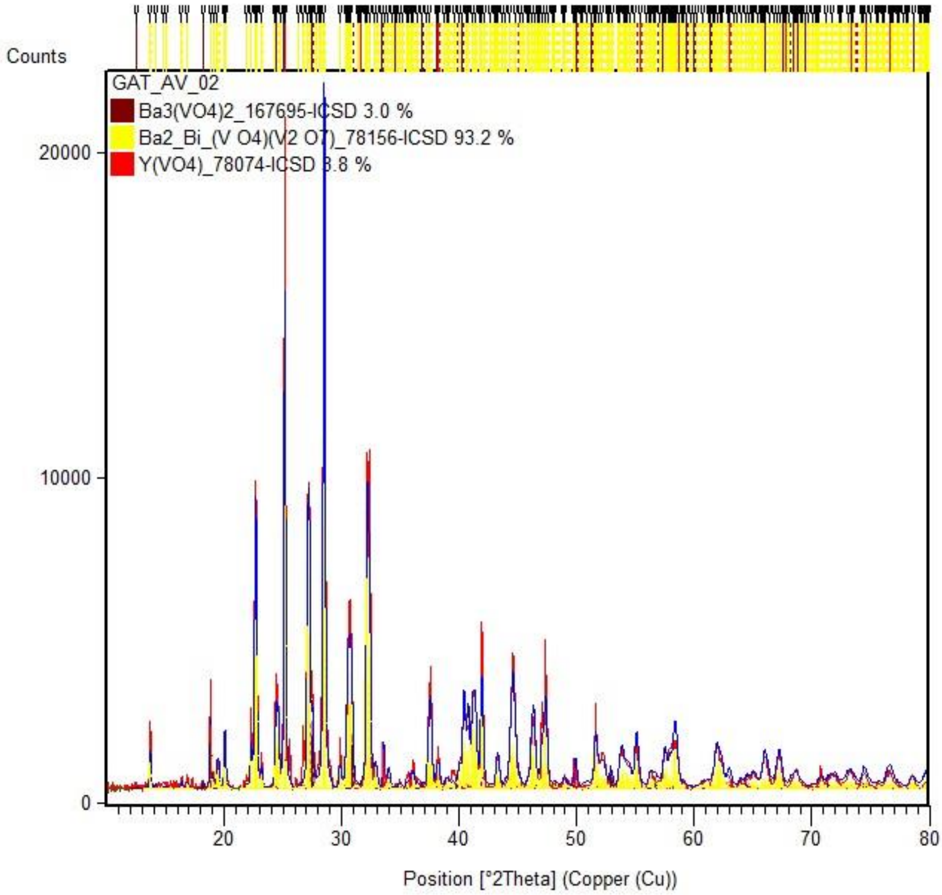

Figure 4.7: XRD spectrum with Rietveld refinement of $Ba_2YV_3O_{11}$ with 1 mol% Sm^{3+} ions after sintering

Figure 4.7 exhibits the crystallographic phase composition of the sintered $Ba_2YV_3O_{11}$ doped with 1 mol% Sm^{3+} ions. Compared to Figure 4.5, which is the same sample prior to the sintering process, Figure 4.7 offers a composite of three different phases. Most part of the powder consists of approximately 93% $Ba_2YV_3O_{11}$ which is a very successful result. Additional phases like yttrium and barium vanadates are generated too. Furthermore, no significant influence on the crystal structure can be observed due to the added samarium ions in the crystal lattice. The reactants undergo again an entire conversion during the sintering step.

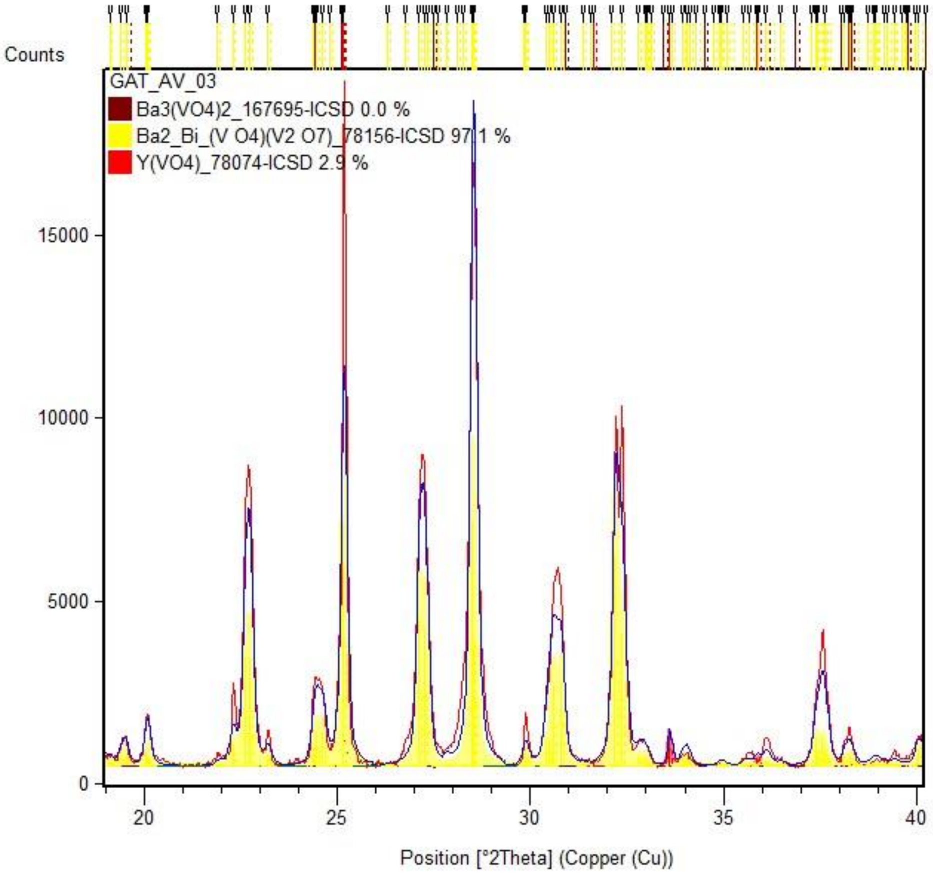

Figure 4.8: XRD spectrum with Rietveld refinement of $Ba_2YV_3O_{11}$ with 2 mol% Sm^{3+} ions after sintering

The XRD spectrum in Figure 4.8 shows the composition of the sintered doped $Ba_2YV_3O_{11}$ with a concentration of 2 mol% Sm^{3+} ions in more detail than the spectra before. Only the important °2Theta range is shown. As well as the 1 mol% Sm^{3+} sample, the 2 mol% Sm^{3+} sample has a high amount of the desired product phase. However, the powder does not include any barium vanadate fraction. With increasing amount of the doping element, the content of the $Ba_2YV_3O_{11}$ phase is raised.

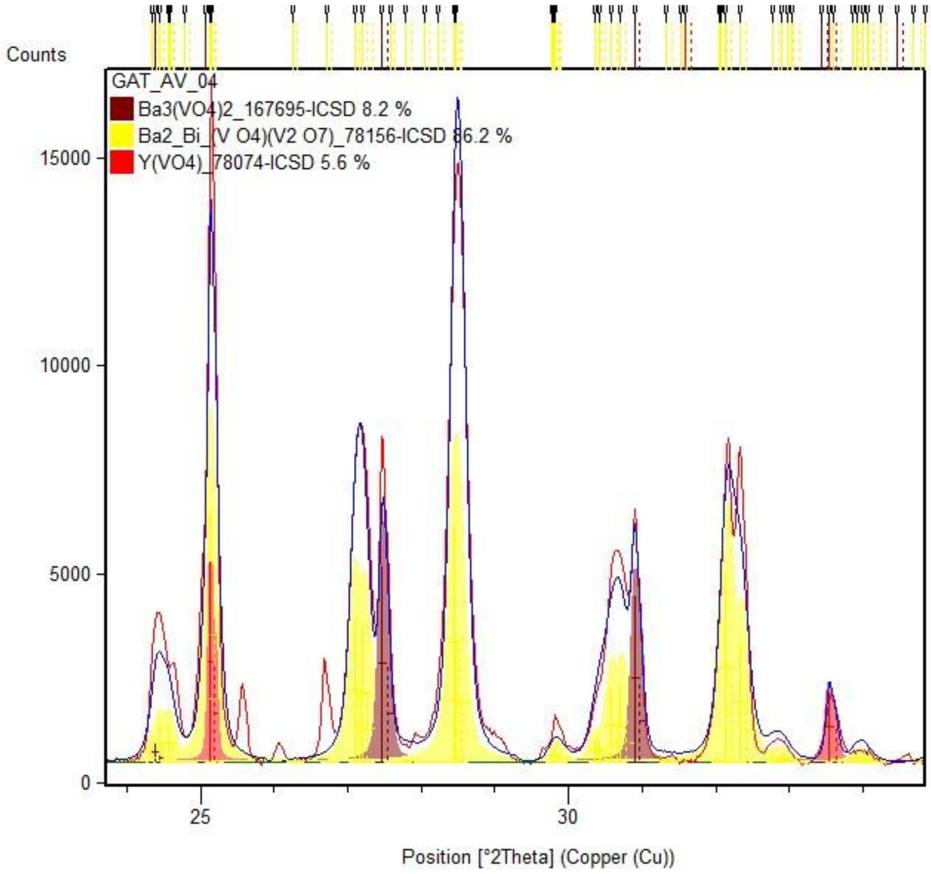

Figure 4.9: XRD spectrum with Rietveld refinement of $Ba_2YV_3O_{11}$ with 3 mol% Sm^{3+} ions after sintering

Similar to the spectrum of the 2 mol% doped Sm^{3+} sample, the sintered $Ba_2YV_3O_{11}$ phosphor with 3 mol% Sm^{3+} ions are illustrated in Figure 4.9 in a smaller °2Theta range. With the doping concentration of 3 mol% the content of the intended product phase is decreased again. In addition, the barium and the yttrium vanadate phase are present in a higher amount as in the sintered samples before. However, the $Ba_2YV_3O_{11}$ fraction is still the predominant phase.

Furthermore, the Scherrer equation was used to estimate the particle size of the four sintered powders.

$$D = \frac{K \cdot \lambda \cdot 57.3}{FWHM(net) \cdot cos\theta} \tag{4}$$

For each sample three distinct peaks (at 27.1, 28.5 and 33.2 °2Theta) were used for the calculation of the particle size. After that, the average of the three particle size values from one sample was calculated. The average size of the particles ranges from 55 to 73 nm which is a satisfying result because the particles a thus produced in nanoscale. Furthermore, it is in accordance with the literature value of an average particle size of 44 nm [72]. Although the gained particle sizes are slightly larger, they are in the same order of magnitude which demonstrates the success of the processing procedure.

4.2 Dy^{3+} and Tm^{3+} doped $GdAl_3(BO_3)_4$ prepared with Solution Combustion Method

4.2.1 Characterization with UV-lamp

A few intermediate products (before the sintering process) exhibited an orange luminescence when they were illuminated with light with a wavelength of 254 nm. The sample which was only doped with Dy^{3+} has a light orange glow, while the sample which was only doped with Tm^{3+} shined also orange but with a much weaker intensity. All other intermediate products that were doped with both rare earth elements did not show a bright luminosity. The 3 mol% Dy^{3+} and 1 mol% Tm^{3+} samples showed only just a very weak orange luminescence. The residual intermediates did not exhibit any luminosity after excitation with 254 nm. The irradiance with light with a wavelength of 365 nm of the whole concentration series of the Dy^{3+} and Tm^{3+} doped $GdAl_3(BO_3)_4$ (GAB) did not initiate an excitation and therefore no characteristic glow was observed.

The sintered substrates were investigated with the same wavelengths. The Dy^{3+} doped product glowed yellow under illumination with 254 nm and with a weaker intensity with an excitation of 365 nm. The sintered GAB with Tm^{3+} ions did not show any fluorescence.

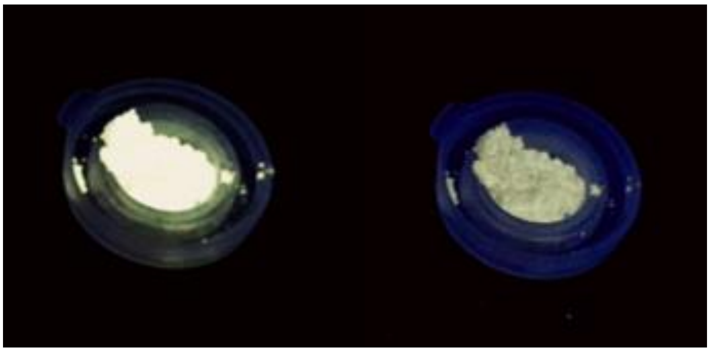

Figure 4.10: Luminosity of the sintered 3 mol% Dy^{3+} and 1 mol% Tm^{3+} doped $GdAl_3(BO_3)_4$ sample. On the left side the phosphor was illuminated with a wavelength of 254 nm and on the right side it was illuminated with a wavelength of 365 nm.

The sintered products with both rare earth doping elements revealed a yellow shine upon excitation with a wavelength of 254 nm such as the phosphor on the left side in Figure 4.10. The intensity of the yellow glow increased with higher Tm^{3+}-concentration. The excitation with 365 nm caused a pale-yellow/ white luminosity. The intensity decreased with increasing the Tm^{3+}-concentration. Due to the higher amount of Tm^{3+}, concentration quenching occurred leading to a lower fluorescence intensity.

The color and the brightness of the powder in the picture above is slightly altered by the camera used again.

4.2.2 Characterization with Reflectance Spectroscopy

The reflectance spectra of the 3 mol % Dy^{3+} doped $GdAl_3(BO_3)_4$ and the 3 mol% Dy^{3+} and 1 mol% Tm^{3+} doped $GdAl_3(BO_3)_4$ are shown in Figure 4.11. The spectra show only transitions of Dy^{3+} and Tm^{3+} in the near-infrared range. The visible range was neglected, because no transitions could be observed due to reflectance measurements.

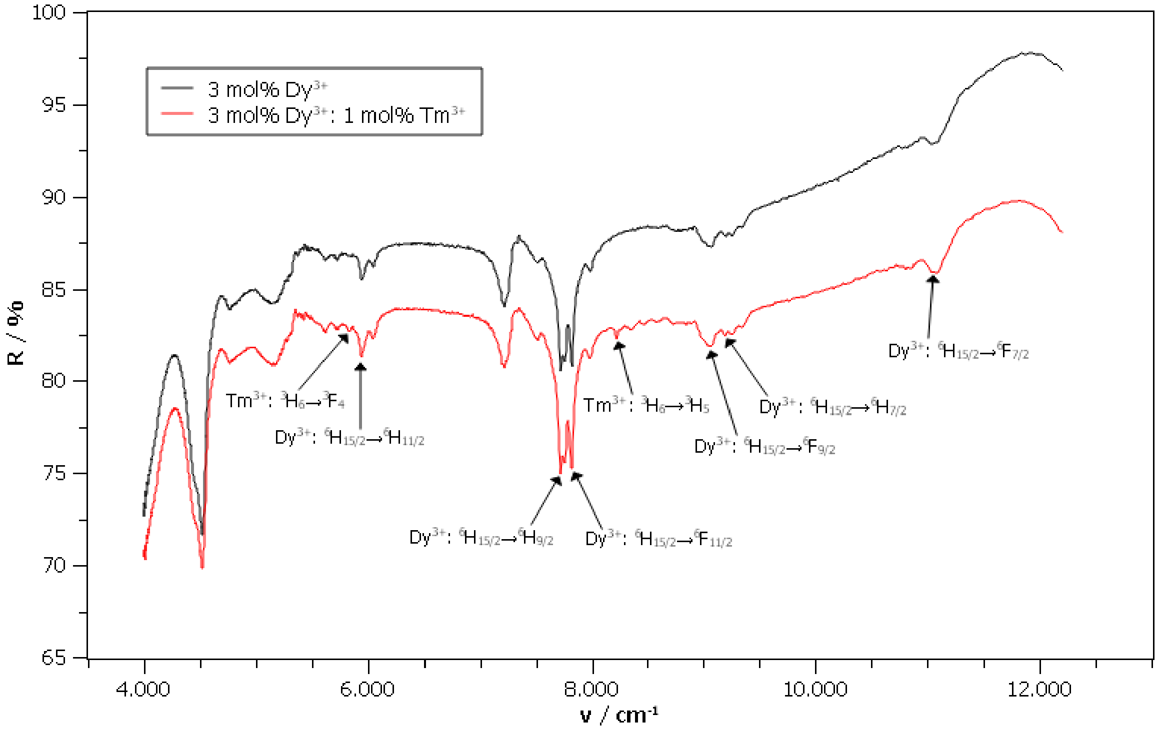

Figure 4.11: Reflectance spectra of 3 mol% Dy^{3+} doped $GdAl_3(BO_3)_4$ and 3 mol% Dy^{3+} and Tm^{3+} doped $GdAl_3(BO_3)_4$ powders in NIR range

The black curve in Figure 4.11 represents the $GdAl_3(BO_3)_4$ phosphor with 3 mol% Dy^{3+}. It exhibits some peaks corresponding to transitions from the ground state $^6H_{15/2}$ to several higher energy levels in the range of about 5000 to 11000 cm^{-1}. The red curve represents the sample with additional 1 mol% Tm^{3+} ions. It reveals the same peaks from Dy^{3+} as the black curve and two further peaks from Tm^{3+}, comply with transitions from the ground state $^3H_6$ to $^3H_5$ and $^3F_4$ energy levels.

Both spectra of the phosphors illustrate some peaks, which could not be identified by energy state transitions of the two rare earth metal dopants. Therefore, these less specific peaks can be produced due to overtones and vibrational combinations of the crystal lattice units again.

4.2.3 Characterization with Fluorescence Spectroscopy

The Dy^{3+} and Tm^{3+} doped $GdAl_3(BO_3)_4$ samples after sintering were characterized with fluorescence spectroscopy and their spectra are illustrated in Figure 4.12.

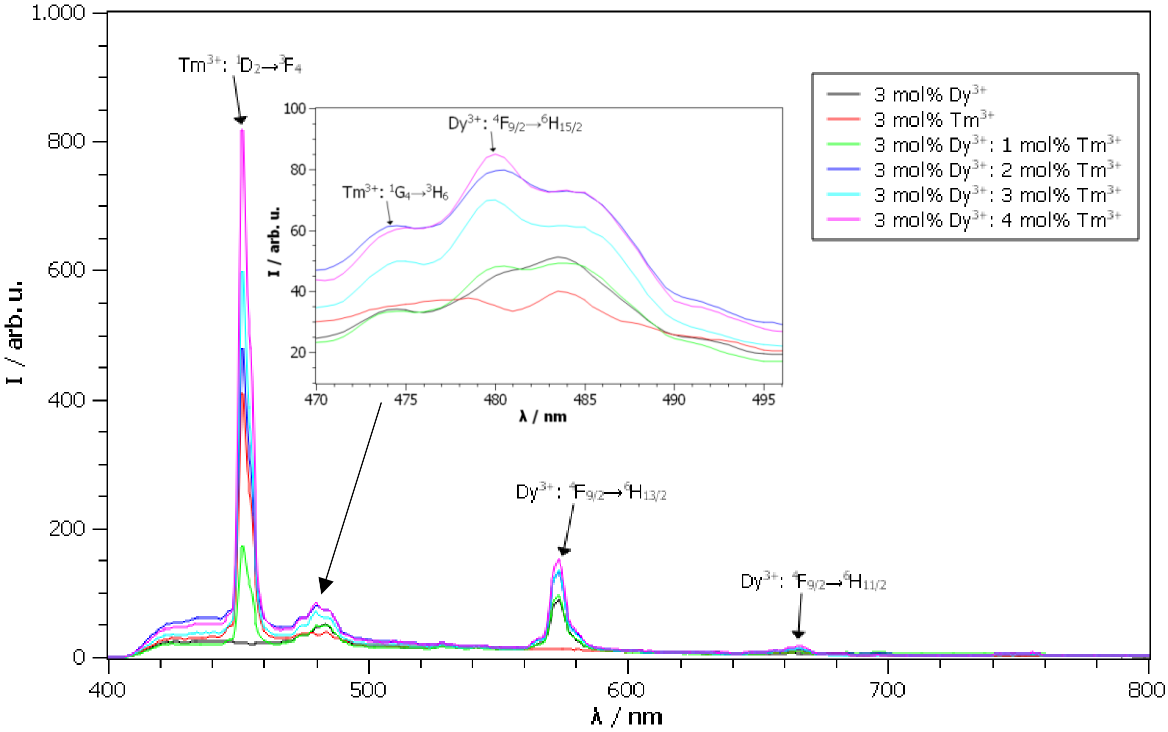

Figure 4.12: Emission spectra of sintered Dy^{3+} and Tm^{3+} doped GAB powders with different Dy^{3+}- and Tm^{3+}- concentrations as activator ions

Figure 4.12 shows also a magnified illustration of the peaks between 470 to 495 nm, which helps to assign the energy level transitions of Dy^{3+} and Tm^{3+}. The black curve represents the phosphor that is doped with 3 mol% Dy^{3+}. It reveals the three characteristic transitions from the excited state $^4F_{9/2}$ to $^6H_{15/2}$, $^6H_{13/2}$ and $^6H_{11/2}$. The $^4F_{9/2}$ to $^6H_{15/2}$ transfer occurs at a wavelength of about 480 nm, corresponding to blue light emission. The second dominant emission band of the black curve is at approximately 570 nm. This emission band belongs to the $^4F_{9/2}$ to $^6H_{13/2}$ transition and generate a yellow emission. As you can see, the intensity of the yellow peak is higher than of the blue peak. Furthermore, a very small peak is observed at about 665 nm, which is due to the relaxation from $^4F_{9/2}$ to $^6H_{11/2}$ state. The emission band produced by this transition lies in the red range of the visible spectrum. However, the contribution to the overall emission color of the phosphor is very weak, because of the weak intensity. As mentioned before, the intensity of the yellow emission band is stronger than of the blue one. Consequently, the Dy^{3+} doped $GdAl_3(BO_3)_4$ phosphor generates a yellowish light rather than a pure white light. The reason for that is, that the yellow emission band is hypersensitive to the $GdAl_3(BO_3)_4$ host environment. Therefore, co-doping with Tm^{3+} can introduce the missing amount of blue radiation.

The red curve in Figure 4.12 represents the 3 mol% Tm^{3+} doped $GdAl_3(BO_3)_4$ sample. The spectrum shows a significant peak at about 450 nm corresponding to the $^3D_2$ to $^3F_4$ transition and a smaller peak at about 475 nm corresponding to the $^1G_4$ to $^3H_6$ transfer of Tm^{3+}. Both relaxation processes generate blue light emission. There are no further emission bands in the yellow or red regions. Thus, the phosphor should offer a blue light after excitation. However, the characterization with UV-light illumination exhibits no luminescence behavior.

The residual spectra belong to 3 mol% Dy^{3+} doped $GdAl_3(BO_3)_4$ with different Tm^{3+} ions concentrations. These curves show the already mentioned transitions from Dy^{3+} and Tm^{3+} as expected. Due to that, the yellow light emission, which is dominant in the 3 mol% Dy^{3+} doped phosphor, is compensated by the blue emission portion of Tm^{3+}. The increase of the Tm^{3+} concentration effects the increase of the intensity of the blue emission band at 450 nm, whereas the intensity of the yellow emission band at 570 nm is only slightly influenced. The addition of Tm^{3+} shifts the color coordinates of the phosphor to the blue range and thus it can tune the emission color to purer white light. However, if the Tm^{3+} amount is too high, it effects a general blue emission of the phosphor. As it can be seen in Figure 4.12, the phosphors with 3 and 4 mol% Tm^{3+} exhibit a strong and dominant peak at 450 nm, which results in a larger contribution of the blue emission. Therefore, a doping concentration of 1 or maximum 2 mol% Tm^{3+} would be optimal to generate white light emission.

4.2.4 CIE Color Coordinates and Color Chart

The obtained chromaticity values for the sintered Dy^{3+} and Tm^{3+} co-doped $GdAl_3(BO_3)_4$ samples are shown in the 1931 CIE color chart in Figure 4.13.

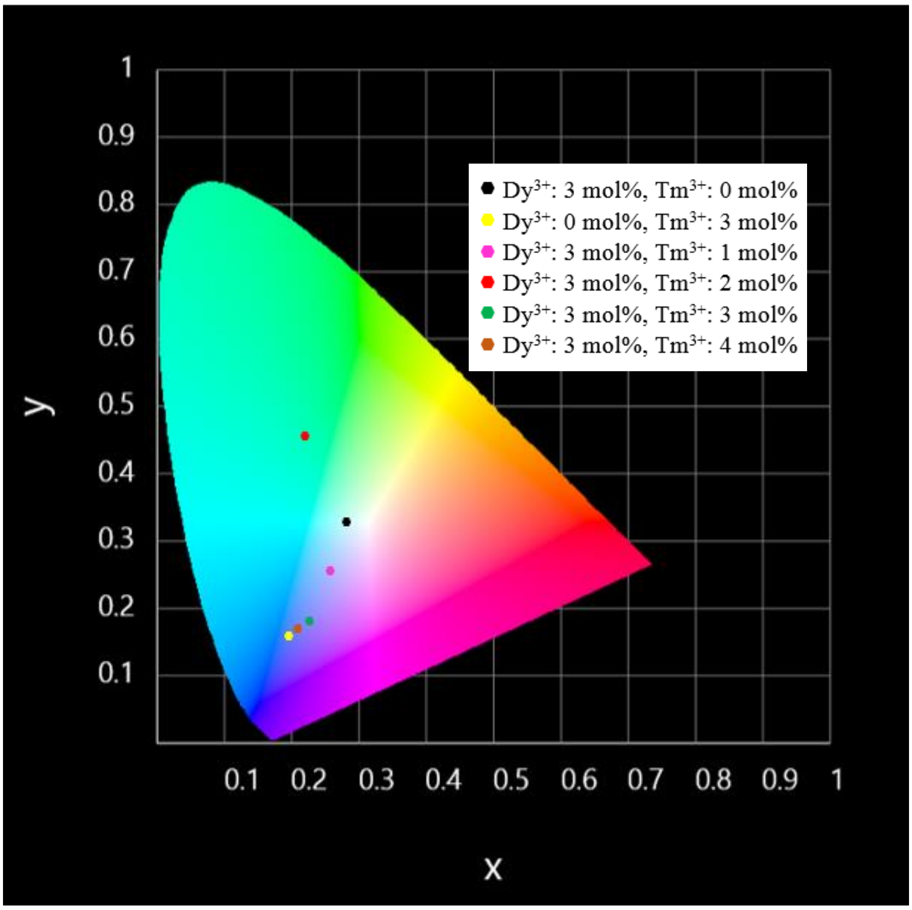

Figure 4.13: 1931 CIE color chart with marked chromaticity values of the sintered Dy^{3+} and Tm^{3+} doped $GdAl_3(BO_3)_4$ phosphors

The differently-colored dots in Figure 4.13 demonstrate the x, y and z color coordinates of the experimental series. Each dot represents a sample with a specific doping concentration of Dy^{3+} and Tm^{3+}. The black point marks the chromaticity coordinates of the sample, which is only doped with Dy^{3+}.

It is very near the achromatic point. In contrast the yellow point, that marks the Tm^{3+} doped sample, is shifted into the blue area. The chromaticity values of all other samples, that are doped with both rare earth metals, are between these two points, except the 3 mol% doped Dy^{3+} and the 2 mol% Tm^{3+} sample. Hence, a tendency can be observed in the sample series due to the different concentrations. A higher amount of Tm^{3+} ions effects a displacement to the blue range and the part of emitting blue light is increased. The color coordinates of the 3 mol% doped Dy^{3+} and the 2 mol% Tm^{3+} sample are in the green region, which is indicated through the red dot. The values of this sample differ significantly from the other samples in this series. Therefore, an error in the sample preparation cannot be excluded.

4.2.5 Crystallographic Characterization

The crystallographic characterization by XRD measurements was carried out with four selected samples before and four selected samples after the sintering step.

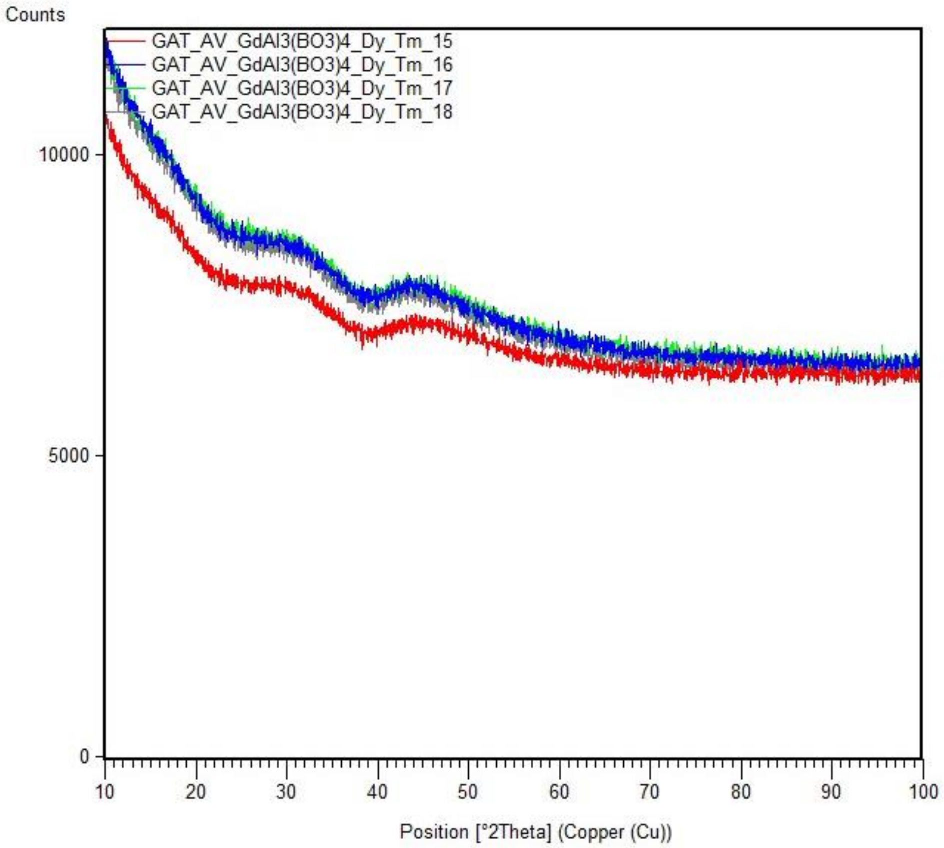

Figure 4.14: XRD spectrum with Rietveld refinement of four $GdAl_3(BO_3)_4$ samples before sintering. The concentration of Dy^{3+} is in each sample 3 mol% while the Tm^{3+}-concentration varies. Number 15 is 0 mol% Tm^{3+}, Number 16 is 1 mol% Tm^{3+}, Number 17 is 2 mol% Tm^{3+} and Number 18 is 4 mol% Tm^{3+}.

Figure 4.14 shows the XRD spectrum of the four unsintered substrates. All substrates show the same curve without any peaks and therefore no phases could be identified. That means that the samples are x-rays amorphous and have no crystallinity. This is explainable because the conversion of the $GdAl_3(BO_3)_4$ takes only place during the sintering at 1100°C. Consequently, the incorporation of the doping elements does also not occur before the heat-treatment are carried out. Hence, the mere combustion reaction does not generate the desired product. The following sintering process is a mandatory step which leads to the manufacture of the $GdAl_3(BO_3)_4$ phosphor.

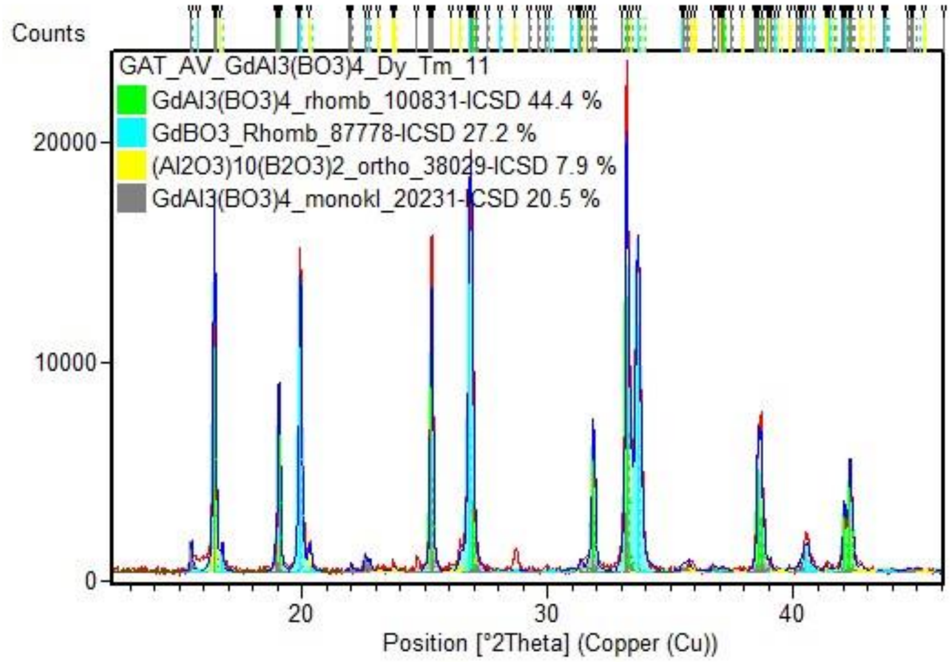

Figure 4.15: XRD spectrum with Rietveld refinement of $GdAl_3(BO_3)_4$ with a concentration of 3 mol% Dy^{3+} ions and 0 mol% Tm^{3+} ions after sintering

Figure 4.15 represents a rough phase distribution of the sintered $GdAl_3(BO_3)_4$ with Dy^{3+} as doping element. No Tm^{3+} ions are present in this samples. As can be seen from the crystal structure determination the Dy^{3+} is not considered, which means that the doping element has no significant influence on the crystal lattice. This is the same conclusion as at the Sm^{3+} doped $Ba_2YV_3O_{11}$ before. Additionally, no impact of the doping element on the lattice constants was recognizable.

The XRD spectrum reveals four different phases, from which two phases are the $GdAl_3(BO_3)_4$ once in rhombohedral and one in monoclinic form. However, the monoclinic phase is overrepresented due to the high intensity of the first peak. It is assumed that the determined amount of 20.5% of the monoclinic $GdAl_3(BO_3)_4$ phase is not correct. This phase probably exists in a much lower quantity in the product.

Furthermore, a rhombohedral $GdBO_3$ phase was determined with an approximate amount of 27.2% and an orthogonal $(Al_2O_3)_{10}(B_2O_3)_2$ phase with a share of 7.9% was identified. These are also only rough assessments and therefore the obtained values can deviate from the real amounts of these phases in the product. In addition, overlaps of some peaks occur which make it hard to identify them. This leads again to possible deviations of the obtained values. However, the overlaps are not as drastic as in the $Ba_2YV_3O_{11}$ samples and thus the impact is not so rigorous. This is the case in all following XRD spectra.

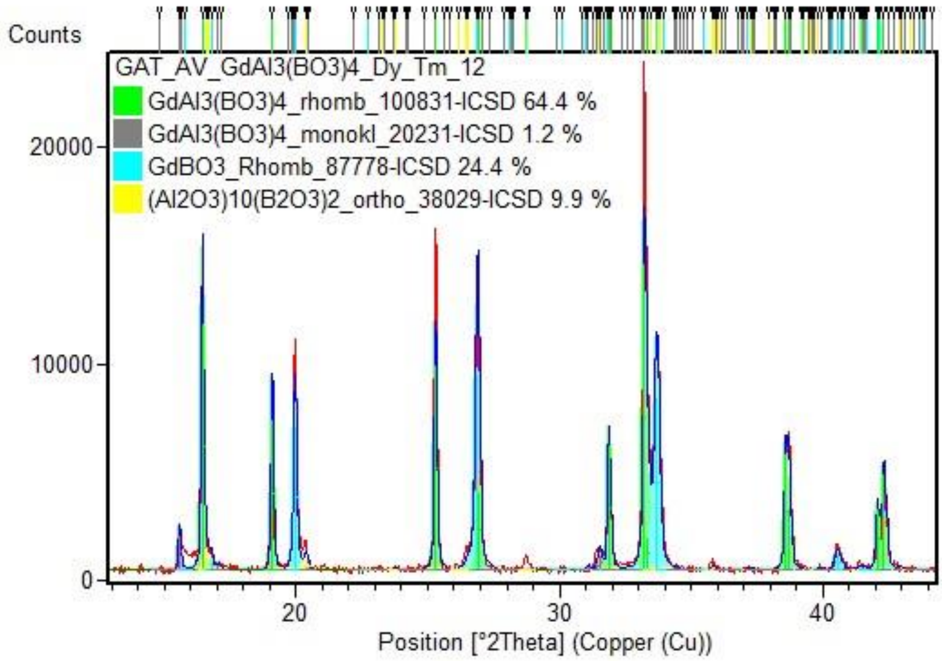

Figure 4.16: XRD spectrum with Rietveld refinement of $GdAl_3(BO_3)_4$ with a concentration of 3 mol% Dy^{3+} ions and 1 mol% Tm^{3+} ions after sintering

The sintered sample with 3 mol% Dy^{3+} ions and 1 mol% Tm^{3+} ions consists of the same four phases as the sample without Tm before which is shown in Figure 4.16. However, the rhombohedral $GdAl_3(BO_3)_4$ phase is significantly represented in a higher portion with approximately 64.4%. In contrast, the amount of the monoclinic $GdAl_3(BO_3)_4$ phase is substantially lower in the product, which results in a better agreement with the real phase composition. The two other phases are found in the product with approximately the same amounts as in the sample before.

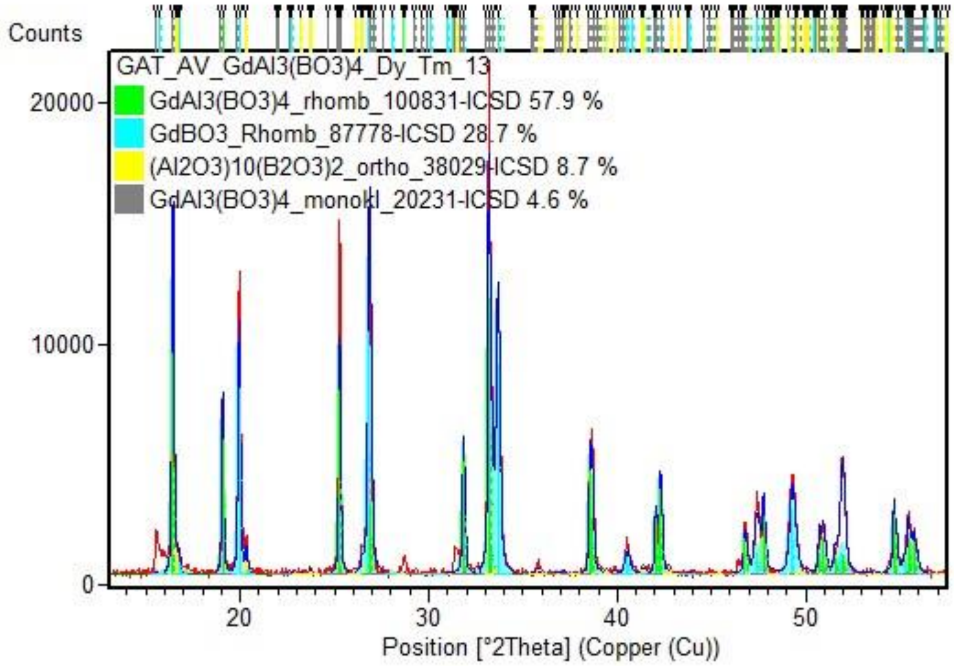

Figure 4.17: XRD spectrum with Rietveld refinement of $GdAl_3(BO_3)_4$ with a concentration of 3 mol% Dy^{3+} ions and 2 mol% Tm^{3+} ions after sintering

Approximately equal phase composition as shown in Figure 4.16 is found in the 3 mol% Dy^{3+} and the 2 mol% Tm^{3+} doped $GdAl_3(BO_3)_4$ after the sintering process, which can be seen in Figure 4.17.

There are only a few deviations of the percentage share of the rhombohedral and the monoclinic $GdAl_3(BO_3)_4$ phases. The amount of the monoclinic phase is slightly higher and consequently the rhombohedral one is slightly reduced.

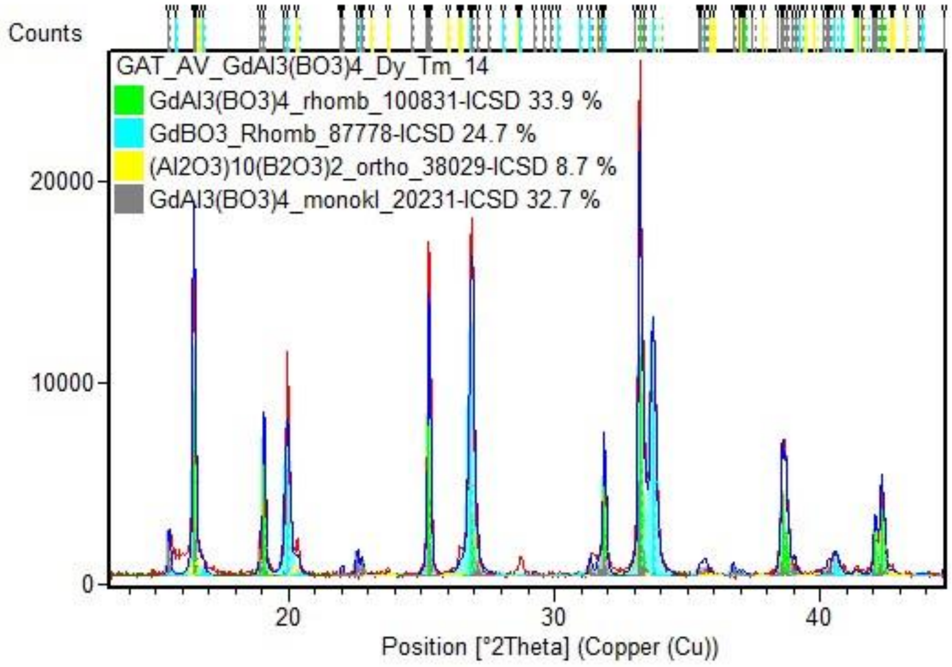

Figure 4.18: XRD spectrum with Rietveld refinement of $GdAl_3(BO_3)_4$ with a concentration of 3 mol% Dy^{3+} ions and 4 mol% Tm^{3+} ions after sintering

The XRD spectrum, which is illustrated in Figure 4.18 exhibits a completely different crystallographic phase distribution to the spectrum in Figure 4.17. The sintered $GdAl_3(BO_3)_4$ with a concentration of 3 mol% Dy^{3+} ions and 4 mol% Tm^{3+} ions consists of a significantly lower part of the rhombohedral $GdAl_3(BO_3)_4$ phase. In return the monoclinic $GdAl_3(BO_3)_4$ phase is present in a higher content again with approximately 32.7%. The amount of the other two phases correlates with the sintered samples before.

Equation 4 was used again to calculate the particle sizes of the sintered products. The calculation with the Scherrer equation provides a rough estimation again. For the determination of the particle sizes three pronounced peaks (16.4, 25.3 and 33.2 °2Theta) of a sample were chosen. Afterwards, the three obtained particles size values were used to calculate an average. The received average particle sizes of all four sintered powders ranges from 132 to 184 nm. However, these are no accurate values because the method with using the Scherrer equation is only a coarse determination.

4.3 Ce^{3+} doped $Y_3Al_5O_{12}$ prepared with Solution Combustion Method

4.3.1 Characterization with UV-lamp

The intermediate substrates were illuminated with light with a wavelength of 254 nm and 365 nm again. They did not exhibit a lightning luminosity, that means that the complete incorporation of the cerium ions into the crystal lattice do not take place until the sintering process is completed.

The sintered undoped $Y_3Al_5O_{12}$ powder did not show any radiance neither with an excitation wavelength of 254 nm nor 365 nm. The sintered Ce^{3+} doped products showed only a yellow glow when they were excited with a wavelength of 365 nm, which is illustrated in Figure 4.19 (powder on the right side).

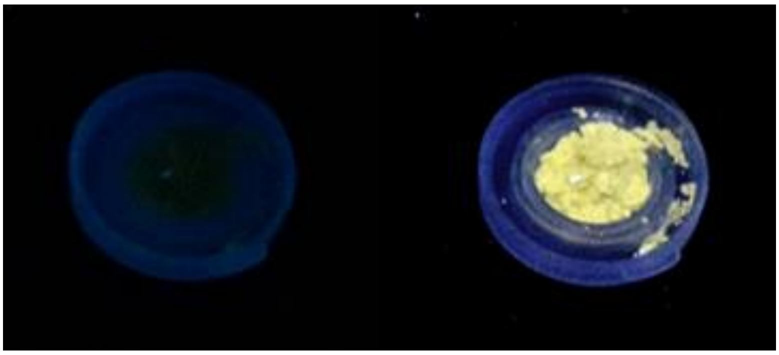

Figure 4.19: Luminosity of the sintered 1 mol% Ce^{3+} doped $Y_3Al_5O_{12}$ sample. On the left side the phosphor was illuminated with a wavelength of 254 nm and on the right side it was illuminated with a wavelength of 365 nm.

However, no distinction of the luminosity between the different samples were observed with the naked eye. Therefore, a concentration quenching due to an increase of the amount of Ce^{3+} ions could not be identified without any spectroscopic measurements.

4.3.2 Characterization with Reflectance Spectroscopy

The reflectance spectra with all transitions in the visible and the near-infrared range after illumination with light of the undoped and Ce^{3+} doped YAG are shown in Figure 4.20.

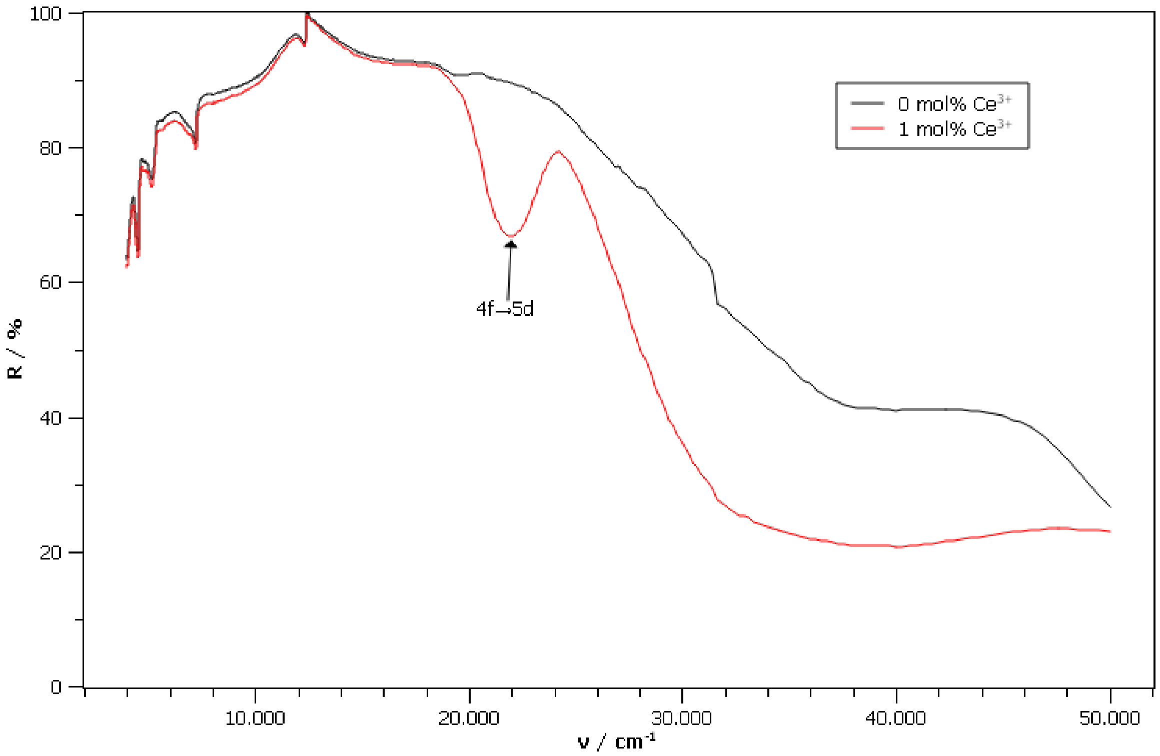

Figure 4.20: Reflectance spectra of undoped YAG and 1 mol% Ce^{3+} doped YAG powders in the visible and near-infrared range. The detector change occurs at approximately 12 000 cm^{-1}.

The black curve in Figure 4.20 represents the sintered undoped YAG material, whereas the red curve marks the sintered Ce^{3+} doped YAG phosphor. The characteristic 4f-5d transition, that occurs only in the doped compound is clearly identifiable by the broad peak of the red curve at a wavenumber of around 20 000 to 23 000 cm^{-1}, which lies in the visible region. The undoped material does not show any peak in this area, because of the absence of the activator ions.

The peaks of both samples in the NIR region coincide. They cannot assign to any energy level transitions of the Ce^{3+} ions. Hence, it is assumed that these peaks belong to overtones and vibrational combinations of the crystal lattice units again.

It should be noted, that there is a detector change at approximately 810 nm, which can be seen by a leap in the spectra of both curves at around 12 000 cm^{-1}. At this point, the reflectance spectrometer switches from the InGaAs detector to the photomultiplier tube detector.

4.3.3 Characterization with Fluorescence Spectroscopy

Figure 4.21 exhibits the emission spectra of the sintered undoped YAG and all sintered Ce^{3+} doped YAG samples with an excitation wavelength of 343 nm.

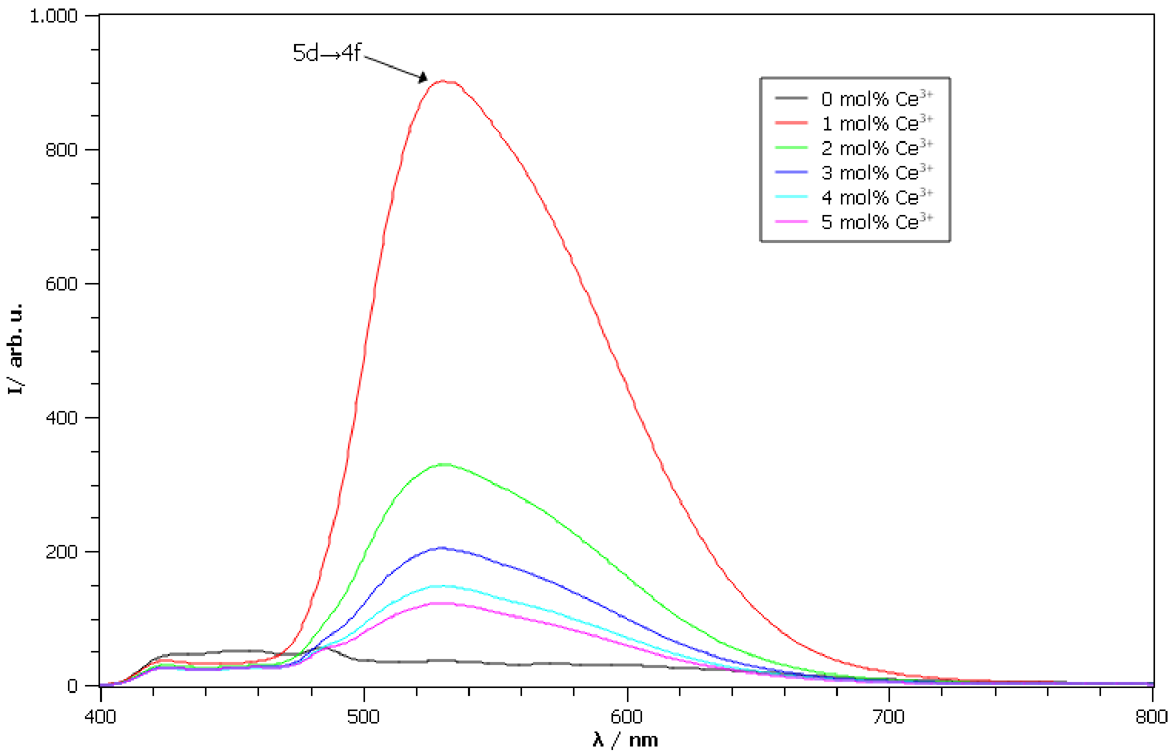

Figure 4.21: Emission spectra of sintered Ce^{3+} doped YAG powders with different Ce^{3+}-concentrations as activator ions

The emission spectrum of the sintered undoped yttrium aluminum garnet reveals no fluorescence peak in the green/yellow range (black curve). It only shows a broader emission band with a very low intensity in the blue region. Without any activator ions a glow of the yttrium aluminum garnet after excitation is not possible. The Y^{3+} ions do not have any transitions with an energy release, which correspond to the emission of visible light. This is also confirmed through the characterization with the UV-lamp, where no luminescence could be observed.

Due to the addition of the Ce^{3+} ions the material is able to glow, which is due to the 5d-4f transition of the electron of the cerium ion. The interplay of the host material (YAG) and the activator ions (Ce^{3+}) causes an energy state lowering of the 5d-levels, which makes the emission of energy as visible light possible. The gap between the 5d- and the 4f-levels is now reduced and the transition from the 5d- to the 4f-states corresponds to the radiation of green and yellow light. This can be seen by all colored curves in Figure 4.21, where cerium ions are used as dopant. All these curves exhibit a broad peak from approximately 490 nm to 640 nm being in the most part of the green and yellow range of the color spectrum.

The 1 mol% Ce^{3+} doped YAG phosphor (red curve in Figure 4.21) shows the highest emission intensity of all phosphors of the sample series. This compound possesses the smallest doping element concentration but exhibits the highest emission efficiency. Due to an increase of the cerium ions concentration the intensity of the luminescence decreases. This trend is attributed to a concentration quenching of the activator ions. Higher quantities of Ce^{3+} ions in the host material effects shorter average distances between themselves resulting in more frequent radiation- free transfers into the ground state.

4.3.4 CIE Color Coordinates and Color Chart

The following figure illustrates the results of the color measurements and the calculations of the Ce^{3+} doped $Y_3Al_5O_{12}$ samples after the heat treatment.

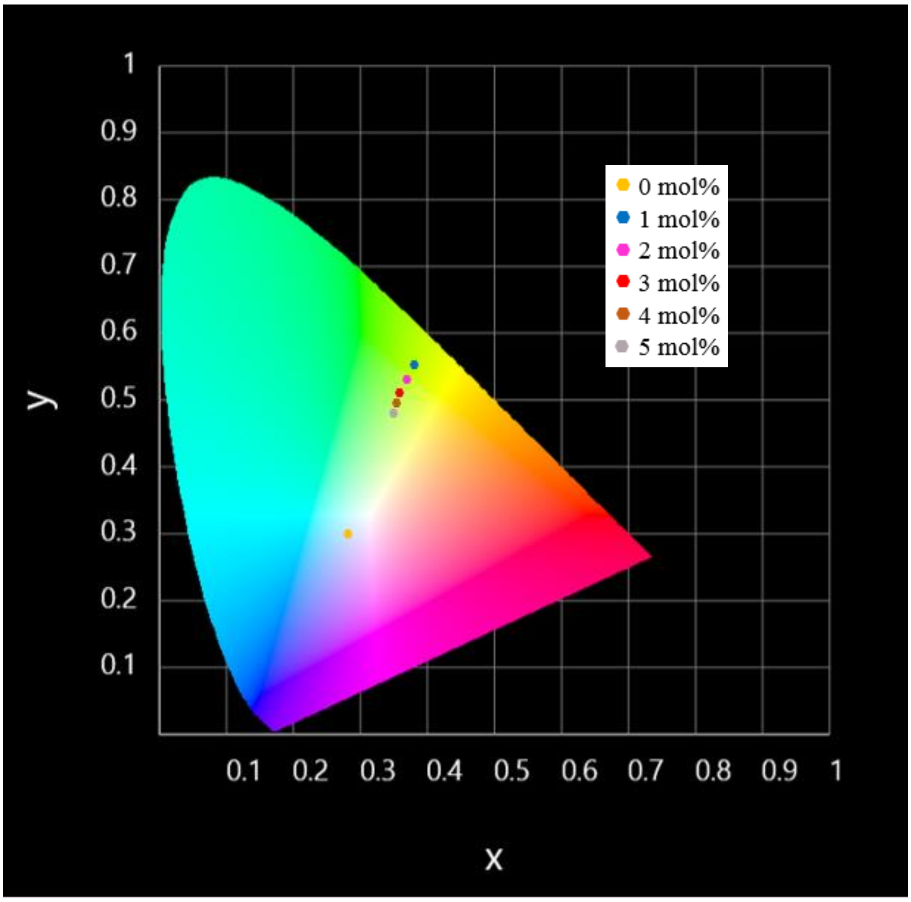

Figure 4.22: 1931 CIE color chart with marked chromaticity values of the sintered Ce^{3+} doped $Y_3Al_5O_{12}$ phosphors

Figure 4.22 exhibits the 1931 CIE color chart with the chromaticity values of all samples. Every dot represents the chromaticity values of a sintered powder of the sample series. The color coordinates of the Ce^{3+} doped $Y_3Al_5O_{12}$ samples are close to each other and lie in the yellow region of the color chart, which is marked through the different colored dots. As can be seen, the dots are on the border to the light green range and the yellow area. This discovery matches with the observation through illumination under the UV-light with 365 nm, that reveals a yellow glow. Additionally, the emission spectra of the fluorescence spectroscopy also showed a broad peak in the green and yellow range of the visible spectrum. The calculation of the chromaticity values of the sample series and their position in the color chart represents the emission behavior of yellow/green light again.

The light orange point, that depicts the undoped $Y_3Al_5O_{12}$ sample lies very close to the achromatic point, which is not only the position of the color white, but as well the position of the color black. The illumination with UV-light causes no glow of this powder. The incorporation of the Ce^{3+} ions into the crystal lattice only leads to the radiance behavior and causes a displacement to the yellow range. The merely undoped powder could not be used as light emitting materials.

The points in Figure 4.22 shows also a tendency of the various concentrations of the doping element. The 1 mol% doped Ce^{3+} sample has the highest chromaticity values x and y and consequently the most intensive yellow glow. It is indicated through the blue point in the intensive yellow part of the chart. With increasing the Ce^{3+} ions concentration the chromaticity values x and y decrease. Due to this raised amount of the doping element the color coordinates are shifted to the lighter yellow area, which is well recognized through the colored points in the figure. The higher the doping concentration of the $Y_3Al_5O_{12}$ sample, the stronger the concentration quenching through the Ce^{3+} ions, resulting in diminishing the luminosity of the material.

4.3.5 Crystallographic Characterization

Due to the crystallographic results of the intermediate products of the sample series with $GdAl_3(BO_3)_4$, the $Y_3Al_5O_{12}$ substrates before the sintering process were not characterized by XRD measurements. It was assumed that the unsintered $Y_3Al_5O_{12}$ intermediates do not show any crystallinity before they undergo a heat treatment and consequently they were x-rays amorphous too. Therefore, only four sintered samples of these experimental series were measured.

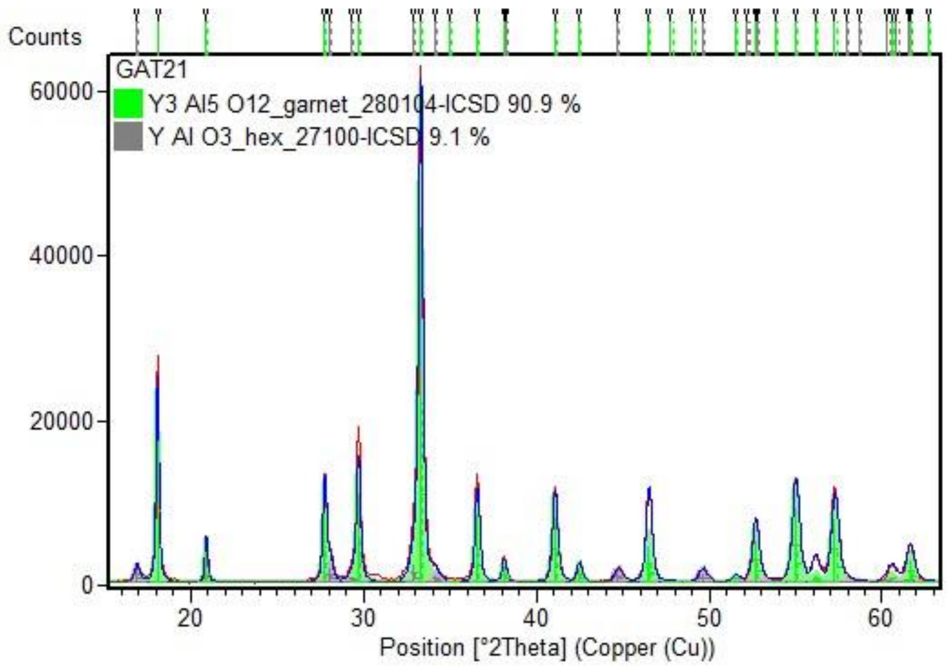

Figure 4.23: XRD spectrum with Rietveld refinement of $Y_3Al_5O_{12}$ with 0 mol% Ce^{3+} ions after sintering

Figure 4.23 illustrates the XRD spectrum of the undoped $Y_3Al_5O_{12}$ after the heat treatment at 900°C. The spectrum shows relative sharp peaks and represents a high crystallinity. As can be seen only two phases were determined from which one of them is the desired $Y_3Al_5O_{12}$ phase. This phase contributes with more than 90 % to the product composition. Further, the sintered product consists of a low part of a hexagonal $YAlO_3$ phase with 9.1%.

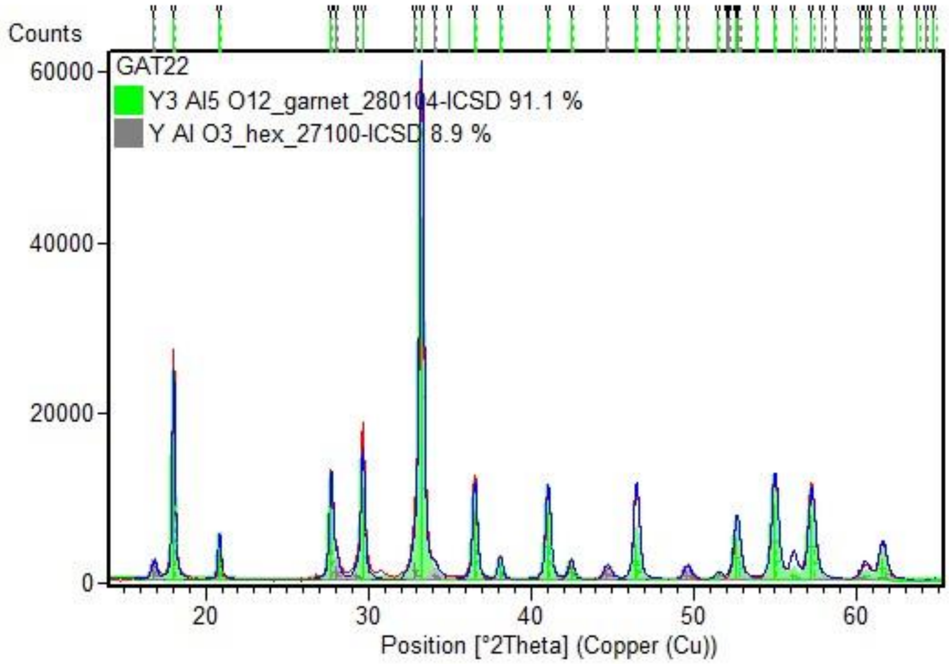

Figure 4.24: XRD spectrum with Rietveld refinement of $Y_3Al_5O_{12}$ with 1 mol% Ce^{3+} ions after sintering

In general, the added Ce^{3+} ions have no effect on the crystal lattice of the $Y_3Al_5O_{12}$ which is illustrated in Figure 4.24. The XRD spectrum exhibits sharp and well separated peaks again and the crystallinity of the product is high too. Although the product was doped with 1 mol% Ce^{3+} ions, the amount of the $Y_3Al_5O_{12}$ phase and the hexagonal $YAlO_3$ phase are quite the same as in the undoped sample. Hence, no significant influence could be observed.

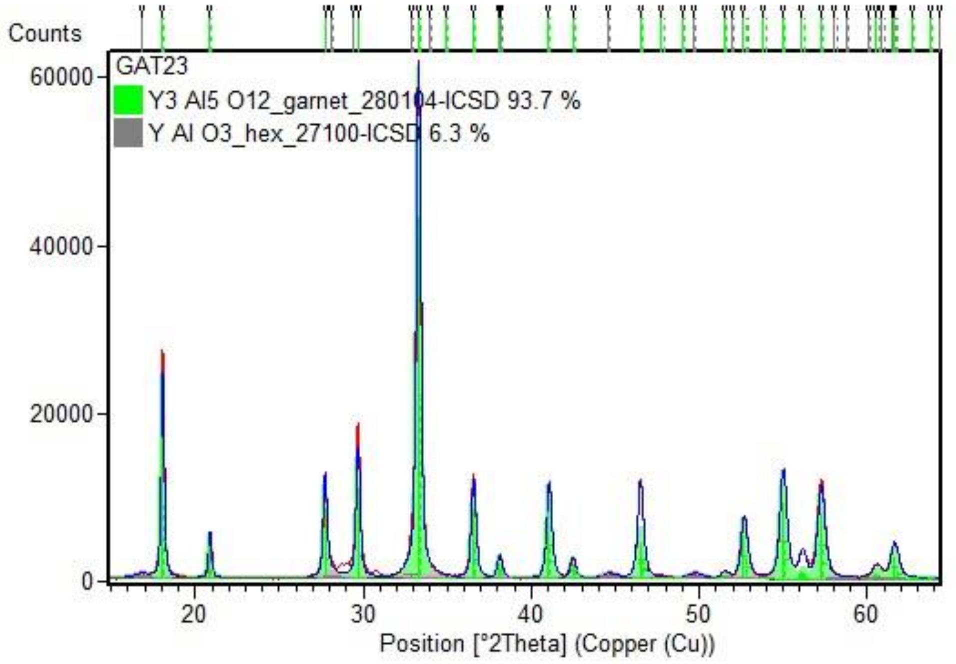

Figure 4.25: XRD spectrum with Rietveld refinement of $Y_3Al_5O_{12}$ with 2 mol% Ce^{3+} ions after sintering

A higher concentration of the doping element has an influence on the percentage shares of the two phases that can be shown in Figure 4.25. The percentage share of the $Y_3Al_5O_{12}$ phase is slightly higher and subsequently the one of the hexagonal $YAlO_3$ phase is reduced. Although the increase of the $Y_3Al_5O_{12}$ phase is not extremely rigorous, the doping element quantity weakly affects the phase distribution. However, there are no anomalies according to the crystal structure and the lattice constants through the added Ce^{3+} ions. The higher doping element concentration offers an advantage in the decrease of the hexagonal phase.

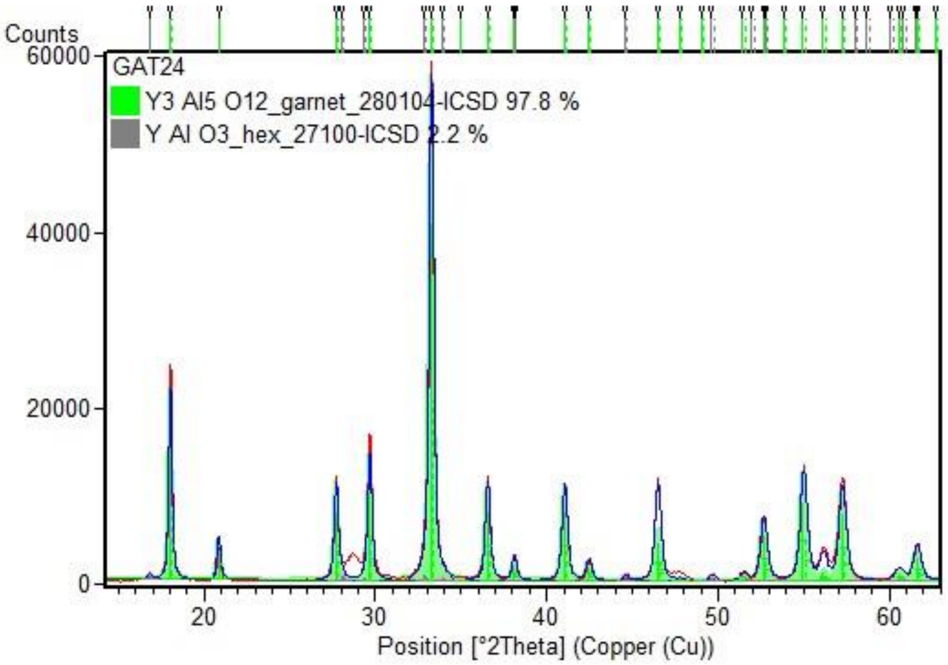

Figure 4.26: XRD spectrum with Rietveld refinement of $Y_3Al_5O_{12}$ with 4 mol% Ce^{3+} ions after sintering

Figure 4.26 demonstrates the XRD spectrum of the 4 mol % Ce^{3+} doped $Y_3Al_5O_{12}$ product. The same as before, it shows no difference in their peak distribution. However, some peaks have a higher intensity, which can be also seen in the amount of the two phases. The $Y_3Al_5O_{12}$ phase yielded 97.8% that is significant higher as in the samples before. The reason can be due to the higher Ce^{3+} ions concentration again.

With Equation 4 the particle size of the Ce^{3+} undoped and doped $Y_3Al_5O_{12}$ products were determined. The size of the particles ranges from 40 to 46 nm. However, the Scherrer equation only worked out with very broad peaks, which is not the case in these samples. It is only a rough estimation of the particle sizes from less crystalline substances. The sharp peaks in the spectra however indicate a very high crystallinity. Hence, the received particles sizes are not accurate.

4.4 Ce^{3+} doped YAG prepared by the Conventional Oxide Method

Two 0.7 wt% Ce^{3+} doped yttrium aluminum garnet samples were fabricated through the conventional oxide method. The 0.7 wth% Ce^{3+} ions come up to approximately 1 mol% of the dopant. The duplicate determination was carried out to compare the results of the solution combustion method with those of the conventional oxide method. The concentration of 0.7 wt% in the conventional method was chosen for a closer examination, in particular, to see whether the obtained results match with ones of the 1 mol% Ce^{3+} doped YAG prepared by solution combustion method, which reaches the highest luminosity.

4.4.1 Characterization with UV-Lamp

The illumination with UV-light with a wavelength of 254 nm revealed no luminescence of both Ce^{3+} doped YAG phosphors. The excitation with light at a wavelength of 365 nm shows a yellow glow as expected. However, the luminosity of the powders prepared by conventional oxide method was weaker than of the substrate fabricated by the solution combustion method. The following image demonstrates the luminescence intensities of the two YAG samples with 1 mol% Ce^{3+}-concentration of both methods.

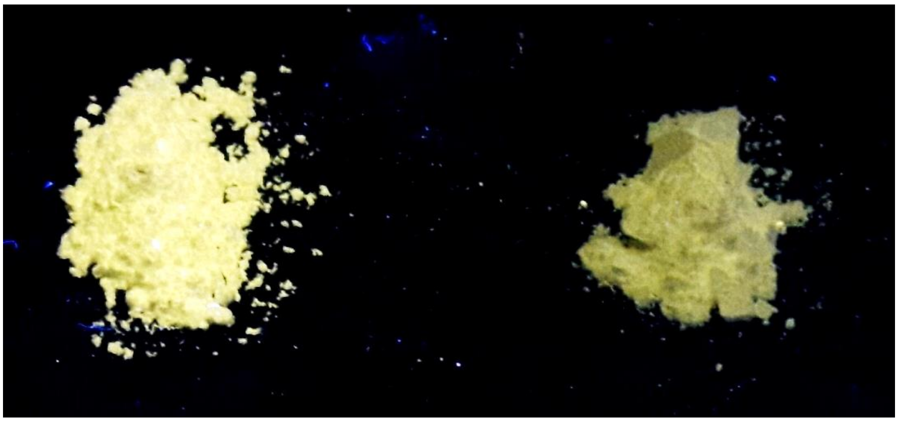

Figure 4.27: Luminosity of 1 mol% Ce^{3+} doped samples of both methods with an excitation wavelength of 365 nm. The powder on the left side is prepared by solution combustion method and the powder on the right side is prepared by conventional oxide method.

The preparation of the phosphor with the conventional oxide method resulted in a pale-yellow glowing of the powder. As can be seen in Figure 4.27 the luminosity of the phosphor is significantly lower, which can be observed with the naked eye. Hence, an insufficient insertion of the activator ions into the host material is assumed due to this visible unveiling. It is important to mention, that the color and the brightness of the image is slightly falsified by the used camera. Both powders have glowed with an excitation of a wavelength of 365 nm.

4.4.2 Characterization with Reflectance Spectroscopy

The reflectance spectra of the duplicate determination in the visible range and the near-infrared range after illumination with light of the 0.7 wt% Ce^{3+} doped YAG are shown in Figure 4.28.

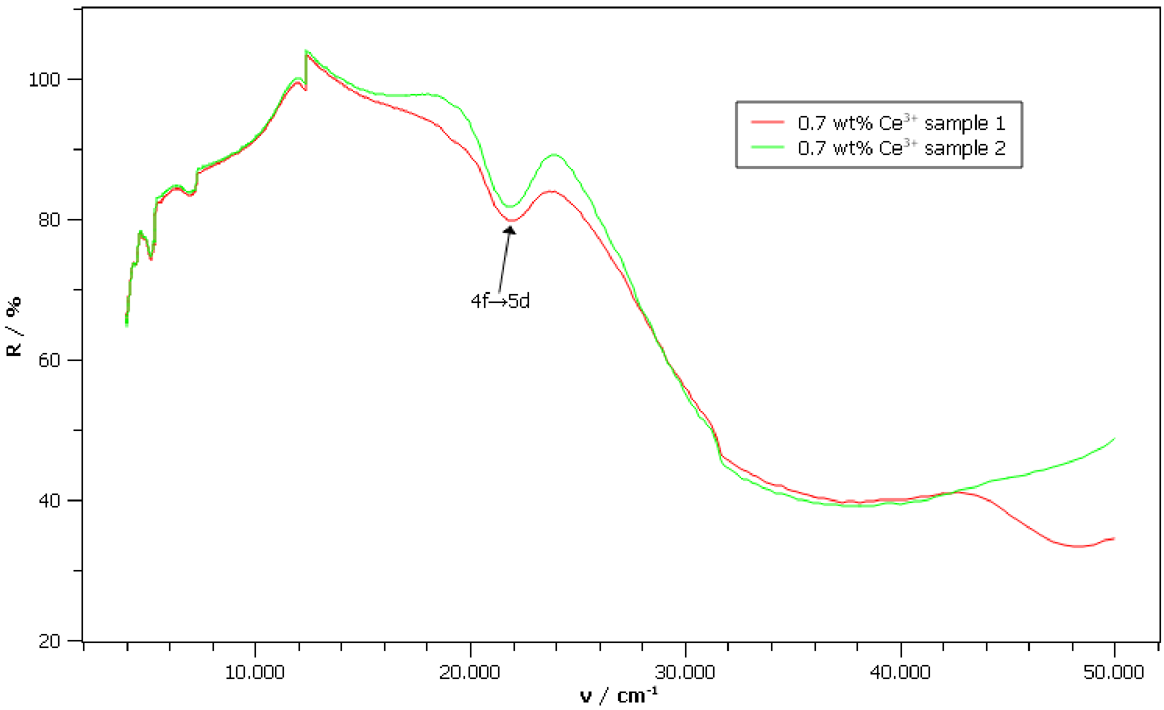

Figure 4.28: Reflectance spectra of the two YAG powders with an activator concentration of 0.7 wt% Ce^{3+} ions prepared by conventional oxide method. The detector change occurs at approximately 12 000 cm^{-1}.

Both products of the conventional oxide method have similar curves as the Ce^{3+} doped YAG in Figure 4.20. Each of the two curves in Figure 4.28 exhibit a peak in the range of approximately 20 000 to 23 000 cm^{-1}, which corresponds to the samples produced by solution combustion again. This peak characterizes the transition of an electron in the 4f- and 5d-levels, which is responsible for the yellow/green emission.

The peaks of both samples in the near-infrared range are assumed that they are produced due to overtones and vibrational combinations of the crystal lattice units again.

Furthermore, the detector leap at approximately 12 000 cm^{-1} is observed too, because of the switch of the InGaAs detector to the photomultiplier tube detector.

4.4.3 Characterization with Fluorescence Spectroscopy

The emission spectra of the duplicate determination of the 0.7 wt% Ce^{3+} doped $Y_3Al_5O_{12}$ fabricated by conventional oxide method are illustrated in Figure 4.29. Additionally, the rare earth doped YAG prepared by solution combustion with almost the same amount of Ce^{3+} ions is plotted too, to compare the methods again.

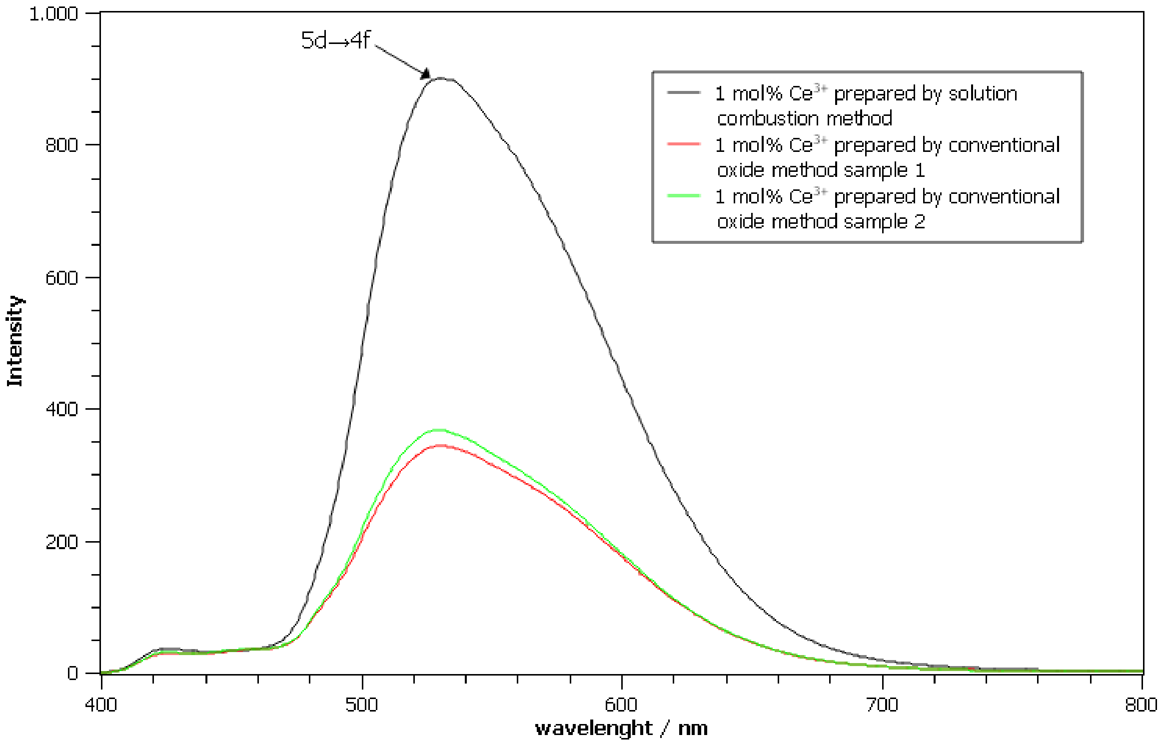

Figure 4.29: Emission spectra of 1 mol% Ce^3 doped YAG sample from solution combustion process and the two YAG samples from the conventional oxide method with approximately 1 mol% Ce^{3+} (0.7 wt%)

The green and the red curves in Figure 4.29 belong to the YAG phosphors, which were prepared using the conventional oxide method. These two samples have the same doping concentration of 0.7 wt%, that corresponds approximately to 1 mol%. For reasons of accuracy a double determination was carried out. The plot of them showed an almost identical curve progression, with the exception that the peak maximum differs slightly in its intensity. However, this intensity difference is very small and can be neglected. Thus, it can be said that the results of duplicate determination are reproducible. The emission spectra indicate a broad peak from around 490 to 640 nm, which corresponds to yellow and green light emission again. The peak is traced back to the 5d- and 4f- state transition of the Ce^{3+} ion as like in the samples from the solution combustion method. The yellow/ green emitted light is generated due to the lowering of the 5d-levels caused by the centroid shift and the crystal field splitting. Again, an integration of the cerium ions took place. In general, both preparation methods lead to a successful fabrication of the phosphor material and could be used in combination with a blue illumination light for white light emitting diodes.

However, the two curves of the conventional oxide method have lower peak maxima than the curve from the solution combustion method. The intensities are more than 50% lower, which suggests that the incorporation of the activator ions into the host matrix was not completely carried out. Accordingly, the synthesis of the Ce^{3+} doped YAG with the conventional process leads to insufficient results regarding to the luminosity. As can be seen in Figure 4.29 the luminosity of the phosphor, which was prepared by solution combustion is significantly higher. Hence, this doped YAG phosphor is more efficient due to the higher intensity of light emission. The lower luminosity of the Ce^{3+} doped YAG samples prepared by conventional oxide method is proved by the characterization with UV-light before as well.

The obtained light emitting phosphor with the 0.7 wt% Ce^{3+} could be used in LEDs, but its luminous intensity would be weak, whereas the product from the solution combustion supplies a stronger light emission. Therefore, the application of the phosphor from the combustion process would be economically more advantageous.

4.4.4 CIE color coordinates and color chart

Figure 4.30 represents the CIE color chart with the chromaticity values of all sintered Ce^{3+} doped YAG phosphors manufactured by solution combustion and the duplicate determination of the conventional oxide process.

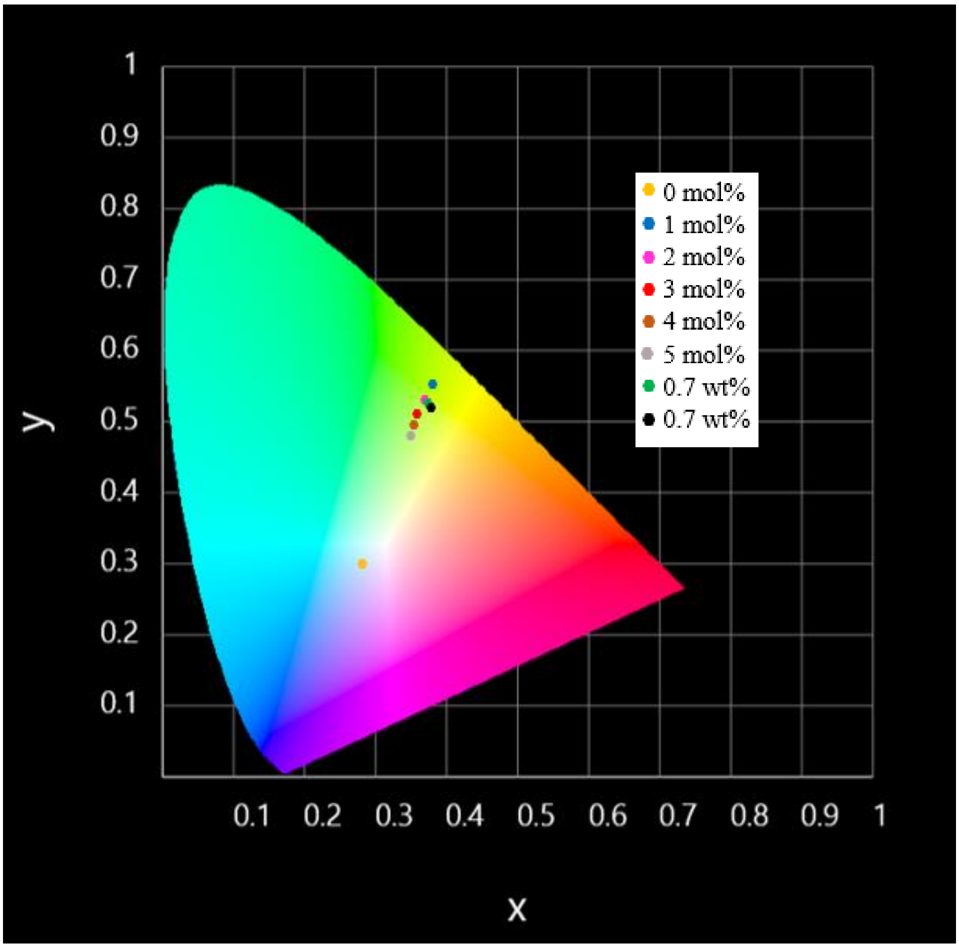

Figure 4.30: 1931 CIE color chart with marked chromaticity values of the sintered Ce^{3+} doped $Y_3Al_5O_{12}$ phosphors synthesized by solution combustion method and by conventional oxide method

The calculation of the tristimulus values and accordingly the chromaticity values of the two 0.7 wt% Ce^{3+} doped YAG phosphors from the conventional method (green and black dots) leads to results, which lies in the yellow/green area of the CIE color chart in Figure 4.30. However, it seems that they tend more to the yellow region of the diagram compared to the findings of the products from the solution combustion method. In any case, the color results of the duplicate determination coincide with the residual sample series prepared by solution combustion.

It is worth of mention that the YAG phosphors with 0.7 wt% Ce^{3+} ions, which corresponds to approximately 1 mol% Ce^{3+}, possess color coordinates with lower x and y values as the sample from the solution combustion method with nearly the same Ce^{3+}-concentration (blue point). Their values are shifted to a slightly lighter part of the yellow area of the color chart and match more with the 2 mol% Ce^{3+} doped phosphor of the solution combustion method. They all exhibit a weaker luminosity as the YAG sample with 1 mol% Ce^{3+} prepared by solution combustion.

4.4.5 Crystallographic Characterization

The characterization with XRD measurements of both 0.7 wt% Ce^{3+} doped $Y_3Al_5O_{12}$ delivers two spectra with several sharp peaks, which can be seen in Figure 4.31 and 4.32.

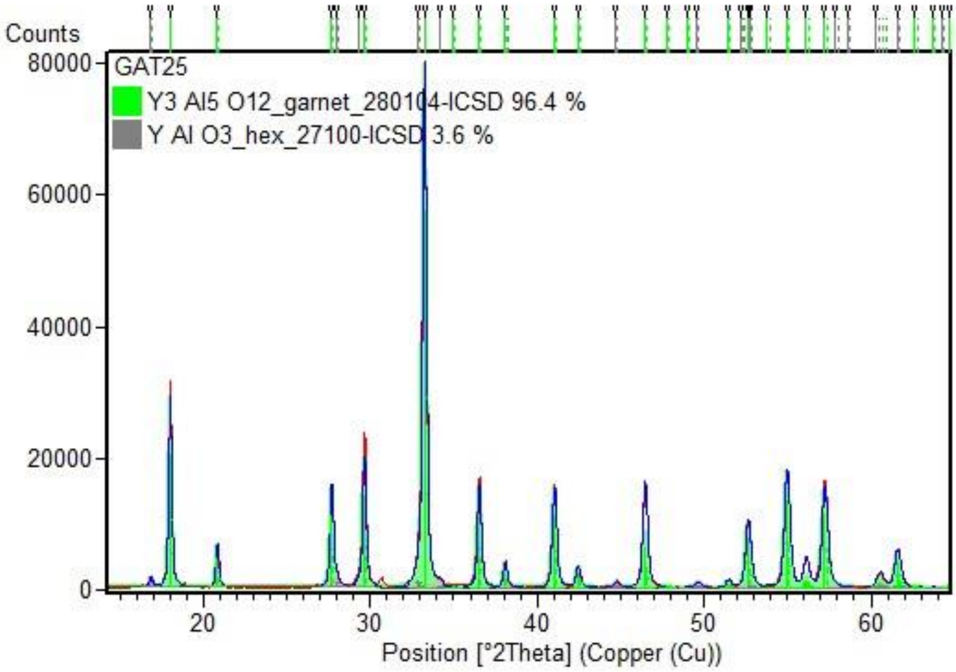

Figure 4.31: XRD spectrum with Rietveld refinement of $Y_3Al_5O_{12}$ with 0.7 wt% Ce^{3+} ions of sample 1

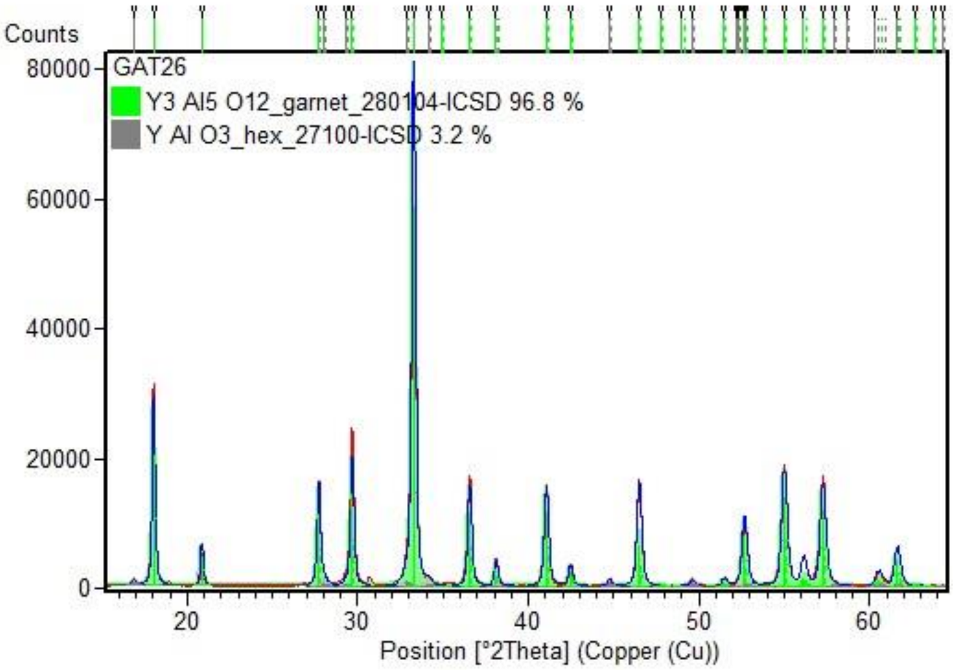

Figure 4.32: XRD spectrum with Rietveld refinement of $Y_3Al_5O_{12}$ with 0.7 wt% Ce^{3+} ions of sample 2

The spectra of the duplicate determination prepared by the conventional oxide method are quite identical. They exhibit the same number of peaks at the same positions with very similar counts of each peak.

The sharp and relatively well-separated peaks suggest that the gained products are very crystalline as like the sintered powders from the solution combustion method. The spectra of the samples from the conventional oxide route looks also like the spectra of the experimental series before. The peaks in the spectra show a quite similar pattern. However, the counts of the two samples from the conventional method are a bit higher as them of the products fabricated by solution combustion.

Figure 4.31 and Figure 4.32 reveal two different phases in the Ce^{3+} doped YAG phosphors. In analogy to the sample series of the solution combustion method. A large portion of the samples is the desired $Y_3Al_5O_{12}$ phase with 96.4 % and 96.8%. The activator Ce^{3+} ions do not exhibit an impact on the crystal lattice of the host matrix. The residual part of the samples consists of a hexagonal $YAlO_3$ phase. The Ce^{3+} doped YAG phosphors produced by conventional oxide method compose of a higher amount of the $Y_3Al_5O_{12}$ phase. However, the XRD measurements do not provide any information about the incorporation of the activator into the host material.

5 Summary and Outlook

In this work three series of phosphors for the application in white light emitting diodes were prepared by solution combustion method. The three series were Sm^{3+} doped $Ba_2YV_3O_{11}$, Dy^{3+} and Tm^{3+} doped $GdAl_3(BO_3)_4$ and Ce^{3+} doped $Y_3Al_5O_{12}$ phosphors with different concentrations of the dopant. Additionally, a duplicate determination of the Ce^{3+} doped $Y_3Al_5O_{12}$ were fabricated by conventional oxide route to compare the two different preparations method with each other. The three series of the combustion method and the duplicate determination of the conventional oxide method were characterized by investigations under the UV-lamp, fluorescence spectroscopy, reflectance spectroscopy and XRD measurements.

The sintered Sm^{3+} doped $Ba_2YV_3O_{11}$ samples show an orange luminescence due to the illumination with 254 nm and a pale-yellow luminescence with 365 nm. The emission spectra exhibit the characteristic broad yellow emission band of the vanadate group, which consists of two overlapping peaks. Furthermore, four emission bands of the Sm^{3+} ions, ranging from green to red region, are observed. Due to the broad emission distribution over the entire visible color spectrum, this phosphor material shows good color rendering properties. It has suitable conditions for the generation of white light similar to sunlight. The $Ba_2YV_3O_{11}$ sample with 2.5 mol% Sm^{3+} concentration exhibit the best properties for white light generation because of the emission spectrum and due to the calculated color coordinates. The XRD spectra of this series after the sintering step reveal a relative high phase purity. The particle sizes of the Sm^{3+} doped $Ba_2YV_3O_{11}$ samples ranges from 55 to 73 nm, which was successfully in the nanoscale.

The Dy^{3+} and Tm^{3+} doped $GdAl_3(BO_3)_4$ phosphors exhibit a yellowish luminescence. The color was paler than the color of the Sm^{3+} doped $Ba_2YV_3O_{11}$ samples. The emission spectra illustrate three characteristic peaks of Dy^{3+}, which are in the blue, yellow and red range. Two peaks are also observed from Tm^{3+}. The higher Tm^{3+} concentration shifts the chromaticity values of the phosphor to the blue range. Therefore, the $GdAl_3(BO_3)_4$ with 3 mol% Dy^{3+} and 1 mol% Tm^{3+} sample offers an emission color nearest to white light emission. The XRD spectra of the sintered Dy^{3+} and Tm^{3+} doped $GdAl_3(BO_3)_4$ samples show four different phases, from which two are the rhombohedral and the monoclinic $GdAl_3(BO_3)_4$ phases. However, the monoclinic phase is overrepresented in the spectra. The determination of the particle sizes results in a range from 132 to 184 nm, which is only a rough determination using the Scherrer equation.

The Ce^{3+} doped $Y_3Al_5O_{12}$ phosphors illustrate a significant yellow luminescence with an excitation at 365 nm. The yellow color of the luminescence is the most intensive compared to the other two phosphor materials. The emission spectra of the sample series of the Ce^{3+} doped YAG confirms the observations under the UV-lamp. It reveals a broad emission band, where the largest part is in the green/yellow region. The YAG sample with 1 mol% Ce^{3+} ions shows the highest intensity. With a further increase of the Ce^{3+} amount, the intensity decreases due to concentration quenching. Hence, 1 mol% Ce^{3+} is the optimal concentration as activator ions for YAG. The chromaticity values are in the yellow part of the 1931 CIE chart, which coincide with the emission spectra. However, the color coordinates of the 1 mol% Ce^{3+} sample lie in the intensive yellow area, whereas with increasing the Ce^{3+} ions amount the coordinates shift in direction of the white region. The XRD spectra of this series exhibit very crystalline products due to the sharp peaks. Additionally, the products have a high phase purity and the particle sizes are in the range from 40 to 46 nm. However, due to the high crystallinity the determination of the particle sizes with the Scherrer equation is not accurate.

The Ce^{3+} doped YAG prepared by solid state reaction method reveals the same yellow luminescence as the samples prepared by solution combustion method, but the intensity is weaker. This is also confirmed in the emission spectra. The duplicate determination shows the broad yellow emission band too, but with significantly weaker intensities. The chromaticity values are also in the yellow part of the 1931 CIE chart. The XRD spectra exhibit crystalline and pure products too. However, the solution combustion method is compared to the conventional oxide route timesaving and more efficient in luminescence. Furthermore, nanoparticles can be obtained.

Due to the color emission of all three phosphor materials the Sm^{3+} doped $Ba_2YV_3O_{11}$ has the best requirement for white light generation. The broad distribution of emission bands in the color spectrum leads to the possibility of white light generation due to a high color rendering index, provided that the relation of the activator ions concentration to the host material is adjusted. The Dy^{3+} and Tm^{3+} doped $GdAl_3(BO_3)_4$ are also able to produce white light with appropriate concentrations of the rare earth metal ions. However, due to the sharp peaks of the emission spectra, there are many missing wavelengths. Therefore, the white light of Dy^{3+} and Tm^{3+} doped $GdAl_3(BO_3)_4$ phosphor is less similar to daylight than the warmer white light of the Sm^{3+} doped $Ba_2YV_3O_{11}$ phosphor. The Ce^{3+} doped YAG in turn, produces an intensive yellow emission. Thus, a significant portion of blue must be introduced by the illumination source to generate white color emission. This blue component could be provided by using a blue LED for excitation.

The research in the field of WLEDs will further increase due to the promising results in light generation, energy saving and environmental aspects. It will focus on the improvement and optimization of already existing host/activator systems. However, the development of new host materials with various rare earth metal ions prepared by the solution combustion method will also be of great interest in the future because it provides nanoparticles with beneficial optical properties.

6 References

[1] M. Li et. al, Broadly tuning Sm^{3+} emission via crystal field micro-modulation in $CdMoO_4$ for white-LEDs, J Mater Sci: Mater Electron 28 (2017) 2642

[2] S. Al-Waisawy et. al, Preparation of balanced trichromatic white phosphors for solid-state white lighting, The Journal of Biological and Chemical Luminescence 32 (2017) 791

[3] Y. Lin et. al, Inorganic Phosphor Materials for Lighting, Top Curr Chem (Z) 374:21, Springer International Publishing Switzerland (2016) 2-3

[4] E. Vilejshikova et. al, Luminescence of Eu:$Y_3Al_5O_{12}$, Eu:$Lu_3Al_5O_{12}$, and Eu:$GdAlO_3$ Nanocrystals synthesized by Solution Combustion, Journal of Applied Spectroscopy 84, No. 5 (2017) 867

[5] E. Schubert, Light-Emitting Diodes, 2nd edition, Cambridge University Press, New York (2006) 353-354

[6] H. Shi et. al, Preparation and luminescence properties of YAG:Ce phosphor for white LED application via a vacuum sintering method, Phys. Status Solidi A 211, No.7 (2014) 1596

[7] B. Huang et. al, Luminescent properties of low-temperature-hydrothermally-synthesized and post-treated YAG:Ce (5%) phosphors, Optical Materials 36 (2014) 1561

[8] B. Jamalaiah, Optimization of photoluminescence of $GdAl_3(BO_3)_4$:Sm^{3+} phosphors for solid state lighting devices, Journal of Molecular Structure 1146 (2017) 546

[9] J. Wang et. al, Color-tunable luminescence and energy transfer properties of $Ba_3Y_{1-x}M_x(PO_4)_3$ (M= Dy, Tm) phosphor with UV light excitation, Journal of Luminescence 188 (2017) 497

[10] M. Dalal et. al, Energy transfer and photoluminescent analysis of a novel color-tunable $Ba_2Y_{1-x}V_3O_{11}$:xSm^{3+} nanophosphor for single-phased phosphor-converted white LEDs, Ceramics International 44 (2018) 10532

[11] T. Rossing, C. Chiaverina, Light Science: Physics and the Visual Arts, Springer Science & Business Media, New York (1999) 129

[12] P. Flesch, Light and Light Sources: High-Intensity Discharge Lamps, Springer Science & Business Media, Niederlande (2007) 17-18

[13] S. Stewart and R. Johnson, Blackbody Radiation: A History of Thermal Radiation Computational Aids and Numerical Methods, CRC Press, Boca Raton (2016) 3

[14] D. Basu, Dictionary of Material Science and High Energy Physics, CRC Press, Boca Raton (2001) 239

[15] Z. Jagoo, Tracking Solar Concentrators: A Low Budget Solution, Springer Science & Business Media, Dordrecht (2013) 7

[16] Blackbody Radiation, Retrieved January 6, 2019, from http://hyperphysics.phy-astr.gsu.edu/hbase/wien.html

[17] ZEISS Microscopy Online Campus: Tungsten-Halogen Lamps, Retrieved December 3, 2018, from http://zeiss-campus.magnet.fsu.edu/articles/lightsources/tungstenhalogen.html

[18] S. Kitsinelis, Light Sources: Technologies and Applications, CRC Press, Boca Raton (2016) 24

[19] Reference 12, p. 14

[20] T. Khanh et. al, LED Lighting: Technology and Perception, Wiley-VCH, Weinheim (2015) 19

[21] A. Tiwari et. al, Advanced Magnetic and Optical Materials, John Wiley & Sons, New Jersey (2016) 261-262

[22] J. Brox, Brilliant: The Evolution of Artificial Light, Houghton Mifflin Harcourt, Boston (2010) 7

[23] M. Shur and R. Zukauskas, Solid-State Lighting: Toward Superior Illumination, Proceedings of the IEEE, Vol. 93, No. 10 (2005) 1692

[24] R. Waits, Edison's vacuum technology patents, Journal of Vacuum Science & Technology A 21 (2003) 881

[25] V. Khanna, Fundamentals of Solid-State Lightning: LEDs, OLEDs, and Their Applications in Illumination and Displays, CRC Press, Boca Raton (2014) 7-13

[26] The Low Pressure Sodium Lamp, Retrieved December 11, 2018, from http://www.lamptech.co.uk/Documents/SO%20Spectral.htm

[27] J. Cho et. al, White light-emitting diodes: History, progress, and future, Laser Photonics Rev. 11, No. 2 (2017) 1

[28] C. Yang et. al, The Yellow Ring Measurement for the Phosphor-converted White LED, Physics Procedia 19 (2011) 182-183

[29] C. Tsai, Color Rendering Index Thermal Stability Improvement of Glass-Based Phosphor-Converted White Light-Emitting Diodes for Solid-State Lighting, International Journal of Photoenergy (2014) 1

[30] S. Ye et. al, Phosphors in phosphor-converted white light-emitting diodes: Recent advances in materials, techniques and properties, Materials Science and Engineering R 71 (2010) 3

[31] D. Dexter, A Theory of Sensitized Luminescence in Solids, The Journal of Chemical Physics Vol. 21, No. 5 (1953) 836-837

[32] Reference 30, pp. 9-10

[33] Reference 3, p. 11

[34] L. Zhang et. al, Enhanced light extraction of single-surface textured YAG:Ce transparent ceramics for high power white LEDs, Applied Surface Science 455 (2018), 425

[35] S. Agarwal et. al, Physical and optical properties of Ce: YAG nanophosphors and transparent ceramics and observation of novel luminescence phenomenon, Optical Materials Express Vol. 7, No. 3 (2017) 1057

[36] P. Atkins and J. de Paula, Atkins' Physical Chemistry, 8th edition, Oxford University Press, Oxford (2006) 732

[37] G. Jia et. al, Spectroscopy of $GdAl_3(BO_3)_4$: Tm^{3+} crystal, Journal of Applied Physics Vol. 96, No. 11 (2004) 6262

[38] Y. Yue et. al, Growth and Nonlinear Optical Properties of $GdAl_3(BO_3)_4$ in a Flux without Molybdate, Crystal Growth Design 16 (2016) 347

[39] E. Fuchs et. al, Polyspectral white light emission from Eu^{3+}, Tb^{3+}, Dy^{3+}, Tm^{3+} co-doped $GdAl_3(BO_3)_4$ phosphors obtained by combustion synthesis, Materials Science and Engineering B 156 (2009) 73

[40] W. Draai and G. Blasse, Energy Transfer from Vanadate to Rare-Earth Ions in Calcium Sulphate, phys. stat. sol. (a) 21 (1974) 569

[41] L. Li et. al, $NaBaLa_2(PO_4)_3$: A novel host lattice for Sm^{3+}-doped phosphor materials emitting reddish-orange light, Journal of Alloys and Compounds 701 (2017) 515

[42] C. Lisheng and S. Qiang, Synthesis and luminescence property of $Ba_2RV_3O_{11}$(R =Y,Gd,La):Eu^{3+} (or Dy^{3+},Bi^{3+}), Chinese Journal of Luminescence (1992) 226

[43] Reference 30, pp. 8-9

[44] B. Ratnam et. al, Optimization of synthesis technique and luminescent properties in Eu^{3+}-activated $NaCaPO_4$ phosphor for solid state lighting applications, Journal of Luminescence 185 (2017) 100

[45] H. Yang and J. Jeong, Synthesis, Crystal Growth, and Photoluminescence Properties of YAG:Eu^{3+} Phosphors by High-Energy Ball Milling and Solid-State Reaction, J. Phys. Chem. C 114 (2010) 226

[46] A. Varma et. al, Solution Combustion Synthesis of Nanoscale Materials, Chem. Rev. 116 (23) (2016) 14494

[47] A. Mukasyan, Solution Combustion as a Promising Method for the Synthesis of Nanomaterials, Advances in Science and Technology Vol. 63 (2010) 187-188

[48] Reference 3, pp 6-8

[49] Reference 3, pp 7

[50] Y. Shi et. al, Synthesis and characterization of $YNbTiO_6:Dy^{3+}$ phosphor, Journal of Alloys and Compounds 509 (2011) 3128

[51] H. Baig et. al, Investigation of luminescence properties of Dy^{3+} doped $YAlO_3$ phosphors synthesized through solid state method, Optik 127 (2016) 9179

[52] A. Durairajan et. al, Sol-gel synthesis and photoluminescence studies on colour tuneable Dy^{3+}/Tm^{3+} co-doped $NaGd(WO_4)_2$ phosphor for white light emission, Journal of Luminescence 157 (2015) 357

[53] B. Jamalaiah et. al, Luminescence, energy transfer and color perception studies of $Na_3Gd(PO_4)_2:Dy^{3+}:Tm^{3+}$ phosphors, Optical Materials 36 (2014) 1688

[54] M. Li et. al, Broadly tuning Sm^{3+} emission via crystal field micro-modulation in $CdMoO_4$ for white-LEDs, J Mater Sci: Mater Electron 28 (2017) 2642

[55] F. Yang et. al, Sm^{3+}-doped $Ba_3Bi(PO_4)_3$ orange reddish emitting phosphor, Spectrochimica Acta Part A: Molecular and Biomolecular Spectroscopy 105 (2013) 626

[56] A. Herrmann et. al, The effect of glass composition on the luminescence properties of Sm^{3+} doped alumino silicate glasses, Journal of Non-Crystalline Solids 502 (2018) 191

[57] J. Schanda, Colorimetry: Understanding the CIE System, John Wiley & Sons, New Jersey (2007) 29

[58] Reference 57, p. 10

[59] Reference 57, pp. 27-31

[60] Understand color science to maximize success with LEDs (MAGAZINE)-LEDs, Retrieved December 10, 2018, from https://www.ledsmagazine.com/articles/2012/05/understand-color-science-to-maximize-success-with-leds-magazine.html

[61] Reference 57, p. 30

[62] Reference 57, p. 31

[63] R. Kuehni and A. Schwarz, Color Ordered: A Survey of Color Systems from Antiquity to the Present, Oxford University Press, Oxford (2008)141

[64] Reference 57, pp. 33-34

[65] Reference 57, pp. 35-37

[66] R. Jagannathan et. al, Colour coordinates of some photoluminescent materials, B. Electrochem 4 (6) (1988) 597

[67] W. van Driel and X. Fan, Solid State Lighting Reliability: Components to Systems, Springer Science & Business Media, New York (2012) 565

[68] W. Burger and M. Burge, Digitale Bildverarbeitung: Ein algorithmische Einführung mit Java, 3. Auflage, Springer Vieweg, Berlin (2015) 365-367

[69] R. Hunt and M. Pointer, Measuring Colour, 4th edition, John Wiley & Sons, Chichester (2011) 45

[70] R. Hunt and M. Pointer, Measuring Colour, 4th edition, John Wiley & Sons, Chichester (2011) 44

[71] M. Dalal et. al, Energy transfer and photoluminescent analysis of a novel color-tunable $Ba_2Y_{1-x}V_3$:xSm^{3+} nanophosphor for single-phased phosphor-converted white LEDs, Ceramics International 44 (2018) 10535

[72] M. Dalal et. al, Energy transfer and photoluminescent analysis of a novel color-tunable $Ba_2Y_{1-x}V_3$:xSm^{3+} nanophosphor for single-phased phosphor-converted white LEDs, Ceramics International 44 (2018) 10537

7 Abbreviations

CIE	Commission internationale de l’éclairage
CMF	Color matching function
CRI	Color rendering index
GAB	$GdAl_3(BO_3)_4$
LEDs	Light emitting diodes
NIR	near-infrared
pc-LEDs	phosphor converted light emitting diodes
SCS	Solution combustion synthesis
UV	ultraviolet
WLEDs	White light emitting diodes
XRD	x-ray diffraction
YAG	$Y_3Al_5O_{12}$

8 List of Figures

9 List of Tables